

University of Windsor

Scholarship at UWindsor

Electronic Theses and Dissertations

Theses, Dissertations, and Major Papers

2004

Study of crossflow cooling and heating of air via an in-line elliptical tube array heat exchanger.

Mesbah-ul Ghani Khan
University of Windsor

Follow this and additional works at: <https://scholar.uwindsor.ca/etd>

Recommended Citation

Khan, Mesbah-ul Ghani, "Study of crossflow cooling and heating of air via an in-line elliptical tube array heat exchanger." (2004). *Electronic Theses and Dissertations*. 3649.
<https://scholar.uwindsor.ca/etd/3649>

This online database contains the full-text of PhD dissertations and Masters' theses of University of Windsor students from 1954 forward. These documents are made available for personal study and research purposes only, in accordance with the Canadian Copyright Act and the Creative Commons license—CC BY-NC-ND (Attribution, Non-Commercial, No Derivative Works). Under this license, works must always be attributed to the copyright holder (original author), cannot be used for any commercial purposes, and may not be altered. Any other use would require the permission of the copyright holder. Students may inquire about withdrawing their dissertation and/or thesis from this database. For additional inquiries, please contact the repository administrator via email (scholarship@uwindsor.ca) or by telephone at 519-253-3000ext. 3208.

Study of crossflow cooling and heating of air via an in-line elliptical tube
array heat exchanger

by

Mesbah-ul Ghani Khan

A Thesis

Submitted to the Faculty of Graduate Studies and Research
through the Department of Mechanical, Automotive, and Materials Engineering
in Partial Fulfillment of the Requirements for
the Degree of Master of Applied Science at the
University of Windsor

Windsor, Ontario, Canada

2004



Library and
Archives Canada

Bibliothèque et
Archives Canada

Published Heritage
Branch

Direction du
Patrimoine de l'édition

395 Wellington Street
Ottawa ON K1A 0N4
Canada

395, rue Wellington
Ottawa ON K1A 0N4
Canada

Your file *Votre référence*
ISBN: 0-494-00137-2
Our file *Notre référence*
ISBN: 0-494-00137-2

NOTICE:

The author has granted a non-exclusive license allowing Library and Archives Canada to reproduce, publish, archive, preserve, conserve, communicate to the public by telecommunication or on the Internet, loan, distribute and sell theses worldwide, for commercial or non-commercial purposes, in microform, paper, electronic and/or any other formats.

The author retains copyright ownership and moral rights in this thesis. Neither the thesis nor substantial extracts from it may be printed or otherwise reproduced without the author's permission.

AVIS:

L'auteur a accordé une licence non exclusive permettant à la Bibliothèque et Archives Canada de reproduire, publier, archiver, sauvegarder, conserver, transmettre au public par télécommunication ou par l'Internet, prêter, distribuer et vendre des thèses partout dans le monde, à des fins commerciales ou autres, sur support microforme, papier, électronique et/ou autres formats.

L'auteur conserve la propriété du droit d'auteur et des droits moraux qui protègent cette thèse. Ni la thèse ni des extraits substantiels de celle-ci ne doivent être imprimés ou autrement reproduits sans son autorisation.

In compliance with the Canadian Privacy Act some supporting forms may have been removed from this thesis.

Conformément à la loi canadienne sur la protection de la vie privée, quelques formulaires secondaires ont été enlevés de cette thèse.

While these forms may be included in the document page count, their removal does not represent any loss of content from the thesis.

Bien que ces formulaires aient inclus dans la pagination, il n'y aura aucun contenu manquant.


Canada

1020570

© 2004 Mesbah G. Khan

Study of crossflow cooling and heating of air via an in-line elliptical tube
array heat exchanger

by

Mesbah-ul Ghani Khan

APPROVED BY:

R. Seth

Department of Civil and Environmental Engineering

N. Zamani

Department of Mechanical, Automotive, and Materials Engineering

A. Fartaj, Co-Advisor

Department of Mechanical, Automotive, and Materials Engineering

D. S-K. Ting, Co-Advisor

Department of Mechanical, Automotive, and Materials Engineering

W. Altenhof, Chair of Defense

Department of Mechanical, Automotive, and Materials Engineering

September 8, 2004

ABSTRACT

The thermal resistance at airside for an air-to-water crossflow heat exchanger is significantly higher than waterside. Heat exchanger performance improvement task means to enhance the airside heat transfer coefficient. In current study, airside heat transfer and flow characteristics of an elliptical tube array heat exchanger were experimentally investigated by examining the effects of Reynolds number on Nusselt number and pressure drop coefficient.

In a thermal wind tunnel, the air-cooling and air-heating experiments were conducted via an array of 18 elliptical tubes (each 300 mm long) with their 31.7 mm major axis parallel to the air crossflow. The tubes, minor-to-major axis ratio of 0.3, were evenly spaced by 6.1 mm airgap. The array was placed in a 300 x 300 mm² and 600 mm long test section. Water entered the bottom tube, jig-jagged through the array, and exited at the top tube. Two temperature settings, constant air and water inlet temperatures and constant air and water inlet temperature difference, were applied. The airside Reynolds number (Re_a), based on the approach air-velocity and streamwise major-axis length of the tube, was varied between 10000 and 36000, while that for waterside (Re_w) based on mean water-velocity and inner-hydraulic diameter, altered from 1100 to 7300. The airside Nusselt numbers (Nu_a) was based on major-axis length, while that for waterside (Nu_w) on inner-hydraulic diameter of the tube.

The Re_a was found to be the key factor affecting the heat transfer. In all tests, the results showed that the average Nu_a increased with Re_a in power law relationship. The Nu_a was found to be almost independent of Re_w . The Nu_a in air-heating appeared slightly higher than air-cooling process. Considering the experimental limitations and uncertainty, a unified correlation was obtained as $Nu_a = 0.263 Re_a^{0.663} Pr_a^{1/3}$ for cooling and heating

tests. Current results compared well with literatures. The non-dimensional airflow pressure drop decreased with increasing Re_a and remained constant at higher Re_a .

The Nu_w also varied with Re_w . About 20% higher Nu_w in air-heating than air-cooling tests was observed. The overall Nu_w - Re_w correlations for air-cooling and air-heating were obtained. These results also compared well with the literatures.

Dedicated to my -

wife Sharmin,

son Samin,

and

daughter Maleeha

ACKNOWLEDGEMENTS

First of all, the author must thank the Almighty for sustaining and pulling him through this work and all his life.

The special thanks and sincere gratitude go to Dr. A. Fartaj and Dr. D. S-K. Ting for their consistent supervisions, supports, patient guidance, and astute suggestions throughout the research work. Without their expert guidance, appreciation, and continuous encouragement, the successful completion of this work would not have been possible with the same spirit and flavor as carried out and presented by the author in this thesis.

The author would like to extend his thanks to Mr. P. Seguin for his technical and electronic supports and to Mr. R. Tattersall for his technical and informative supports associated to thermal wind tunnel test rig.

The author deeply acknowledges the cordial supports and services provided by Mr. S. Budinsky and Mr. M. Enns (late) at the Technical Support Center in fabricating and installing the elliptical tube array heat exchanger test chamber for this research work.

The author gratefully thanks Ms. R. Gignac for providing very friendly secretarial assistance throughout his studentship with the Department of Mechanical, Automotive, and Materials Engineering. The secretarial supports in regards to the graduate assistantship provided by Ms. B. Denomey are also gratefully acknowledged.

The financial assistance provided by the University of Windsor in the form of Graduate Assistantship is highly acknowledged.

The author is very grateful to ASHRAE (American Society of Heating, Refrigerating, and Air-conditioning Engineers) for supporting with the Grant-in-Aid scholarship and honoring with its Life Member's Club (LMC) Award. Additionally thanks are extended to the Ministry of Training, Colleges, and Universities of Canada and to the University of Windsor for providing the Ontario Graduate Scholarship (OGS).

Finally, the author would like to express his sincere appreciation to his wife Sharmin, son Samin, and daughter Maleeha for their continued patience, understanding, and various supports throughout the duration of research and especially during the preparation of this thesis.

TABLE OF CONTENTS

ABSTRACT		iv
DEDICATION		vi
ACKNOWLEDGEMENTS		vii
LIST OF ORIGINAL PUBLICATIONS AND PRESENTATIONS		xiii
LIST OF TABLES		xiv
LIST OF FIGURES		xv
NOMENCLATURE		xvii
 CHAPTERS		
CHAPTER 1	INTRODUCTION	2
	1.1 Motivation	5
	1.2 Objectives	6
 CHAPTER 2	 LITERATURE SURVEY AND THE SCOPE OF THE CURRENT STUDY	 8
	2.1 Enhancing heat transfer using elliptical tubes	8
	2.1.1 Effect of tube axis ratio (AR) on heat transfer	9
	2.1.2 Role of cylinder orientation, spacing, angle of attack, and surface roughness on heat transfer	11
	2.1.3 Influence of number of tubes, array, and tube banks on heat transfer	12
	2.2 Minimizing pressure drop and vortex induced vibration using elliptical tubes	13
	2.3 Summary of literature review	14
	2.4 Scope of current study	15

CHAPTER 3	EXPERIMENTAL SETUP, PROCEDURES, AND MODELLING OF VELOCITY PROFILE	17
3.1	The thermal wind tunnel and the test section	18
3.2	Schematic of the test section with elliptical tube array heat exchanger	18
3.3	Experimental methods and operating conditions	20
3.4	Measurement and data collection procedures	22
3.4.1	Air, water and tube side temperature measurements	24
3.4.2	Airside velocity, mass flow rate, and pressure drop measurements	27
3.4.3	Waterside mass flow rate and velocity measurements	34
CHAPTER 4	THEORETICAL CONSIDERATIONS AND DATA REDUCTION	36
4.1	Evaluation of thermophysical properties of air and water	36
4.2	Assumptions made in the experiments and data reduction	37
4.3	Key dimensionless parameters	37
	Reynolds number (Re)	38
	Prandtl number (Pr)	39
	Grashof number (Gr)	41
	Pressure Coefficient at Airside (C_{press})	41
4.4	Representation of heat transfer – the Nusselt number (Nu)	42
4.5	Airside and waterside heat transfer rates (q) and coefficients (h)	46

CHAPTER 5	RESULTS AND DISCUSSIONS	52
5.1	Airside Analysis – both Air-cooling ($T_{a,i} > T_s > T_{w,i}$) and Air-heating ($T_{a,i} < T_s < T_{w,i}$) processes	53
5.1.1	Effect of Reynolds number on the heat transfer rate (q – Re_a relationship)	53
5.1.2	Effect of Reynolds number on Nusselt number (Nu_a – Re_a relationship)	59
5.1.3	Effect of Reynolds number on Nusselt number with Prandtl effect (Nu_a – Re_a – Pr_a relationship)	64
5.1.4	Comparison of current proposed Nu_a – Re_a – Pr_a correlation with other available studies	67
5.1.5	Pressure drop across the tube array (C_{press} – Re_a relationship)	70
5.2	Waterside Analysis – both Air-cooling ($T_{a,i} > T_s > T_{w,i}$) and Air-heating ($T_{a,i} < T_s < T_{w,i}$) processes	78
5.2.1	Effect of Reynolds number on the heat transfer rate (q – Re_w relationship)	78
5.2.2	Effect of Reynolds number on Nusselt number (Nu_w – Re_w relationship)	82
5.2.3	Comparison of current proposed Nu_w – Re_w – Pr_w correlations with other studies	86
CHAPTER 6	CONCLUSIONS AND RECOMMENDATIONS	91
6.1	Conclusions	92
6.2	Recommendations	95
REFERENCES		99

APPENDICES

APPENDIX-A UNCERTAINTY ANALYSES AND ERROR

ESTIMATIONS	107
A.1 Procedures of addressing uncertainty issues	107
A.2 Instrumental and measurements' uncertainties – independent parameters	111
A.2.1 Measurement uncertainties – basic independent geometric dimensions of the tubes and the array ($H = 2a_i, 2b_i, 2a_o, 2b_o, S_T, \text{ or } L$)	111
A.2.2 Measurement uncertainties – Airside pressure differences ($H = \Delta p_{\text{pitot}} \text{ or } \Delta p_{\text{array}}$)	115
A.2.3 Measurement uncertainties – temperatures ($H = T \text{ and } \Delta T$)	119
A.2.4 Measurement uncertainties – Water mass and collection time ($H = m_w \text{ and } t$)	122
A.3 Uncertainties in the evaluation of thermophysical properties of Air and Water	125
A.3.1 Uncertainties in the tube outer surface temperature Measurements ($H = T_{s,o}$)	126
A.3.2 Uncertainties in the determination of Airside film temperatures ($H = T_{f,a}$)	128
A.3.3 Uncertainties in the determination of Waterside bulk temperature ($H = T_{w,b}$)	130
A.3.4 Sample calculations of uncertainties in thermophysical properties ($H = c_p, \mu, \nu, \text{ Pr, } \rho$)	131
A.4 Propagation of uncertainties from independent to basic dependent parameters	135
A.4.1 Uncertainties in tube's basic dependent dimensions – ($H = L_t, A_{c,i}, A_{c,o}, P_i, P_o, D_{h,i}, D_{h,o}, A_{s,i}, \text{ or } A_{s,o}$)	135

A.4.2	Uncertainties in the Airside dependent parameters – ($H = V_a, \dot{m}_a, Re_a, \text{ or } q_a$)	145
A.4.3	Uncertainties in the Waterside dependent parameters – ($H = \dot{m}_w, V_w, Re_w, q_w$)	151
A.5	Propagation of uncertainties into the representative results	157
A.5.1	Uncertainties in the Airside Nusselt number – ($H = Nu_a$)	161
A.5.2	Uncertainties in the Airside pressure drop coefficient – ($H = C_{press}$)	163
A.5.3	Uncertainties in the Waterside Nusselt number (Nu_w)	166
A.6	Tabulation of overall uncertainty data for all the experiments	168
APPENDIX-B	TABULATION OF EXPERIMENTAL RESULTS	169
B.1	Table B.1: Heat transfer data corresponding to different Re_a (for a given Re_w)	170
B.2	Table B.2: Heat transfer data corresponding to different Re_w (for a given Re_a)	171
VITA AUCTORIS		173

LIST OF ORIGINAL PUBLICATIONS AND PRESENTATIONS

Some of the results and observations from each experimental phase of current study are disseminated and documented in the form of journal publication, conference presentations, and transaction publications as follows:

Khan, M. G., Fartaj, A. and Ting, D. S-K. 2004a. An experimental characterization of cross-flow cooling of air via an in-line elliptical tube array. Int. Journal of Heat and Fluid Flow, Vol. 25, No. 4, pp. 636-648.

Khan, M. G., Fartaj, A. and Ting, D. S-K. 2004b. An elliptical tube array as a cross flow heat exchanger in Heat Exchangers and Their Simulation, Thermal Management, and Fundamental Advances in Thermal and Fluid Sciences, Published by the Society of Automotive Engineers, Inc., PA, Vol. S-1818, pp. 151-160. (Originally presented at the SAE 2004 World Congress, March 2004, Detroit, USA, SAE Technical Paper # 2004-01-0217).

Khan, M. G., Fartaj, A. and Ting, D. S-K. 2005. Study of cross-flow cooling and heating of air via an elliptical tube array (Paper # TECH-00077-2004), American Society of Heating, Refrigerating, and Air-conditioning Engineers, Inc. (ASHRAE). Accepted for presentation in 2005 ASHRAE Winter Meeting, Feb. 2005, Orlando, FL, USA and also accepted for subsequent publication in the ASHRAE Transaction.

LIST OF TABLES

Tables	Descriptions	Page No.
3.3.1	Operating conditions: Air Cooling tests ($T_{a,i} > T_s > T_{w,i}$) and Air Heating tests ($T_{a,i} < T_s < T_{w,i}$)	22
5.1.1	Curve fit coefficients and R^2 values for Eq. (5.1.1) and Figures 5.1.1 to 5.1.4 ($q - Re_a$ variation)	54
5.1.2	Curve fit coefficients and R^2 values for Eq. (5.1.2) and Figures 5.1.5 to 5.1.8 ($Nu_a - Re_a$ variation)	60
5.1.3	Values of airside pressure coefficients (C_{press}) at different Re_a	77
5.2.1	Curve fit coefficients and R^2 values for Eq. (5.2.1) and Figures 5.2.1 and 5.2.2 ($q - Re_w$ variation)	79
5.2.2	Curve fit coefficients and R^2 values for Eq. (5.2.2) and Figures 5.2.3 and 5.2.4 ($Nu_w - Re_w$ variation)	82
A.1.1	Sample data for Air-heating test ($T_{w,i} > T_s > T_{a,i}$) – Measured and Calculated Values (Operating conditions: $\dot{m}_w \approx 0.06$ kg/s and $V_a \approx 9$ m/s)	110
A.2.1	Tubes' independent dimensions, H , as measured by the digital caliper	112
A.2.2	Uncertainties in tubes' basic independent dimensions (Measured)	115
A.2.3	Uncertainties in fundamental / independent experimental parameters	124
A.4.1	Uncertainties in tube's dependent dimensions (Calculated)	144
A.6.1	Overall uncertainty data for all the experiments	168
B.1	Heat transfer data corresponding to different Re_a (for a given Re_w)	170
B.2	Heat transfer data corresponding to different Re_w (for a given Re_a)	171

LIST OF FIGURES

Figures	Descriptions	Page No.
2.1	Schematic of airflow over an elliptical tube	8
3.1	(a) Closed-loop Thermal Wind Tunnel, (b) Test section with elliptical tube array (before installation), and (c) Test section (after installation)	17
3.2.1	Schematic of the test section with elliptical tube array – dimensions and measurement setup (drawn not to scale)	19
3.4.1	Sample $T_{s,o}$ variation in the direction of water flow (error bars are shown)	27
3.4.2	Pitot static tube with stem diameter $D = 2.38$ mm (drawn not to scale)	28
3.4.3a	Air velocity at the test section inlet (5 x 5 grid point measurement: $V_a = 5$ m/s; maximum deviation from the mean = $\pm 4.5\%$) – Contour	30
3.4.3b	Air velocity at the test section inlet (5x5 grid point measurement: $V_a = 5$ m/s; maximum deviation from the mean = $\pm 4.5\%$) – 3D plot	30
3.4.4a	Air velocity at the test section inlet (5 x 5 grid point measurement at $V_a = 10.8$ m/s; maximum deviation from the mean = $\pm 1.5\%$) – Contour	31
3.4.4b	Air velocity at the test section inlet (5 x 5 grid point measurement at $V_a = 10.8$ m/s; maximum deviation from the mean = $\pm 1.5\%$) – 3D Plot	31
3.4.5a	Air velocity at the test section inlet (5 x 5 grid point measurement at $V_a = 16.5$ m/s; maximum deviation from the mean = $\pm 2.6\%$) – Contour	32
3.4.5b	Air velocity at the test section inlet (5 x 5 grid point measurement at $V_a = 16.5$ m/s; maximum deviation from the mean = $\pm 2.6\%$) – 3D Plot	32
3.4.6	Experimental domain with pressure measurement taps (drawn not to scale)	33

5.1.1	Change of q with Re_a for different Re_w (Phase-I: Air-cooling test)	55
5.1.2	Change of q with Re_a for different Re_w (Phase-II: Air-heating test)	56
5.1.3	Change of q with Re_a for different Re_w (Phase-III: Air-cooling test)	56
5.1.4	Change of q with Re_a for different Re_w (Phase-IV: Air-heating test)	57
5.1.5	Change of Nu_a with Re_a for different Re_w (Phase-I: Air-cooling test)	61
5.1.6	Change of Nu_a with Re_a for different Re_w (Phase-II: Air-heating test)	61
5.1.7	Change of Nu_a with Re_a for different Re_w (Phase-III: Air-cooling test)	62
5.1.8	Change of Nu_a with Re_a for different Re_w (Phase-IV: Air-heating test)	62
5.1.9	Nu_a - Re_a - Pr_a relationships for cooling and heating (Error bars shown)	65
5.1.10	Comparison of current Nu_a - Re_a - Pr_a relationship with other correlations	68
5.1.11	Case-I: Variation of $C_{press, array}$ with Re_a for the whole array of elliptical tubes	71
5.1.12	Case-II: Variation of C_{press} with Re_a for a single elliptical tube in array	72
5.1.13	Case-III: Comparison of current C_{press} - Re_a relation with available studies	75
5.2.1	Change of q with Re_w for different Re_a (Phase-I: Air-cooling test)	79
5.2.2	Change of q with Re_w for different Re_a (Phase-II: Air-heating test)	80
5.2.3	Change of Nu_w with Re_w for given Re_a (Phase-I: Air-cooling test)	83
5.2.4	Change of Nu_w with Re_w for given Re_a (Phase-II: Air-heating test)	83
5.2.5	Nu_w - Re_w - Pr_w relationships for cooling and heating processes	85
5.2.6	Comparison of current Nu_w - Re_w - Pr_w relationship with other correlations	88

NOMENCLATURE

A	Area [m ²]
a	Semi-major axis length of the tube [m]; $2a$ = Major axis length of the tube
A_c	Cross-sectional area of the tube [m ²]; $A_c = \pi ab$
AR	Axis ratio (ratio of minor to major axis lengths), $AR = \frac{b}{a} = \sqrt{1-e^2}$
A_s	Tube surface area [m ²]; $A_s = PL_t$
B	Bias error
b	Semi-minor axis length of the tube [m]; $2b$ = Minor axis length of the tube
BR	Blockage ratio
$C_1 - C_8$	Correlation/curve fit coefficients
C_D	Drag coefficient
c_p	Specific heat capacity at constant pressure [kJ/kg.°C]
C_{press}	Airside pressure coefficient; $C_{\text{press_array}} = \frac{\Delta p_{\text{array}}}{\frac{1}{2} \rho_a V_{a, \text{max}}^2}$ (for the whole array), and $C_{\text{press}} = \frac{\Delta p_{\text{array}}}{\frac{1}{2} \rho_a V_a^2 N_T}$ (for a single tube in the array)
D_h	Hydraulic diameter [m]; $D_h = \frac{4A_c}{P}$
e	Eccentricity of elliptic tube; $e = \frac{\sqrt{a^2 - b^2}}{a}$
f	Friction factor
g	Gravitational acceleration [9.806 m/s ²]
Gr_a	Grashof number at airside; $Gr_a = \frac{g \beta_a (T_{a,i} - T_{s,o}) Z_a^3}{\nu_a^2}$

Gr_w	Grashof number at waterside; $Gr_w = \frac{g\beta_w(T_{w,b} - T_{s,i})Z_w^3}{\nu_w^2}$
h	Heat transfer coefficient [W/m ² .°C]
H	A generic variable to denote any of the tube/array geometric dimensions (e.g. $2a_i$, $2b_i$, $2a_o$, $2b_o$, L , S_T , A_c , A_s , etc.) or parameters such as T_a , ΔT_a , T_w , ΔT_w , ΔT_s , Δp_{pitot} , Δp_{array} , \dot{m}_a , \dot{m}_w etc.
k	Thermal conductivity [W/m.°C]
L	Spanwise length of each elliptical tube in the array [m]
L_t	Total length of 18 tubes excluding the 180° Plexiglas bends [m]
m	Mass of the fluid [kg]
\dot{m}	Mass flow rate of the fluid [kg/s]
N	Degree of freedom/number of measurement steps for the whole population
n	Total number of repeated readings for the same measurements
N_T	Number of flow obstruction mediums / tubes
Nu	Nusselt number; for air: $Nu_a = h_a(2a_o)/k_a$ and for water: $Nu_w = h_w D_{h,i}/k_w$
P	Perimeter/Circumference of the elliptic tube [m]; or the Precision error component when appears in uncertainty analysis
Pr	Prandtl number; $Pr_a = (\mu_a c_{p,a})/k_a$ for air and $Pr_w = (\mu_w c_{p,w})/k_w$ for water
q	Heat transfer rate [Watt]
R^2	Coefficient of determination (i.e. an indicator of reliable curve-fit); $0 \leq R^2 \leq 1$, The closer the R^2 value to 1 ($R^2 \rightarrow 1$), the better the curve-fit.
Re	Reynolds number; for air: $Re_a = V_a(2a_o)/\nu_a$ and for water: $Re_w = V_w D_{h,i}/\nu_w$
R_{th}	Thermal resistance [°C/W]

S_c	Center-to-center distance between two adjacent tubes in the array [m]
S_H	Sample standard deviation for the parameter H
S_T	Distance of narrowest gap between two adjacent tubes in the array [m]
T	Temperature [$^{\circ}\text{C}$]
t	Time recorded by stopwatch [sec] for water mass flow calculation; or the Student-t distribution in uncertainty analysis section
$T_{f,a}$	Airside film temperature [$^{\circ}\text{C}$]; $T_{f,a} = (T_{a,i} + T_{s,o}) / 2$
$T_{w,b}$	Bulk water flowing temperature inside tube array [$^{\circ}\text{C}$]; $T_{w,b} = (T_{w,i} + T_{w,o}) / 2$
U	Variable to denote the uncertainty
V	Mean velocity of flowing fluid [m/s]
X	X-coordinate in Figure 3.2.1 and a product in Eq. (5.2.5a)
Y	Y-coordinate in Figure 3.2.1 and a product in Eq. (5.2.6a)
y	A coefficient to the generalized heat transfer relation (Eqs. 4.4.3 to 4.4.5)
Z	Z-coordinate in Figure 3.2.1, and characteristic length [m]; $Z_a = 2a_o$ for airside and $Z_w = D_{h,i}$ for waterside

Greek letters

Δp	Pressure difference [Pa]
ΔT	Mean temperature difference between any two locations [$^{\circ}\text{C}$];
ΔT_a	Mean temperature difference between the air inlet and outlet [$^{\circ}\text{C}$]; $\Delta T_a = T_{a,i} - T_{a,o} $
ΔT_{a-s}	Mean temperature difference between inlet air and tube outer surface [$^{\circ}\text{C}$]; $\Delta T_{a-s} = T_{a,i} - T_{s,o} $

ΔT_{a-w}	Mean temperature difference between the air inlet and water inlet [°C]; $\Delta T_{a-w} = T_{a,i} - T_{w,i} $
ΔT_w	Mean temperature difference between the water inlet and outlet [°C]; $\Delta T_w = T_{w,i} - T_{w,o} $
ΔT_{w-s}	Mean temperature difference between bulk water and tube inner surface [°C]; $\Delta T_w = T_{w,b} - T_{s,i} $
α	Thermal diffusivity [m ² /s]
β	Coefficient of thermal expansion [K ⁻¹]
δ	Boundary layer thickness [m]
ε	Emissivity of copper tube
μ	Dynamic viscosity [kg/m.s]
μ_s	Dynamic viscosity taken at surface temperature of the tube array [kg/m.s]
ν	Kinematic viscosity or Momentum diffusivity [m ² /s]
ρ	Density [kg/m ³]
σ	Stefan-Boltzmann constant, $\sigma = 5.66961 \times 10^{-8}$ [W/m ² .K ⁴]
ψ	Void fraction used to calculate $V_{a,max}$; $\psi = S_c / S_T = (1 + 2b_o / S_T)$

Superscripts / Exponent

m	An exponent to the generalized heat transfer relation (Eqs. 4.4.3 to 4.4.5)
n	An exponent to the generalized heat transfer relation (Eqs. 4.4.3 and 4.4.4)
p	An exponent to the generalized heat transfer relation (Eqs. 4.4.3 to 4.4.4)

Subscripts

a	Air
array	Measured across the elliptical tube array
b	Bulk
c	Cross-section
C_{press}	Airside pressure coefficient
d	Dew point
duct	Test section duct
f	Film
h	Hydraulic
h_a	Airside heat transfer coefficient
h_w	Waterside heat transfer coefficient
i	Inlet or entrance for airside and waterside; or inner side for the tube surface; or when appears in uncertainty analysis, it represents a variable to count the number of repeated readings for the same measurement
j	Variable to denote the total number of measurements for the whole population
max	Maximum
Nu_a	Nusselt number at airside
Nu_w	Nusselt number at waterside
o	Outlet or Exit for airside and waterside; and outer side for tube surface
pitot	Measured by Pitot static tube
q	Overall Heat transfer rate

q_a	Heat transfer rate at airside
q_w	Heat transfer rate at waterside
Re_a	Reynolds number at airside
Re_w	Reynolds number at waterside
s	Tube surface
t	Total
w	Water
x	Number of error sources

Equation Symbols for Uncertainty Analysis

$B_{\bar{H}}$	Bias error limit of the mean of parameter H
\bar{H}	Mean value of the parameter H
$P_{\bar{H}}$	Precision error limit of the mean of parameter H
$S_{\bar{H}}$	Standard deviation of the mean for the parameter H
$U_{\bar{H}}$	Overall absolute uncertainty in the measurement of parameter H
$\frac{U_{\bar{H}}}{\bar{H}}$	Overall relative uncertainty in the measurement of parameter H

CHAPTER 1

INTRODUCTION

1. INTRODUCTION

Energy, in a number of different forms, plays crucial and vital roles for the development of any nation regardless of any location in the globe. The processing of raw materials and their subsequent modification and fabrication into products to improve our quality of living require a significant amount of energy. Thus the production, utilization, and exchange of energy are part of our daily life. In the study of the areas of thermodynamics, a necessity was felt to distinguish the energy that is stored in a system from that which is in transition from one system to another. This energy in transition may be either heat or work. The transmission, utilization, and management of this heat energy are unavoidably common for the survival of the human beings in this earth.

In utilizing the heat energy, there are some situations in which the direct mixing of one substance (from where the energy is to be removed) with another (in which the energy is to be added) is not possible or not convenient. Even when it is possible, the desired purpose may not be met properly. For instance, we can burn a certain amount of fuel directly in a cold room to release the heat energy required to mix with air to warm the room to a comfortable living level. On the other hand, the presence of the combustion products in the room soon brings the room to an uncomfortable and unlivable state. Situation like this has initiated the necessity of separating the medium where the heat energy is stored from that of the medium where the heat energy is to be added. This separation is generally made by means of a finite barrier, usually the wall, which poses another constraint to the effective heat transfer called the thermal resistance. Extensive efforts have thus been devoted in the past to devise equipment, which is capable of efficiently transferring heat energy from one medium to another in the presence of such separating wall. This has dictated the development of a special kind of device, which

bears a generic name called the “heat exchanger”. The most frequently used heat exchanger is the type where the hot and cold fluids are separated by a partition through which heat, but not matter, flows. As the applications of heat exchangers are found everywhere, the complete treatment of a heat exchanger design, especially the thermal analysis, is essential, which is the subject area of current study.

For scientific and industrial progress, it is essential to gain a better understanding on how to specify the heat transfer in an exchanger, which will occur under some given conditions. As a wall separates two fluids, most part of the total thermal resistance is shared by the fluid layers adjacent to the wall and very little by the wall itself. This resistance dictates the heat transmission between the fluids via respective fluid side heat transfer coefficient and the surface area. The performance improvement of a heat exchanger depends on the enhancement of heat transfer coefficients from fluid-to-wall surface. The exchange of heat from a wall to a fluid or from a fluid to a wall is thus a very important process, which is involved in almost all types of heat exchangers.

Heat exchangers can be classified in many ways based on the duty demanded, construction features, flow arrangements, transfer process, number of fluids involved, size etc., details of which can be found in any heat exchanger handbook available today. Of all, cross flow heat exchanger is a type encountered in numerous applications, such as an automotive radiator and air-conditioning system, in which the flow of fluids is perpendicular to each other. Heat transfer in this type of system is driven mainly by the forced convection mechanism where both fluids are forced to flow by external means such as a pump, a blower etc. In the subject of heat transfer and fluid flow, the fluid flow velocity is generally characterized by a dimensionless term called the Reynolds number. Tubes of various kinds are used in heat exchangers to provide the separating walls as well

as to provide the required heat transfer surface area. Almost all of the earlier heat exchangers used the circular tubes as their components.

Due to the interaction between heat transfer and fluid flow, the thermal resistance in forced convection mechanism is determined by the thickness of the boundary layer, which develops on the tube surface. Earlier, in the efforts of improving heat exchanger performance by many researchers, it was identified that the thicker the boundary layer the lower the heat transfer is. To take care of this problem, it was also recognized that an effective means of increasing heat transfer is to increase the fluid flow velocity thereby increasing the Reynolds number. For a fixed size, this requires an increase in velocity, which, again results in an increase in pressure drop across the heat exchanger. This means that more pump work is required, thereby increasing the initial equipment as well as the operating costs. All of these created an urge of finding further techniques to reduce thermal resistance and to enhance the convective heat transfer in a heat exchanger in a way that is most efficient and cost effective. Recently, economic and environmental issues coupled with the space saving considerations have led to the search for more efficient lightweight compact heat exchangers. In this event, the heat transfer enhancement has been the main focus among researchers in this area. The heat transfer enhancement research includes, but is not limited to, the increase of heat transfer area, promoting flow disturbance, changing tube shapes, identifying efficient tube orientation, optimizing flow configuration etc.

In an effort to maximize the heat transfer and minimize the pressure drop, tubes or banks of tubes in crossflow have been the focus of a large number of investigations. Different body shapes and orientations of various types of tubes have been extensively studied and utilized in many applications. While numerous studies have been made on a

single circular tubes or an array of circular tubes, little effort focused on an elliptical tube or array. Although the finned elliptical tube heat exchanger developed by a German company Happel GmbH & Company was in use for cooling transformer oil by air as early as 1926, the first air-cooled condenser in the world of stationery steam turbine works, however, was built and supplied by the same company in 1939 (Schulenberg 1966). In spite of this early use, mass research and application interests on elliptical tube heat exchangers were rare until recent years when it could be anticipated that the elliptical tube has superior combined thermal-hydraulic features over circular cylinder in terms of enhanced heat transfer rate, and minimized pressure drop and vortex or flow induced vibration. Besides, elliptic tubes can increase the system compactness because of their larger heat transfer area per unit volume compared to circular tubes. This has led to choose an elliptical tube array heat exchanger as the subject of current study.

Traditionally air-to-water crossflow heat exchanger consists of tubes of various shapes. The airside generally accounts for about 90% or more of the total thermal resistance of virtually any typical air-to-water heat exchangers (Wang 2000), which demands essentially a proper choice of airside heat transfer correlation in the relevant heat exchanger design and application. Thus, the determination of airside Nusselt number and Reynolds number relationship was taken as the principal focus of the current study.

1.1 Motivation

Today's industries are in search of lightweight efficient compact heat exchanger for saving money, energy and space. An elliptical tube array heat exchanger was chosen in the current study, because, it is anticipated to be a good candidate over circular tube for such competitive heat exchangers for the following reasons:

- o It provides higher heat transfer rate -- increasing heat exchanger efficiency
- o It offers heat exchanger compactness (heat transfer area per unit volume is higher) – saving application space
- o It minimizes pressure drop – minimizing the pumping power and thus the initial cost
- o It is less susceptible to vortex-induced vibration (VIV) – reducing structural failure

1.2 Objectives

For an air-to-water cross flow heat exchanger, the airside generally accounts for about 90% or more of the total thermal resistance, which indicates that the performance improvement of such heat exchanger is mainly dominated by the airside heat transfer coefficient. The main objective of current study is thus to investigate the airside heat transfer characteristics of an in-line array of elliptical tube heat exchanger. This has been carried out through,

- o obtaining the airside Nusselt number versus Reynolds number relationship (Nu_a - Re_a) and compare with available correlation in the literature, and
- o observing the variation of airside pressure drop with Reynolds number (C_{press} - Re_a) and compare with available correlation in the literature.

Additionally,

- o the waterside Nusselt number versus Reynolds number relationship (Nu_w - Re_w) has also been estimated and compared with available correlation in the literature.

CHAPTER 2

LITERATURE SURVEY AND THE SCOPE OF THE CURRENT STUDY

2. LITERATURE SURVEY AND THE SCOPE OF THE CURRENT STUDY

Being the heat exchanger system components, cylinders of different body shapes and orientations have been extensively studied and utilized in many applications. A single cylinder at cross flow of air has been the subject of intensive research for many years. To maximize the heat transfer and minimize the pressure drop, array of tubes or banks of tubes in cross flow have also been the focus of a large number of investigations. Although a handsome number of studies have been made on a single circular cylinder or an array of circular tubes, studies on an elliptical tube or an array are scarce. From a few number of studies, it is seen that the elliptical tube has superior combined thermal-hydraulic features over circular cylinder in terms of enhanced heat transfer rate and minimized pressure drop as reviewed below. Also elliptical tubes can increase the system compactness because of their larger heat transfer area per unit volume compared to circular cylinders. The dimension of an elliptical tube is generally represented by its axis ratio (AR), which is the ratio of minor-to-major axis length (see Figure 2.1). Brief reviews of some literatures available on the study of elliptical tubes are given below.

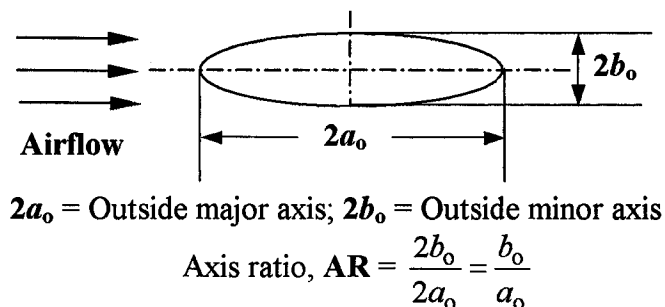


Figure 2.1 Schematic of airflow over an elliptical tube

2.1 Enhancing Heat Transfer Using Elliptical Tubes

Several investigators reported that, in general, an elliptic tube enhances heat transfer relative to a circular one. For example, Matos et al. (2001) numerically

investigated the heat transfer of staggered circular and elliptic tube banks in cross flow of air. The elliptic tubes had an AR of 0.75 with the tube length to minor axis ratio of 6.2. The surface temperature of the tubes was assumed constant and a constant Prandtl number of 0.72 was used. The Reynolds number based on the length of the tube row however was varied from 300 to 800 (i.e. from 75 to 200 when based on the streamwise major axis length of the tube). Compared to circular tube, their results for the same flow obstruction area (i.e. the blockage) showed a 13% relative heat transfer gain due to elliptic configuration. Rahman et al. (2001) numerically investigated the fluid flow and heat transfer characteristics around single isolated cylinders of circular and elliptic cross section at Reynolds number of 36000. The information on the characteristic dimension used in the calculation of Reynolds number was not reported. They used a circular cylinder (i.e. AR = 1) and an elliptical cylinder with an AR of 0.5 whose perimeter was similar to that of the circular one. Both the cylinders, with a constant prescribed surface temperature, were placed in cross flow of air at zero angle of attack. They concluded that the elliptic cylinder provides higher heat transfer coefficient than that of the circular one. Also, Sohal and O'Brien (2001) found that for the same cross sectional area a single elliptical tube with an AR of 0.33 could enhance the heat transfer coefficient by 25-35% compared to a single circular cylinder depending on various design parameters.

2.1.1 Effect of Tube Axis Ratio (AR) on Heat Transfer

Many researchers have studied the effects of tube AR on crossflow heat transfer. One of such studies, a very early but comprehensive one, was made by Eckert and Livingood (1953) on elliptical cylinders for ARs of 0.25 and 0.50, where the major axis was used to define the Reynolds and Nusselt numbers. The investigated range of

Reynolds number was not clearly reported though. The cylinder wall temperature in the analysis was assumed to be constant. The results, based on exact solutions of the laminar boundary layer equations, were compared with other analytical methods and available experimental results. Their findings show that the heat transfer coefficient is higher for elliptical cylinders than circular ones and that the elliptical cylinder with the smaller AR has relatively higher heat transfer coefficient. Rocha et al. (1997) numerically analyzed the heat transfer characters of one- and two-row tubes (circular and elliptic cylinders) and plate fin heat exchangers with air at cross flow. A constant surface temperature was prescribed as boundary condition for the tube surface. The Reynolds numbers, based on hydraulic diameter, was investigated up to 1600 for a constant airside Prandtl number of 0.70. They observed that the elliptical configuration with an AR of 0.86 and a ratio of semi-minor axis to the length of the tube row of 0.23 is the most efficient one among the ARs of 0.75, 0.86 and 1 studied. Badr (1998) numerically studied the forced convection heat transfer from a straight isothermal elliptic tube placed at cross flow of air. Four different elliptic axis ratios of 0.9, 0.7, 0.5, and 0.4 were investigated and in the Reynolds number range, based on twice the focal distance, from 20 to 500 (i.e. approximately from 22 to 1150 when based on major axis length of the tube). The airside Prandtl number was assumed constant at 0.70. He studied the effect of axis ratio for Reynolds number from 110 to 230 (based on major axis length of the tube) and found that the maximum heat transfer rate occurred for the smallest axis ratio, i.e. for $AR = 0.4$. Harris and Goldschmidt (2002) studied the overall heat transfer for elliptical cylinders in cross flow for different ARs. The Reynolds number, based on the major axis length, was investigated from 7400 to 74000. Their result showed that the elliptical tube should have an AR of 0.30 or less to achieve any appreciable change (greater than 10%) in heat

transfer coefficient compared to a circular cylinder. All the studies mentioned here, except Rocha et al. (1997), agreed that the tubes of smaller ARs (i.e. < 1) are more effective in transferring heat. On the other hand, there may be also a critical lower limit of AR beyond which appreciable change in heat transfer may not be achieved. Ebadian et al. (1986) analytically solved the energy equation for a single elliptic tube and investigated the Nusselt number as a function of AR for both uniform wall heat flux and uniform wall temperature conditions. They examined the range of AR from 0 to 1 and found no substantial increase in Nusselt number for AR less than 0.10. The average Nusselt number for uniform wall heat flux condition found to be higher than the uniform wall temperature conditions approximately by 17% and this higher heat transfer proportion was the same for the range of ARs examined. From all the above investigations it is concluded that for an elliptic tube, the heat transfer rate increases with decreasing AR in the range $1 < AR < 0.1$ and remains independent of AR for $AR < 0.1$.

2.1.2 Role of Cylinder Orientation, Spacing, Angle of attack, and Surface roughness on Heat Transfer

There are some other parameters, such as the cylinder orientation, angle of attack, surface roughness, and spacing (in the case of an array of cylinders or banks of tubes) that influence the heat transfer. There are some studies that focus on the effect of these parameters on heat transfer. Nishiyama et al. (1988) experimentally investigated the heat transfer and flow characteristics around elliptic cylinders with an AR of 0.5. The Reynolds number, based on the major axis length of the cylinder, was varied from 15000 to 70000 and the angle of attack from 0° to 90° . The nondimensional cylinder spacing, ratio of surface-to-surface narrowest gap between two adjacent cylinders and the major

axis length, was varied between 1.25 and 4.0. They observed that the angle of attack and cylinder spacing influence the local heat transfer coefficient for elliptic cylinders and concluded that the cylinder spacing and angle of attack should be arranged as small as possible to minimize the drag and to achieve the higher heat transfer. Badr (1998) found the maximum Nusselt number to occur at zero angle of attack.

The tube surface roughness may also have role on heat transfer. Olsson and Sundén (1996) studied the heat transfer and pressure drop characteristics of ten radiator tubes. They concluded that the tubes with rough or enhanced surface provide increased heat transfer than the smooth tubes and also increases related pressure drop. However, there is a tradeoff between the pressure drop and the heat transfer and in many cases the pressure drop may not be larger compared to the benefits of heat transfer gain.

2.1.3 Influence of Number of Tubes, Array, and Tube Banks on Heat Transfer

The possible correlations between single tubes, an array of tubes, and bank of tubes to heat transfer were also examined by a few numbers of researchers. As studied by Žukauskas (1972) and Žukauskas and Ulinskas (1988), the heat transfer for single tubes and banks of tubes is similar but the intensity of the heat transfer of a tube in a bank or in an array can be higher than that of a single tube depending on the arrangement of the tubes. Gnielinski (1979) claimed that the same Nusselt number for a single tube in cross-flow may be valid for the case of a tube in an array in crossflow if the Nusselt number for the single tube is deduced with a Reynolds number in which the mean velocity in the gap between the tubes is used as the characteristic velocity. Žukauskas (1972) reported that the heat transfer increases with the increase of number of tube rows in the flow direction and the increase is almost independent for further increase of rows more than the 5th row.

His work did not report for any effect on heat transfer if the number of column is increased, in other words if the number of tubes in any array or bank is increased. The study of the effect of number of tubes on heat transfer however is scarce.

2.2 Minimizing Pressure drop and Vortex induced vibration using Elliptical Tubes

Many authors reported that, in addition to enhancing heat transfer, an elliptic tube can reduce the pressure drop, the drag coefficient, and vortex induced vibration compared to a circular cylinder. For example, enhanced heat transfer as well as relative pressure drop reduction of up to 25% was observed when utilizing the elliptical arrangement as reported by Brauer (1964). Brauer examined the circular and oval tube banks ($AR = 0.56$) in both in-line and staggered configurations. The Reynolds number, based on tube exterior hydraulic diameter, was investigated from 5500 to 100000 (i.e. from 7900 to 144000 when based on tube major axis length). In addition to observing higher heat transfer, Brauer found that the pressure drop decreases with increasing Reynolds number and with decreasing the gap between two adjacent tubes. Friction factor decreases as the tubes are brought closer. This can be explained that when the tubes come closer, the turbulence area is minimized and thus the pressure drop also minimized. At higher Reynolds number pressure loss decreases because the flow changes from laminar to turbulent zone thereby pushing the boundary layer separation point towards the rear of the tube thereby narrowing the area of turbulence. Additionally it is due to the fact that the entire tube surface is not contracted by the flow. A heat exchanger built from finned elliptical tubes requires less heat transfer surface area and consumes less power for driving fans than an exchanger built from finned circular tubes for a given heat transfer

duty (Schulenberg 1966). Ota et al. (1987) examined the flow around an elliptic cylinder with AR of 0.33 in the Reynolds number range (based on major axis length) from 35000 to 125000. Hassan and Sirén (2004) investigated the heat exchangers, made with circular (AR = 1) and elliptic tubes (AR = 0.32), in the Reynolds number range from 500 to 4000 (when based on streamwise major axis length and approach air velocity). The average pressure drop and hence the friction factor they found to be smaller in elliptic configuration, which is about 46% of that of the circular one. It is obvious from these and other investigation that at crossflow the elliptical tube performs better than the circular configuration in terms of reduced pressure drop and vortex induced vibration.

2.3 Summary of Literature Review

Almost all of the earlier studies on crossflow were dealing with cylinder surface heated by electrical means either for uniform heat flux, such as Laetitia and Kondjoyan (2002) and Ota and Nishiyama (1984) or for constant surface temperature, for instance Badr (1998). Studies on the situation when the tube surface temperature and heat flux may not be considered as uniform are scarce and equally the studies on the airside heat transfer coefficients where the tube surface is cooled or heated by water flowing inside the tube are also limited. Even fewer studies may be found, which quantify and compare the effects of direction of heat flow on the airside heat transfer process, especially for the cases of fluid like air when the Prandtl number is roughly constant. While authors such as Dittus and Boelter (1930), McAdams (1942), Winterton (1998), Cengel (2003), etc. suggest a larger Prandtl exponent for heating the fluid than for cooling it, the role of heat flow direction has not been systematically studied nor postulated based on sound reasoning. On this subject, Scholten and Murray (1995)

studied the effects of direction of heat flow on Nusselt numbers for a gas-particle cross flow over circular tube arrays. Their study mainly deals with the heat transfer mechanism of gas-particle suspension, which does not represent the case of atmospheric airflow.

2.4 Scope of Current Study

The cooling and heating of air, via a single row in-line elliptical tube heat exchanger, were experimentally investigated in this study. The effects of Reynolds number on Nusselt number and the airflow pressure drop across the array were examined. The airside Nusselt numbers for cooling process were compared with those for heating process. The elliptical tube array, with an AR of 0.30, was oriented in a closed loop thermal wind tunnel with airflow parallel to the streamwise major axis length of the tube. Based on the above literature survey, most optimal range of affecting parameters, such as AR, angle of attack, and blockage ratio (BR), was considered in current study. An AR of 0.30 was employed as it falls into the optimal AR range of most studies reviewed above (Eckert and Livingood 1953; Harris and Goldschmidt 2002). The angle of attack was kept at zero degree with the front stagnation point of the tube surface because it is the best flow orientation indicated by Badr (1998). According to Žukauskas (1972), higher BR is not favorable because the C_D and hence the C_{press} goes higher for a BR larger than 0.60. Thus a tube spacing of 6.1 mm (i.e. the surface-to-surface narrowest gap) corresponding to a BR of 0.30 was used. Airside Reynolds number, based on the mean approach air velocity and the streamwise major axis length of the tube, was investigated in the range from 10000 to 36000. This Reynolds number range was chosen because many of the practical heat exchangers run within this flow range (Rahman et al. 2001).

CHAPTER 3

EXPERIMENTAL SETUP AND PROCEDURES

3. EXPERIMENTAL SETUP, PROCEDURES, AND MODELLING OF VELOCITY PROFILE

As portrayed in Figure 3.1, the experimental facility comprises a thermal wind tunnel, and hot and cold water supply systems. The test section is a duct of square cross section, where the experimental single-array in-line elliptical tube heat exchanger is placed in the middle. The details of the test setup and procedures are described below.

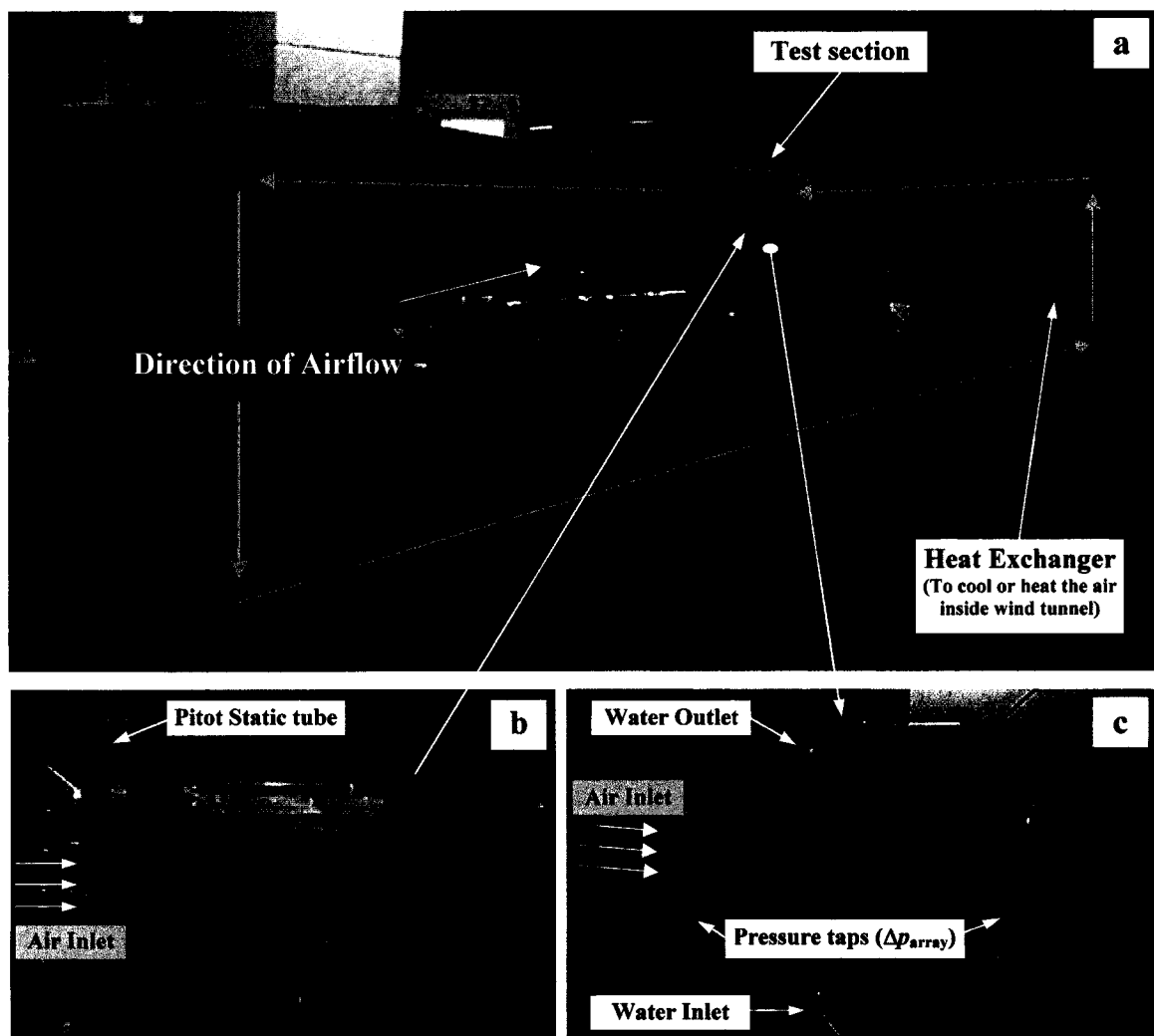


Figure 3.1 (a) Closed-loop Thermal Wind Tunnel, (b) Test section with elliptical tube array (before installation), and (c) Test section (after installation)

3.1 The Thermal Wind Tunnel and the Test Section

The experiments were performed in a closed-loop thermal wind tunnel located in the Essex Hall (Room B05) at the University of Windsor, which is shown in Figure 3.1a. The wind tunnel is 5440 mm (\approx 214 inch) long, 750 mm (\approx 30 inch) wide, and 1640 mm (\approx 65 inch) high with a contraction ratio of 6.25. The air is forced to flow inside the wind tunnel by means of an air blower, which is driven by an electrically powered hydraulic pump. The air velocity is controlled manually by turning a needle valve attached to the hydraulic pump. The arrows in Figure 3.1a show the direction of airflow in the wind tunnel. The system is capable of producing the air velocities of up to 30 m/s without any obstruction and up to 17 m/s in the presence of the elliptical tube array heat exchanger, in the test section. The test section, containing the elliptical tube array heat exchanger, is seen in Figure 3.1b and 3.1c before and after installation respectively. The assembled test section is placed in the upper middle part of the wind tunnel.

3.2 Schematic of the Test Section with Elliptical Tube Array Heat Exchanger

Figures 3.1b and 3.1c display the photographic images of the test duct including the tube array. As illustrated in Figure 3.2.1, the test section is 600 mm long (in the Z direction, i.e. in the direction airflow), 300 mm wide (along the $\pm X$ axis), and 300 mm high (along the $\pm Y$ axis). The test duct was made of Plexiglas having a thermal conductivity of 0.19 W/m. $^{\circ}$ C. The elliptical tubes were drawn from 0.825 mm thick 20.60 mm inner diameter circular copper tubes (ASTM B-88 type-M) with a thermal conductivity of 339 W/m. $^{\circ}$ C. The tubes drawn in this process was not in perfect elliptical shapes, which was considered and described in uncertainty analysis in Appendix A. Each of the formed elliptical tubes was 300 mm long with the outside major and minor axes

lengths of 31.7 mm and 9.7 mm, respectively, giving the minor-to-major axis ratio (AR) of 0.3. The array, consisting of 18 elliptical tubes spaced by 6.1 mm gap (i.e. the surface-to-surface narrowest distance between two adjacent tubes), was oriented in the test section at zero angle of attack, that is, with the major axis parallel (streamwise) and minor axis perpendicular to the direction of airflow. As shown in Figures 3.1b, 3.1c, 3.2.1, and 3.4.6, the tubes were oriented to form an in-line array of heat exchanger to be at cross-flow of air, where the water inlet was at the bottom of the array into the 1st tube and outlet at the top from the 18th tube. The tubes were connected at their ends (outside of the test duct) using small square pockets made of the same Plexiglas material. Two half dummy tubes were placed at the top and bottom of the array to reduce extraneous effects.

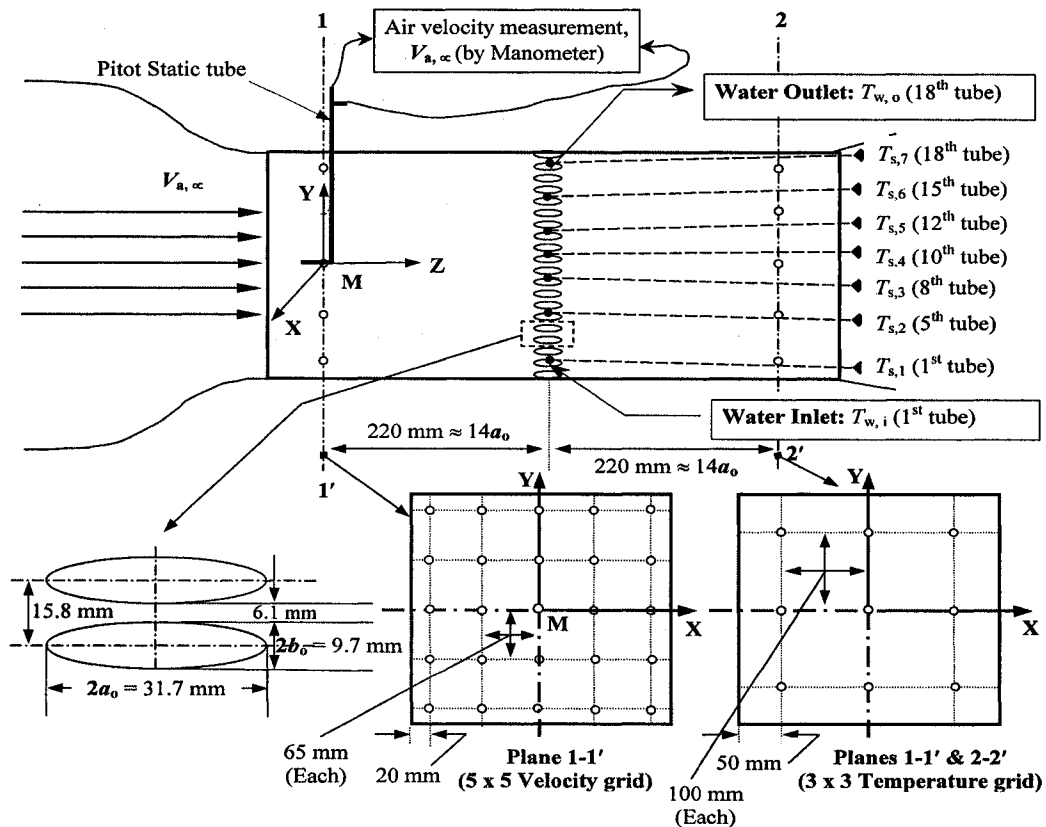


Figure 3.2.1 Schematic of the test section with elliptical tube array - dimensions and measurement setup (drawn not to scale)

3.3 Experimental Methods and Operating Conditions

In the experiments, water was passed through inside the tubes of the array and air was blown over the array, that is, the array is at cross flow of the flowing air. The heat transfer characteristics between the air and the water were investigated in two ways, namely *cooling the air* and *heating the air*. *Cooling the air* means the hot air flowing over the tube array is cooled down by passing cold water inside the tubes of the array. It is the operation when the approach air temperature is higher than that of the water temperature at the array inlet and/or the temperature of the tube surface, i.e. $T_{a,i} > T_{s,o} > T_{w,i}$. *Heating the air* means the cold air flows over the tube array and is heated up by passing the hot water inside the tubes of the array. In this operation the approach air temperature is lower than the inlet water temperature and/or the tube surface temperature, i.e. $T_{a,i} < T_{s,o} < T_{w,i}$.

As shown in Figure 3.1a, a heat exchanger located inside the wind tunnel at the upstream side was the source of cooling and heating the air inside the wind tunnel. The desired free stream inlet air temperature at the test section entrance was achieved by passing the hot or cold water through this heat exchanger and by running the wind tunnel for about 30 to 40 minutes until the airflow is stabilized. Building water supply lines were used as the sources of hot or cold water supplies into the tube array in the test section as well as into the wind tunnel heat exchanger.

The required water temperature through the inlet of the tube array was maintained in two ways. One way, the direct way, was to pass the hot or cold water into the tube directly from the building supplies. In this way, only a single temperature either from the hot supply water or from the cold supply water was possible to achieve, which depended

on the supply line only. Another way was the use of water-mixing chamber (mixing of hot and cold water) attached with the building water supply line, which was specifically built to use in the wind tunnel experiments. The water-mixing chamber had two inlet valves (one for cold and one for hot water intakes from the supply line); one mixing knob, and one outlet valve to pass the mixed water into the tube array. The cold and hot water were mixed in the mixing-chamber to a desired temperature by turning the mixing knob. The mixing-chamber is capable of managing almost any temperature, between the maximum (i.e. the 100% of the hot water) and the minimum (i.e. 100% of the cold water), required for inlet water supply for the tube array. Compared to the air inlet temperature, maintaining the water inlet temperature to a certain fixed value was quite difficult, which largely depended on the fluctuations in the supply line even though the mixing chamber was used. Both methods were used during all experiments and water-mixing method was found to be advantageous, which gave less fluctuation in temperature compared to the direct way.

In both air cooling and heating tests, the airside and waterside flow velocities were varied corresponding to each other to collect several sets of heat transfer data to observe the effects of flow variations (i.e. the Reynolds numbers) on heat transfer (i.e. the Nusselt number). For all the experiments, the inlet temperatures of the air and water, tube outer surface temperature, and the airside and waterside flow velocities were the only major operating parameters to be measured and well taken care of. The experimental operating conditions for both air-cooling and heating tests are given in Table 3.3.1.

Table 3.3.1 Operating Conditions: Air-cooling tests ($T_{a,i} > T_s > T_{w,i}$) and Air-heating tests ($T_{a,i} < T_s < T_{w,i}$)

Controlling Parameters	Experimental Phases			
	Phase-I (Air cooling)	Phase-II (Air heating)	Phase-III (Air cooling)	Phase-IV (Air heating)
Air inlet temperature, $T_{a,i}$	41.5±1.5°C	17.5±1.5°C	–	–
Water inlet temperature, $T_{w,i}$	6.5±1.0°C	38.8±0.8°C	–	–
Air and Water inlet temperature difference, ΔT_{a-w}	–	–	15.7±1.5°C	15.7±1.5°C
Airside Reynolds number (Re_a) – for Inlet Air velocity: $V_a \approx 5 - 17$ m/s	10000 – 33200	10600 – 33500	10300 – 33500	10800 – 36000
Waterside Reynolds number (Re_w) – for water mass flow rate: $\dot{m}_w \approx 0.02 - 0.08$ kg/s	1100 – 3500	1500 – 7300	–	–
Waterside Reynolds number (Re_w) – for water mass flow rate: $\dot{m}_w \approx 0.06 - 0.10$ kg/s	–	–	3300 – 6100	4000 – 7100

3.4 Measurement and Data Collection Procedures

Eight different air velocity steps between 5 and 17 m/s (giving an airside Reynolds number, based on the streamwise major axis length of the tube, from 10000 to 36000) were investigated corresponding to six different water mass flow rates. For the first two experimental phases, i.e. Phase-I and Phase-II, the average water mass flow rates investigated was between 0.02 and 0.08 kg/s, which corresponded to the waterside

Reynolds numbers, based on the tube inner hydraulic diameter, in the range $1100 \leq Re_w \leq 3500$ for cooling, and $1500 \leq Re_w \leq 7300$ for heating tests. For the other two phases, i.e. Phase-III and Phase-IV, the average water mass flow rates examined between 0.06 and 0.10 kg/s that gave the waterside Reynolds numbers, in the range $3300 \leq Re_w \leq 6100$ for cooling, and $4000 \leq Re_w \leq 7100$ for heating tests. The water mass flow rate through the tube array was manually altered to the desired value by turning the main water supply valve while the temperature was adjusted by manipulating the mixing knob. For each water mass flow rate, the air velocity was varied by manually adjusting the needle valve of the hydraulic pump attached with the wind tunnel. By doing this, 24 data sets for air-cooling and another 24 data sets for air heating tests were gathered for analysis. Every effort was given to ensure that the system is stabilized before starting the data collection, even though during the experiment and data collection process some fluctuations in water supply as well as its temperature were observed that resulted the water and air temperatures to fluctuate slightly. To take these variations into account, during each experiment (for each setting of water mass flow and air velocity), three to four data samples for each of the parameters were collected. Then the mean of the samples was taken as follows

$$H = \frac{1}{n} \sum_{j=1}^n H_j, \quad (3.4.1)$$

where, H , as applicable, represents any of the measured tube dimensions (e.g. $2a_i$, $2b_i$, $2a_o$, $2b_o$, S , and L_t) or experimental parameters (e.g. T_a , ΔT_a , T_w , ΔT_w , ΔT_s , Δp_{pitot} , Δp_{array} , and \dot{m}_w); j is the counter of repeated measurements; and n is the total number of repeated data readings.

3.4.1 Air, Water and Tube side Temperature Measurements

All temperatures were measured using type-T thermocouples and a hand-held OMEGA HH506R digital thermometer. Before each experiment, the temperature readings of all the thermocouples were calibrated and adjusted with respect to one chosen thermocouple probe located at water inlet side. The thermometer had an uncertainty of $\pm(0.2^\circ\text{C}+0.05\%$ of the reading). For a highest temperature of 50°C , the overall uncertainty in the temperature measurement was estimated to be $\pm 1.03^\circ\text{C}$, which includes the errors in reading together with the errors in thermometer and the thermocouple probes. The thermometer had a differential reading function by which, where applicable, the temperature differences such as $\Delta T_w = |T_{w,i} - T_{w,o}|$ and $\Delta T_a = |T_{a,i} - T_{a,o}|$, were measured directly. This correlated measurement helped damp out bias errors leaving only some precision errors, which account for about $\pm 0.10^\circ\text{C}$ for each of the ΔT_a , ΔT_{a-s} , ΔT_{a-w} , ΔT_w , and ΔT_{w-s} measured.

Measurement of Airside Temperatures ($T_{a,i}$, $T_{a,o}$, ΔT_a , and ΔT_{a-s})

Sufficient time (roughly 30 to 40 minutes) was allowed to ensure the circulating air inside the wind tunnel to stabilize to the desired temperature. As extended in Figure 3.2.1, two cross sections (Planes 1-1' and 2-2'), approximately $14a_o$ upstream and downstream of the array, were chosen to measure the approach (upstream) and downstream air temperatures $T_{a,\infty}$ and $T_{a,o}$ respectively. At the beginning of each experiment, the upstream and downstream air temperatures were measured at 9 locations (horizontally and vertically evenly spaced 3 x 3 grid points) over the cross sections at Planes 1-1' and 2-2'. These measurements were taken to obtain the temperature profiles

of the approach air at the inlet of the test section. The approach air temperature profiles were found to be quite uniform, which could be fairly represented by a single point measurement at the inlet. The downstream air temperature profile, however, was not found to be as flat as upstream. So, during the subsequent experiment, the mean approach air temperature ($T_{a,i}$) at the inlet was measured at a single point location at Position M (middle center, see Figures 3.2.1 and 3.4.6) and the downstream air temperature ($T_{a,o}$) at 9 locations around the cross-section at Plane 2-2'. The downstream air temperature ($T_{a,o}$) was recorded as

$$T_{a,o} = \frac{1}{N} \sum_{j=1}^N [T_{a,o}]_j, \text{ where } N = 9. \quad (3.4.2a)$$

The maximum deviation of $T_{a,o}$ from the mean value of its 9 grid points was found no more than $\pm 5\%$ for all the experiments. The mean temperature difference between the air inlet and outlet, was measured as

$$\Delta T_a = \frac{1}{N} \sum_{j=1}^N \left[\frac{1}{n} \sum_{j=1}^n |T_{a,i} - T_{a,o}|_j \right], \text{ where } N = 9 \text{ and } n = 3 \text{ to } 4 \text{ repeats.} \quad (3.4.2b)$$

Similarly, the mean temperature difference between the air inlet and the tube outer surface was estimated as

$$\Delta T_{a-s} = \frac{1}{N} \sum_{j=1}^N \left[\frac{1}{n} \sum_{j=1}^n |T_{a,i} - T_{s,o}|_j \right], \text{ where } N = 7 \text{ and } n = 3 \text{ to } 4 \text{ repeats.} \quad (3.4.2c)$$

Measurement of Waterside Temperatures ($T_{w,i}$, $T_{w,o}$, and ΔT_w)

Water inlet temperature ($T_{w,i}$) at the entrance of the 1st tube and the outlet temperature ($T_{w,o}$) at the exit of the array at the 18th tube (Figures 3.1 and 3.2.1) were

measured by inserting two thermocouple probes inside the tube. For each experimental run, about 3 to 4 repeated readings were recorded to take their mean as

$$T_{w,i} = \frac{1}{n} \sum_{j=1}^n [T_{w,i}]_j \text{ and } T_{w,o} = \frac{1}{n} \sum_{j=1}^n [T_{w,o}]_j, \text{ where } n = 3 \text{ to } 4 \text{ repeats.} \quad (3.4.3a)$$

The mean temperature difference between the water inlet and outlet was measured as

$$\Delta T_w = \frac{1}{n} \sum_{j=1}^n |T_{w,i} - T_{w,o}|_j, \text{ where } n = 3 \text{ to } 4 \text{ repeats.} \quad (3.4.3b)$$

Tube Side Temperature Measurement ($T_{s,o}$)

As shown in Figures 3.2.1 and 3.4.2, seven thermocouple probes were affixed on the outside top surface of the tubes at various locations counting from the bottom to the top of the array (excluding the two dummy half tubes). One at the entrance of the 1st tube, one at the exit of the 18th tube, and other five thermocouple probes were located spanwise middle of the 5th, 8th, 10th, 12th, and 15th tubes of the array. The average outside tube surface temperature ($T_{s,o}$) for all the 18 tubes was estimated from measured individual surface temperature of seven locations as follows

$$T_{s,o} = \frac{1}{N} \sum_{J=1}^N \left[\frac{1}{n} \sum_{j=1}^n [T_{s,o}]_j \right]_J, \text{ where } N = 7 \text{ and } n = 3 \text{ to } 4 \text{ repeats.} \quad (3.4.4)$$

This averaging approach was reasonable because the variation of the tube surface temperature from entry to exit was quite linear, which can be seen in Figure 3.4.1 for two sample test cases (for both cooling and heating tests).

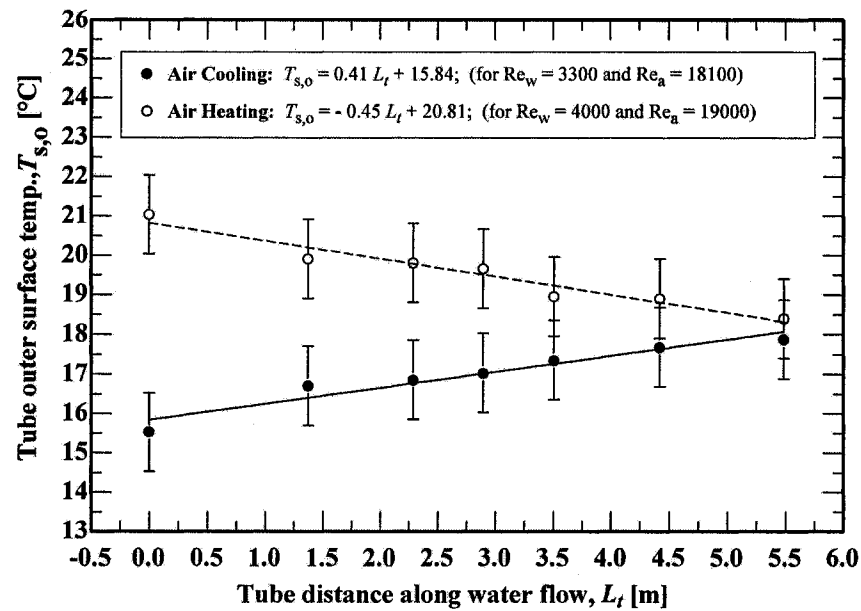


Figure 3.4.1. Sample $T_{s,o}$ variation in the direction of water flow (error bars are shown)

3.4.2 Airside Velocity, Mass flow rate, and Pressure drop Measurements

For each of air velocity, mass flow rate, and pressure drop across the tube array, the basic independent parameter, i.e. the pressure difference, was measured using a handheld digital manometer, Dwyer series 475 Mark III. The manometer had an accuracy of $\pm 1.5\%$ of the reading in Pa, which was considered to be the bias error for manometer.

Measurement of Approach Air Velocity (V_a)

The air velocity in terms of dynamic pressure was measured by means of a 2.38 mm Pitot static tube along with the digital manometer as mentioned above. The manometer reads the pressure difference (Δp_{pitot}) between the static and total pressure ports, which can be seen in Figures 3.2.1 and 3.4.1. Following Equation 3.4.1, the mean airside dynamic pressure for each experiment was calculated as follows

$$\Delta p_{\text{pitot}} = \frac{1}{n} \sum_{j=1}^n [\Delta p_{\text{pitot}}]_j, \text{ where } n = 3 \text{ to } 4 \text{ repeats,} \quad (3.4.5a)$$

and the mean inlet air velocity could be estimated from the following relation,

$$V_a = 0.875 C' \sqrt{\frac{2\Delta p_{\text{pitot}}}{\rho_a}}, \quad (3.4.5b)$$

where 0.875 is a geometric factor introduced to account for the boundary layer effect (discussed below), C' is the design correction constant depends on the spacing of the static pressure holes, and ρ_a is the density of air. To compare to a standard round junction Pitot static tube, $C' = 1.003$ was introduced in the current study for the distances of $3.9D$ from the static pressure ports to the total pressure port at the tip and $9.8D$ from the static pressure ports to the centerline of the stem (as per Flow Kinetics LLC, 2002).

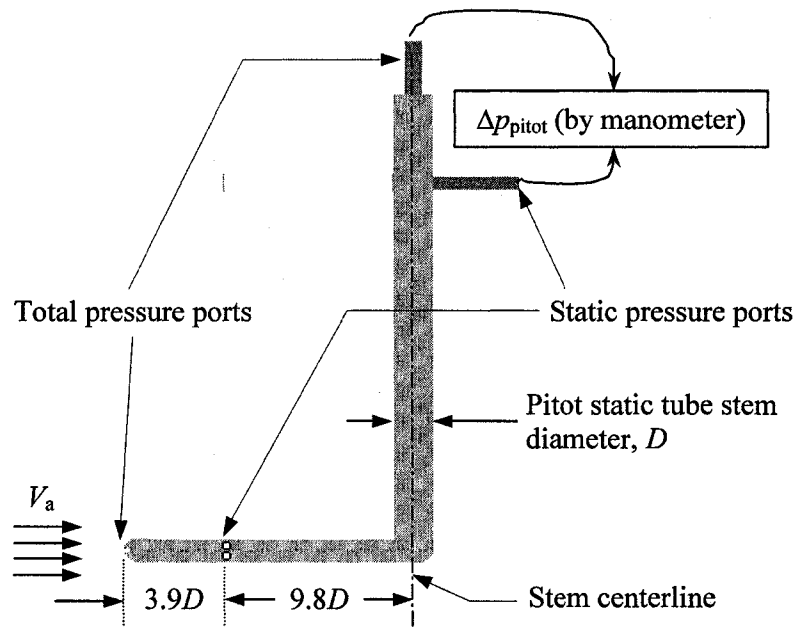


Figure 3.4.2 Pitot static tube with stem diameter $D = 2.38$ mm (drawn not to scale)

As detailed in Figure 3.2.1, a cross section (Plane 1-1'), approximately $14a_0$ upstream of the tube array, was chosen to measure the profile of the approach air velocity ($V_{a,\infty}$) at the test section inlet. At the beginning of the experiment, the approach air velocity ($V_{a,\infty}$) outside the boundary layer, in the presence of the tube array, was measured at 25 locations (horizontally and vertically evenly spaced 5×5 grid points), over the cross section at Plane 1-1'. This was performed by traversing the Pitot static tube over each grid point. The grid point velocity measurements were performed at three different nominal air velocity settings, such as at 5.0, 10.8, and 16.5 m/s. In all cases, the velocity profiles were observed to be reasonably flat for the entire cross section outside the boundary layer, with a maximum deviation of about $\pm 4.5\%$ from the mean. For plotting the velocity profiles for the entire cross section, the measurements were extended beyond the 5×5 grid points to cover the distance up to the test section wall (i.e. the boundary layer). The boundary layer thickness was roughly identified by observation during the measurement. It was the point where nominal velocity starts decreasing and drops to zero at the test section wall. The number and locations of the measuring points were chosen randomly. Around the test section wall, a linear variation of the air velocity in the boundary layer was assumed and this effect was taken into account by introducing a geometric factor of 0.875 in Eq. (3.4.5b).

The air velocity profile, along the Plane 1-1', was generated by plotting the velocity in the Z direction against the distance along X - Y coordinate (see Figure 3.2.1). For visualization, the velocity profiles are presented in Figures 3.4.2 to 3.4.4. It was found that a single point measurement at the middle of the test section inlet could fairly represent this uniform velocity profile for the area outside the boundary layer. It is noted here that the boundary layer thickness around the test section wall was found to be

roughly 0.20 mm. Thus, during the subsequent experiments, the mean upstream air velocity (V_a) was measured at a single point location at Position M (see Figure 3.2.1). The uncertainties in the air velocity measurements were estimated to be no more than $\pm 4.0\%$ of the measured values for both air-cooling and heating tests.

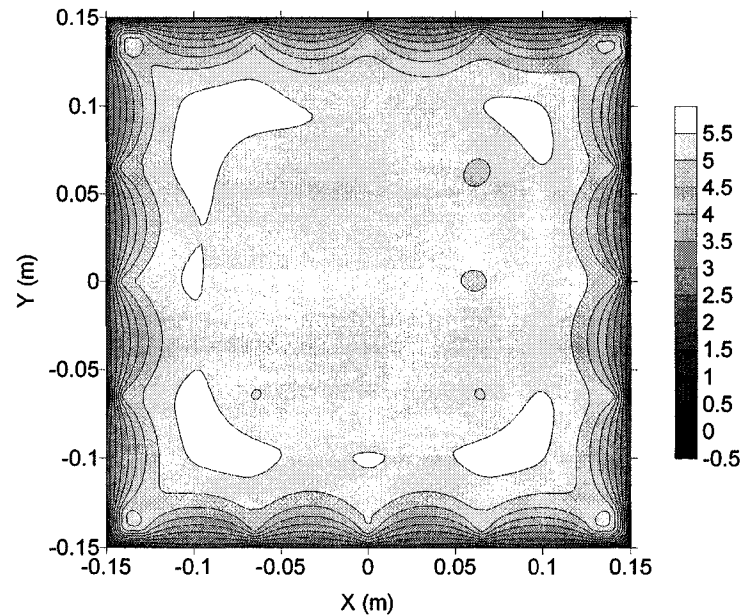


Figure 3.4.3a Air velocity at the test inlet section (5 x 5 grid point measurement: $V_a = 5.0$ m/s; maximum deviation from the mean = $\pm 4.5\%$) – Contour

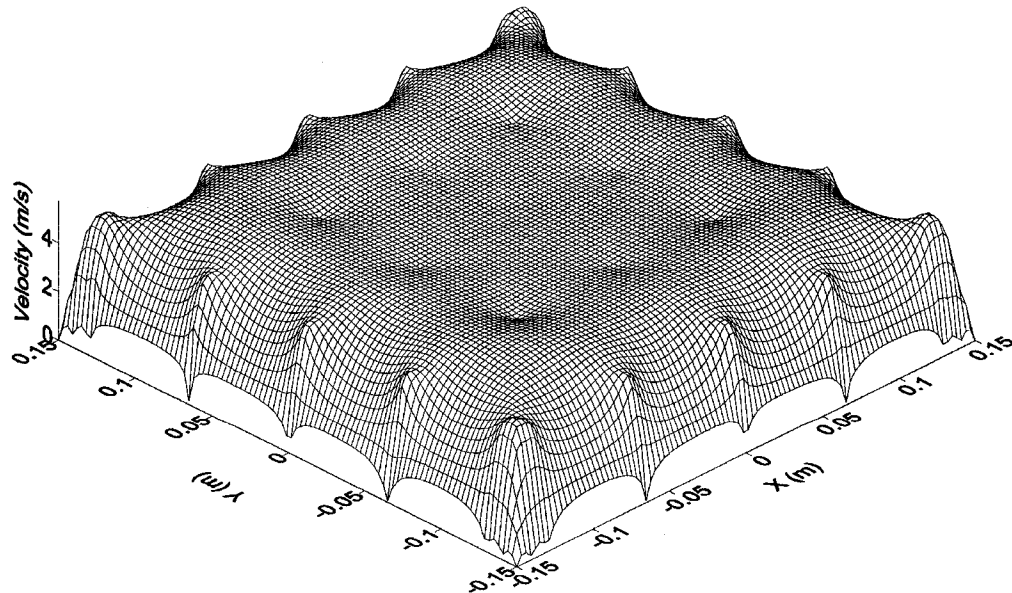


Figure 3.4.3b Air velocity at the test inlet section (5 x 5 grid point measurement: $V_a = 5.0$ m/s; maximum deviation from the mean = $\pm 4.5\%$) – 3D Plot

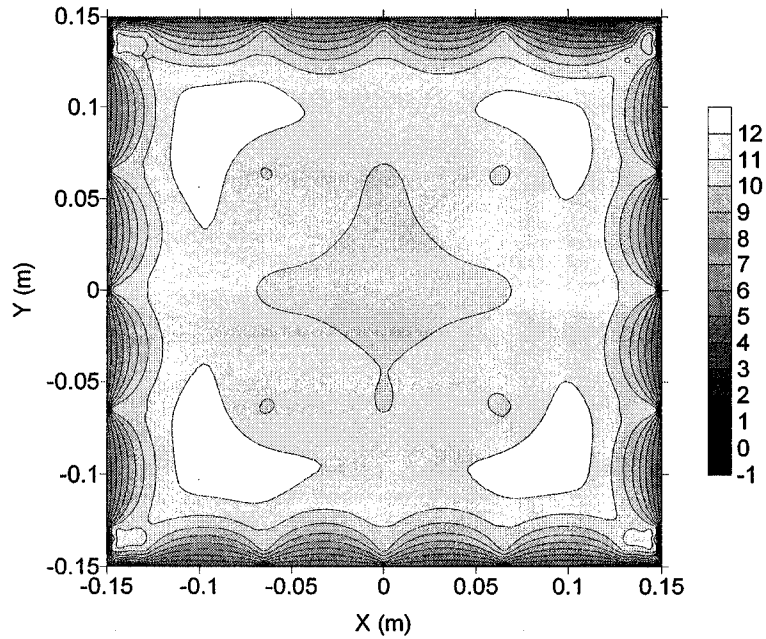


Figure 3.4.4a Air velocity at the test inlet section (5 x 5 grid point measurement:
 $V_a = 10.8$ m/s; maximum deviation from the mean = $\pm 1.5\%$) – Contour

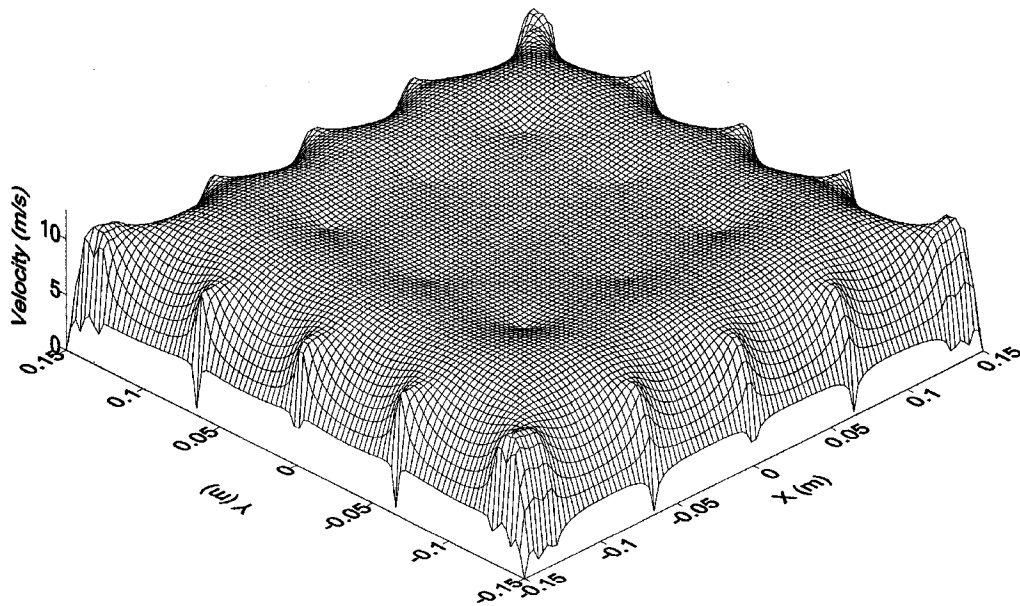


Figure 3.4.4b Air velocity at the test inlet section (5 x 5 grid point measurement:
 $V_a = 10.8$ m/s; maximum deviation from the mean = $\pm 1.5\%$) – 3D Plot

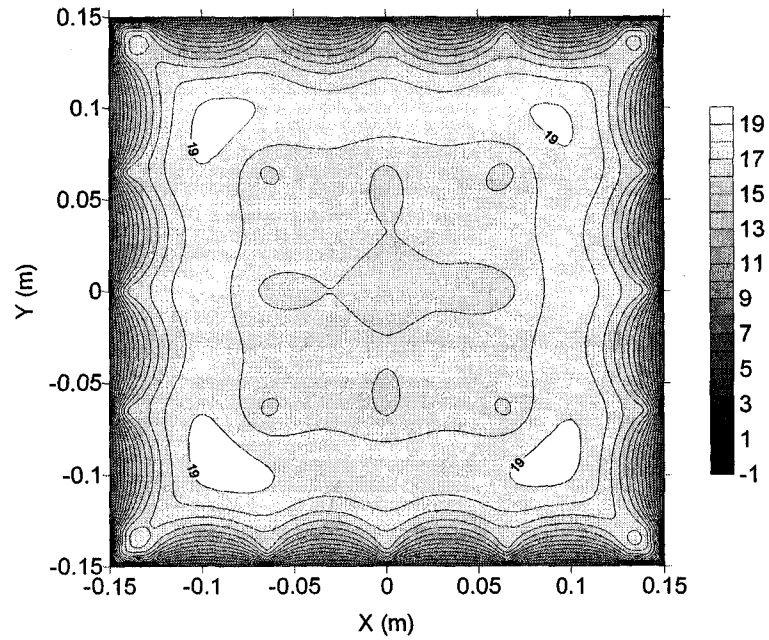


Figure 3.4.5a Air velocity at the test inlet section (5 x 5 grid point measurement: $V_a = 16.5$ m/s; maximum deviation from the mean = $\pm 2.6\%$) – Contour

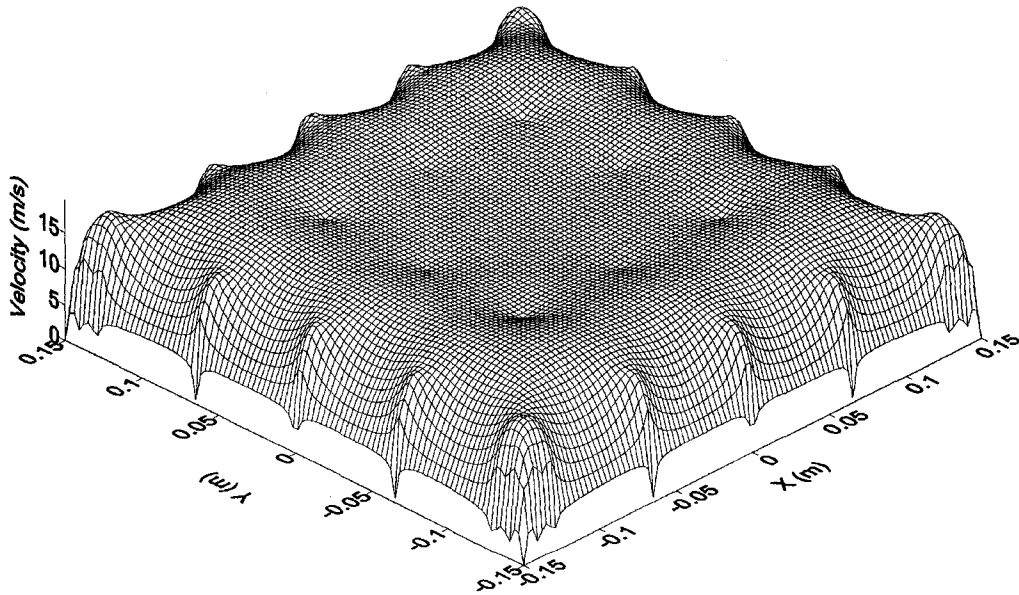


Figure 3.4.5b Air velocity at the test inlet section (5 x 5 grid point measurement: $V_a = 16.5$ m/s; maximum deviation from the mean = $\pm 2.6\%$) – 3D Plot

Estimation of Airside Mass flow rate (\dot{m}_a)

The mean velocity of approach air at the test section inlet was used to estimate the airside mass flow rate. By applying the principle of conservation of mass, the airside mass flow rate was deduced using the following relation

$$\dot{m}_a = \rho_a A_{\text{duct}} V_a, \quad (3.4.5)$$

where A_{duct} is the cross-sectional area of the test section duct at inlet, i.e. along Plane 1-1' as shown in Figure 3.2.1.

Measurement of Airside Pressure drop across the Tube Array (Δp_{array})

Six pressure taps (3 pairs) were drilled to measure the airflow pressure drop across the array, which are shown in Figure 3.4.6. The pressure drops across the tube array (Δp_{array}) were measured along the pressure tap pairs of A-A', B-B', and C-C' using the same manometer as used in air velocity measurement. As discussed in section 5.1.5, the data along taps B-B' was used in the analysis. The uncertainty in the pressure drop measurement across taps B-B' was estimated to be within $\pm 9.0\%$ of the measured value.

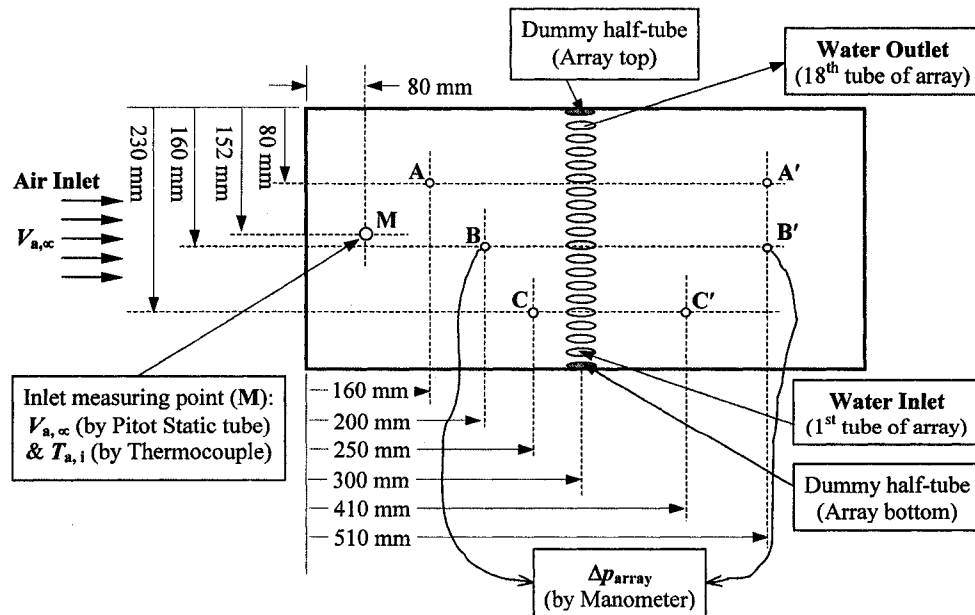


Figure 3.4.6 Experimental domain with pressure measurement taps (drawn not to scale)

3.4.3 Waterside Mass flow rate (\dot{m}_w) and Velocity (V_w) Measurements

Measurement of Waterside Mass flow rate (\dot{m}_w)

The water mass flow rate inside the tubes of the array was measured several times during each experimental run. The mean of the repeated measurements was taken according to the following relation,

$$\dot{m}_w = \frac{1}{n} \sum_{j=1}^n \left[\frac{m_w}{t} \right]_j, \text{ where } n = 3 \text{ to } 4 \text{ repeats.} \quad (3.4.6)$$

Here m_w is the water mass (kg) collected in time t second. The total uncertainties in the measurement of water mass flow rate, including some fluctuations in the water supply line, were approximately $\pm 1.5\%$ of the measured values for both cooling and heating experiments.

Estimation of Water Velocity (V_w)

The mean velocity of water inside the tube was calculated from the mass conservation principles as follows

$$V_w = \frac{\dot{m}_w}{\rho_w A_{c,i}}, \quad (3.4.7)$$

where $A_{c,i}$ is the inner tube cross sectional area.

CHAPTER 4

THEORETICAL CONSIDERATIONS AND DATA REDUCTION

4. THEORETICAL CONSIDERATIONS AND DATA REDUCTION

The experiments were performed depending on the available testing facilities and the existing limitations and on some considerations as described below. The reduction of the data was based on the analysis of theoretical background of heat transfer and fluid flow, which are explained in the following subsections.

4.1 Evaluations of Thermophysical Properties of the Air and Water

If not mentioned otherwise, the thermophysical properties for both air cooling and heating tests were taken at film temperature ($T_{f,a}$) for air and at bulk temperature ($T_{w,b}$) for water. Considering a linear variation of temperature between the outer surface of the tubes and the approach air, the air film temperature was deduced as follows

$$T_{f,a} = \frac{T_{a,i} + T_{s,o}}{2}. \quad (4.1.1)$$

Similarly, the bulk temperature of the flowing water inside the tubes was defined as the arithmetic average of the water inlet and outlet temperatures as

$$T_{w,b} = \frac{T_{w,i} + T_{w,o}}{2}. \quad (4.1.2)$$

To deduce the airside heat transfer rate using Eq. (4.5.2a), not shown yet, the air property was evaluated at bulk temperature. Some of the literatures referred in this thesis also evaluated the airside properties at bulk temperature. Thus, where appropriate, the air properties were evaluated at airside bulk temperature, which was defined as follows

$$T_{a,b} = \frac{T_{a,i} + T_{a,o}}{2}. \quad (4.1.3)$$

4.2 Assumptions made in the Experiments and Data reduction

The following situations were considered during the experiments and data reduction.

1. *Steady state airflow inside wind tunnel.* To ensure this assumption, before conducting each experimental phase the wind tunnel was run for approximately 30 to 40 minutes until the airflow reached to the desired temperature at the inlet of the wind tunnel test section.
2. *Negligible conductive heat transfer between the room and the tube array ($q_{\text{conduction}} \approx 0$).* The test section walls were constructed with thick Plexiglas material having very low thermal conductivity of 0.19 W/m.°C, which justifies this assumption.
3. *No or negligible radiative heat transfer between the room and the test section wall.* This assumption was valid because the room temperature was the same as the outside temperature of the test section walls, which results virtually no temperature difference and hence no radiative heat transfer.
4. *Negligible radiative heat transfer between the air and the outside surface of the tubes.*
5. *No condensation effect on airside heat transfer.*

The validity of the assumptions 4 and 5 have been quantified and explained in Section 4.5 below.

4.3 Key Dimensionless Parameters

Heat transfer and fluid flow to and from any object or surface are essentially dependent on some dimensionless key parameters. This heat transfer rate is generally represented by a non-dimensional heat transfer coefficient, which is termed as the Nusselt

number (Nu). The Nusselt number, defined as the ratio of the convection to the conduction heat transfers, is dependent on at least two independent key parameters such as the Reynolds number and the Prandtl number. Before defining Nu in greater details, the independent key parameters, on which Nu depends, need to be defined first. The Reynolds number (Re) determines the flow velocity and characterizes the nature of the flow and the Prandtl number (Pr) describes the development of boundary layer thickness over the surface, which is the barrier to the heat transfer. There are other two important parameters involved in current study. One is the Grashof number (Gr) that identifies the existence of natural convection, and the other is the Pressure Coefficient (C_{press}), which is used to quantify the airflow pressure drop across the tube array. The Nu is defined in greater detailed in section 4.4 below and the independent key parameters are defined first in this section.

Reynolds Number (Re):

The Reynolds number, named after Osbourne Reynolds - a British engineer and physicist, is defined as the ratio of the inertial force to the viscous force within the flowing fluid. It is used in momentum, heat, and mass transfer to account for the dynamic similarity and to characterize the nature of the flow and is normally defined in the following form

$$Re = \frac{\text{Inertia Force}}{\text{Viscous Force}} = \frac{\text{Mass} \times \text{Acceleration}}{\text{Shear Stress} \times \text{Area}} = \frac{\rho AV^2}{\mu \frac{V}{Z} A} = \frac{\rho VZ}{\mu} = \frac{VZ}{\nu}, \quad (4.3.1)$$

where the characteristic length, Z , was replaced by the streamwise outer major axis length of the tube, i.e. $2a_0$ for airside and by the inner hydraulic diameter of the tube, i.e. $D_{h,i}$ for waterside. Typically, viscous stresses within a fluid tend to stabilize and organize the

flow, whereas excessive fluid inertia tends to disrupt organized flow leading to chaotic turbulent behavior. Thus, Reynolds number governs the flow regime in forced convection. The estimation of the airside Re using Eq. (4.3.1) is for a single tube in an array or bank. It is a common practice in heat exchanger design to call a column of tubes (i.e. vertical stack of tubes) as a single row of tubes. So, for a single row of tubes the Re can be estimated as follows (Brauer 1964; Sparrow and Ramsey 1978; Gnielinski 1985)

$$\text{Re}_{a,\text{array}} = \frac{V_{a,\text{max}} Z_a}{\nu_a}, \quad (4.3.2)$$

where $V_{a,\text{max}}$ is the mean airflow velocity at the narrowest gap between two adjacent tubes in the array, which is deduced as follows

$$V_{a,\text{max}} = \frac{S_c}{S_T} V_a = \left(\frac{S_T + 2b_o}{S_T} \right) V_a = \psi V_a. \quad (4.3.3)$$

The characteristic length in Eq. (4.3.2), Z_a , depending on the comparable correlations in the literature, can be taken to be either $2a_o$ or the maximum perimeter that directly faces the airflow, which in the case of current study is $P_o/2$ (Žukauskas, et al. 2002). In current study, the characteristic length for airside was used as $2a_o$. The $\text{Re}_{a,\text{max}}$ given in Eq. (4.3.2) was not used in current study, however, it can be used to compare the heat transfer and fluid flow data of a single tube row with the similar one in the literature.

Prandtl Number (Pr):

It is named after Ludwig Prandtl – a German scientist who pioneered the concept of boundary layer in 1904 and significantly contributed to the field of boundary layer theory. The Prandtl number, Pr, is defined as the ratio of the momentum diffusivity to the thermal diffusivity. It is generally defined in the following form

$$\text{Pr} = \frac{\text{Momentum Diffusivity}}{\text{Thermal Diffusivity}} = \frac{\nu}{\alpha} = \frac{\mu/\rho}{k/\rho c_p} = \frac{\mu c_p}{k}. \quad (4.3.4)$$

For the heat transfer in general and free and forced convection analysis in particular, the convection heat transfer rate anywhere along the surface of any body is directly related to the temperature gradient at that location. The fluid flow velocity has a strong influence on the temperature profile, and hence the development of the velocity boundary layer relative to the thermal boundary layer has strong effect on the convection heat transfer.

For the laminar flow, the relative thickness of the velocity and the thermal boundary layers is best described by the Prandtl number in the following form

$$\text{Pr} = \left(\frac{\delta_{\text{velocity}}}{\delta_{\text{thermal}}} \right)^{1/n}, \quad (4.3.5)$$

where the exponent n is taken to be $1/3$ and the velocity boundary layer thickness, δ_{velocity} , is obtained in terms of local Re and corresponding to the local distance from the leading edge (Incropera and DeWitt 2002). For laminar flow, Pr provides a measure of the relative effectiveness of momentum and energy transport by diffusion in the velocity and thermal boundary layers. The larger the free stream velocity, the thinner the velocity boundary layer is. Compared to the momentum, the heat diffusion is quicker in fluids with $Pr \ll 1$, and slower in fluids with $Pr \gg 1$ (Cengel 2003). Consequently, relative to the velocity boundary layer, the thermal boundary layer is thicker for fluids with $Pr \ll 1$ and thinner for fluids with $Pr \gg 1$. In turbulent flow, the boundary layer development is influenced strongly by the random fluctuations in the fluid and not by the molecular diffusion, and hence, the relative boundary layer growth does not necessarily depend on the value of Pr . In such cases, $\delta_{\text{velocity}} \approx \delta_{\text{thermal}}$, and the turbulent Prandtl number in the form of the ratio of energy of fluctuating components is used.

Grashof Number (Gr):

The Grashof number is defined as the ratio of the buoyancy force to the viscous force acting on the fluid. For forced convection the Reynolds number dictates the flow regime and for natural convection the Grashof number governs the flow regime. For a flow, it determines whether the forced convection or the natural convection is dominant and is given by

$$\text{Gr} = \frac{\text{Buoyancy Forces}}{\text{Viscous Forces}} = \frac{g(\Delta\rho)(\text{Volume})}{\rho\nu^2} = \frac{g\beta\Delta T(\text{Volume})}{\nu^2} = \frac{g\beta\Delta TZ^3}{\nu^2}, \quad (4.3.6)$$

where, $\beta = \beta_a = \frac{1}{T_{f,a} + 273.15} [K^{-1}]$, $\Delta T = \Delta T_{a-s} = |T_{a,i} - T_{s,o}| [^{\circ}C]$, and $Z = Z_a = 2a_o [m]$

for airside and $\beta = \beta_w = \frac{1}{T_{w,b} + 273.15} [K^{-1}]$, $\Delta T = \Delta T_{w-s} = |T_{w,b} - T_{s,i}| [^{\circ}C]$, and

$Z = Z_a = D_{h,i} [m]$ for waterside.

Pressure Coefficient at Airside (C_{press}):

According to Brauer (1964), Merker and Hanke (1986), and Gaddis and Gnielinski (1997), the pressure coefficient (C_{press}) is generally described by the ratio of the static pressure drop of the airflow across the tube array (Δp_{array}) to the dynamic pressure of the flowing air. For the current experiment, the following non-dimensional expression defines the airflow pressure drop coefficient for a single tube in the array (Khan et al. 2004a)

$$C_{\text{press}} = \frac{\Delta p_{\text{array}}}{\Delta p_{\text{pitot}} N_T} = \frac{\Delta p_{\text{array}}}{\frac{1}{2} \rho_a V_a^2 N_T}, \quad (4.3.7)$$

Equation (4.3.7) is used to determine the pressure coefficient for a single tube in an array or tube bank. However, to deduce the pressure coefficient for a single row of tubes (i.e. the column of tubes perpendicular to the airflow), the following relation was used in the calculation (Brauer 1964; Sparrow and Ramsey 1978; Gnielinski 1985)

$$C_{\text{press,array}} = \frac{\Delta p_{\text{array}}}{\frac{1}{2} \rho_a V_{a,\text{max}}^2}, \quad (4.3.8)$$

where $V_{a,\text{max}}$ is taken from Eq. (4.3.3). This pressure drop coefficient determines the power required to pump the air across the array at the desired flow rate. The lower the pressure coefficient the less the power requirement is.

4.4 Representation of Heat Transfer – the Nusselt Number (Nu)

A convenient method of quantifying the heat transfer to and from any object or surface is through a dimensionless parameter, the Nusselt Number (Nu). This is a dimensionless form of the heat transfer coefficient (h) and was named after Ernst Kraft Wilhelm Nusselt who is one of Germany's notable heat transfer luminaries. As said before, the Nusselt number is the ratio of the convection to the conduction heat transfer rates. In other words, it is the ratio of the fluid layer resistance to the convective resistance and is generally represented by

$$\text{Nu} = \frac{\text{Fluid layer resistance}}{\text{Convective resistance}} = \frac{Z/k}{1/h} = \frac{hZ}{k}, \quad (4.4.1)$$

where k is the thermal conductivity, h is the convection heat transfer coefficient of the participating fluid, and Z is the characteristic length depends on the shape and orientation of the heat transfer surface. In the current study, this Z was replaced by the streamwise

major axis length of the tube, i.e. $Z_a = 2a_o$, for airside (external flow) analysis and by the inner side hydraulic diameter of the tube, i.e. $Z_w = D_{h,i}$, for waterside (internal flow) analysis. If the heat transfer coefficient, h , is known, the Nusselt number can be readily estimated using Eq. (4.4.1). In real world applications, however, different body shapes and heat transfer surfaces are used. In such cases, h may not be known priori and in most cases, it is estimated by experimental investigation (e.g. from the heat balance) or from other suitable observation or from available correlations. In present study, the h for airside and waterside were deduced from the heat balance and the Nu for airside and waterside were estimated separately using Eq. (4.4.1). The heat balance analyses are described and presented in Section 4.5 below. The nature of dependency of experimentally estimated Nu on other parameters was also compared in the light of available correlations.

From the established literature in this area, it is well known fact that the heat transfer either for a single tube, a tube in a row or bank, or for a tube row is influenced by the flow velocity, thermophysical properties of the fluid, heat flux intensity, heat flux direction, and the arrangement of the tubes. Thus most of the heat transfer correlations available are in the form of dimensionless heat transfer coefficient, i.e. the Nu with its functional dependency on the influencing parameters such as the Reynolds number (Re), Prandtl number (Pr), thermophysical properties, and tube arrangement. As per Žukauskas (1972), for the current experimental situation, the dimensionless relation can be represented by

$$\text{Nu} = f \left(\text{Re}, \text{Pr}, \frac{\mu}{\mu_s}, \frac{k}{k_s}, \frac{c_p}{c_{p,s}}, \frac{\rho}{\rho_s}, \frac{S_c}{Z}, \frac{Z}{L} \right). \quad (4.4.2)$$

In current study, for the external flow at airside the arrangement of the tubes, i.e. the factor S_c/Z , was fixed, that means the effect of the variation of S_c/Z on Nu was not included. Also for the internal flow at waterside, the effect of the variation of the geometric factor, Z/L , on Nu was excluded. This is because the factor Z/L accounts for the effect on local Nu, whereas the overall mean Nu was estimated in current study, which covers all the local effects. Thus, from the dimensional analysis, it is found for the forced convection heat transfer, that, the overall mean Nu depends mainly on the flow velocity represented by Re and the boundary layer thickness, which is taken care of by Pr. For the generalization of experimental data, taking main factors into account, the following power law relationship is commonly used for the case of fluid flow over cylinder (Žukauskas and Ulinskas, 1988)

$$\text{Nu} = y \text{Re}^m \text{Pr}^n \left(\frac{\text{Pr}_b}{\text{Pr}_s} \right)^p, \quad (4.4.3a)$$

where y is the coefficient and m , n , and p are the exponents, the values of which are determined by experimental analysis and curve fitting. Depending on the character of the temperature profile in the thermal boundary layer determined by the Pr, usually $n = 1/3$ is used as the exponent of Pr in Eq. (4.4.3a). However, for a variety of flow conditions, from an intensive study of different tubes in cross flow of various kinds of fluids, Žukauskas (1972) proposed the Pr exponent n in Eq. (4.4.3a) to be 0.37 for $\text{Pr} < 10$ and 0.36 for $\text{Pr} > 10$. The factor Pr_b/Pr_s is introduced in Eq. (4.4.3a) to account for the effect of the direction of heat flow (i.e. the heating or cooling of the fluid) in the case of temperature-dependent fluid properties. For the case of air as a gas flow where the Pr is less than unity and almost constant for the range of temperature considered in the experiment, the factor Pr_b/Pr_s turns to unity and can be ignored. Thus for the external

flow, i.e. the air flow over the tubes of the array in the case of current study, the relation in Eq. (4.4.3a), with reasonable accuracy, can be further simplified to give

$$\text{Nu} = y \text{Re}^m \text{Pr}^n, \quad (4.4.3b)$$

where again the exponent of Pr in general is taken to be $n = 1/3$ in most cases.

The factor Pr_b/Pr_s in Eq. (4.4.3a) increases with the increase of temperature head. The effect of the variation of thermophysical properties of a viscous liquid in the thermal boundary layer of a tube is sometimes accounted for by the ratios of $\frac{\mu}{\mu_s}$, $\frac{k}{k_s}$, $\frac{c_p}{c_{p,s}}$. In moderately viscous fluid flow like water, it is mainly the viscosity that changes with temperature across the boundary layer, and therefore in such case the factor Pr_b/Pr_s in Eq. (4.4.3a) can be replaced by the factor μ_b/μ_s (Žukauskas and Ulinskas 1988). For the internal pipe flow, i.e. the water flow inside the tubes in the case of current study, Eq. (4.4.3a) can be re-written as follows

$$\text{Nu} = y \text{Re}^m \text{Pr}^n \left(\frac{\mu_b}{\mu_s} \right)^p. \quad (4.4.4a)$$

Without much error, Eq. (4.4.4a) can also be simplified to give

$$\text{Nu} = y \text{Re}^m \text{Pr}^n, \quad (4.4.4b)$$

where again the exponent of Pr here is taken to be $n = 1/3$ in general. Equation (4.4.4b) is the form of generalized Dittus-Boelter Equation (Dittus and Boelter, 1930) for internal liquid pipe flow as reviewed and explained by Winterton (1998), where, for water flow, the exponent n is recommended to be 0.4 for heating the water and 0.3 for cooling the water. Although the main focus of current study was to deduce the airside Nu–Re

relationship, the waterside Nu–Re relationship is also of interest to know, and thus from the experimental data, the correlation for both airside and waterside was developed in the following form

$$\text{Nu} = y \text{Re}^m \text{Pr}^{1/3}. \quad (4.4.5)$$

To compare the results of current study with that of the literature, the values for Re and Pr and the factors Pr_b/Pr_s in Eq. (4.4.3a) and μ_b/μ_s in Eq. (4.4.4a), however were replaced by the respective airside and waterside experimental data and the comparable correlation from literature were compiled in the same form as of Eq. (4.4.5).

4.5 Airside and Waterside Heat Transfer Rates (q) and Coefficients (h)

A heat balance on the test section control volume was made in the following form

$$q_{\text{overall}} = q_{\text{conduction}} + q_{\text{convection}} + q_{\text{radiation}} + q_{\text{condensation}}. \quad (4.5.1)$$

The waterside and airside heat transfer rates were estimated as,

$$q_w = \dot{m}_w c_{p,w} (T_{w,o} - T_{w,i}) = \dot{m}_w c_{p,w} \Delta T_w \quad (4.5.2a)$$

and

$$q_a = \dot{m}_a c_{p,a} (T_{a,i} - T_{a,o}) = \dot{m}_a c_{p,a} \Delta T_a, \quad (4.5.2b)$$

where the positive q_w and q_a signify air-cooling process and negative q_w and q_a portray air-heating process. The temperature differences, $\Delta T_w = |T_{w,o} - T_{w,i}|$ and $\Delta T_a = |T_{a,i} - T_{a,o}|$, were directly measured using the thermometer's differential function and from several readings the mean was taken for the analysis. The heat transfer rates at waterside were compared with that of the airside. For all the experimental runs, the heat

rate values obtained from Eqs. (4.5.2a) and (4.5.2b) generally agreed within $\pm 6\%$. Thus in the analysis, the overall heat transfer rate, q , was set to the arithmetic average of the airside and waterside heat rates in the following form (Rugh et al., 1992)

$$q = \frac{(q_a + q_w)}{2}. \quad (4.5.3)$$

The radiation heat transfer between the room and the test section wall was neglected due to negligible temperature difference between them. The temperatures of the inner walls ($T_{\text{wall, inner}}$) of the test section were assumed to be equal to the temperature of the flowing air inside the test section ($T_{a,i}$), that is $T_{\text{wall, inner}} \approx T_{a,i}$. Based on Stefan-Boltzmann law, the radiation heat transfer between the inner surfaces of the test section walls and the outer surface of the tubes could be calculated as follows

$$q_{\text{radiation}} = A_{\text{average}} \varepsilon \sigma (T_{a,i}^4 - T_{s,o}^4) = A_{\text{average}} h_{\text{rad}} (T_{a,i} - T_{s,o}), \quad (4.5.4a)$$

where the radiation heat transfer coefficient (h_{rad}) is estimated as,

$$h_{\text{rad}} = \varepsilon \sigma (T_{a,i}^2 + T_{s,o}^2)(T_{a,i} + T_{s,o}). \quad (4.5.4b)$$

For commercial copper tubing with an emissivity of $\varepsilon \approx 0.15$, a conservative estimated of the maximum h_{rad} for cooling and heating processes were found to be 0.95 and 0.80 $\text{W/m}^2 \cdot ^\circ\text{C}$. In both processes, h_{rad} was no more than 1.0% of the respective airside convective heat transfer coefficient (h_a). Thus, the influence of radiation heat transfer between the tube surface and the surrounding environment inside the test section was also ignored (i.e. $q_{\text{radiation}} \approx 0$).

The effect of natural convection on the heat transfer at airside was neglected. The maximum Grashof number, Gr_a , attained in the experiment was approximately 15400 for

cooling and 18300 for heating tests respectively. The Gr_a to Re_a^2 ratios (buoyancy effect indicator) were about 0.000143 (i.e. $\ll 1$) for cooling and 0.000154 (i.e. $\ll 1$) for heating, which according to authors such as Lloyd and Sparrow (1970), Incropera and DeWitt (2002), and Cengel (2003) justify the omission of natural convection for both cooling and heating processes. Similarly, the effect of natural convection on the heat transfer at waterside could also be neglected. The relative humidity (RH) during all tests was measured to be at $27 \pm 5\%$ during cooling and $75 \pm 5\%$ during heating tests. Due to the choice of the operating temperature range of air and water inlets, the dew point temperature ($T_{d,a}$) of air was found to be always lower than the outer surface temperature ($T_{s,o}$) of the tubes. As a result no condensation on the tube surface was observed during the tests (i.e. $q_{\text{condensation}} \approx 0$). Thus, based on the assumptions listed in Section 4.2, the heat transfer between the air and the water was mainly due to the forced convection mechanism. Therefore, by setting the overall heat transfer rate, q_{overall} , to the average heat transfer rates at waterside and airside, Eq. (4.5.1) can be rewritten as

$$q = q_{\text{overall}} \approx q_{\text{convection}} \quad (4.5.5)$$

The airside and waterside convection heat transfer rates for Eq. (4.5.5) were calculated using Newton's law of cooling, which is described below.

Airside Convection Heat Transfer rate ($q_{\text{convection, a}}$):

For airside convection heat transfer rate, Eq. (4.5.5) was rewritten as

$$q = h_a A_{s,o} (T_{a,i} - T_{s,o}) = h_a A_{s,o} \Delta T_{a-s}, \quad (4.5.6)$$

where again the positive q indicates the air-cooling process and the negative q signifies the air-heating process. From Eq. (4.5.6), the airside heat transfer coefficient, h_a , was estimated as,

$$h_a = \frac{q}{A_{s,o} \Delta T_{a-s}}. \quad (4.5.7)$$

Finally the airside Nusselt number, Nu_a , was estimated using Eq. (4.4.1) as

$$Nu_a = \frac{h_a Z_a}{k_a} = \frac{h_a (2a_o)}{k_a}. \quad (4.5.8)$$

Waterside Convection Heat Transfer rate ($q_{\text{convection, w}}$):

For deducing the waterside convection heat transfer rate, the tube inner side surface temperature needs to be calculated first. The average inner-surface temperature of the tubes was deduced as follows

$$T_{s,i} = T_{s,o} + q \left[\frac{\ln \left(\frac{D_{h,o}}{D_{h,i}} \right)}{2\pi k_{\text{tube}} L_t} \right]. \quad (4.5.9)$$

Equation (4.5.9) is based on the radial conduction through circular cross-section. As proposed by many authors and as used in many heat transfer textbooks, this equation was employed in current study for the non-circular cross-section (i.e. elliptical tube in current study) by replacing the tube's inner and outer side diameters with the respective hydraulic diameters. For all the experimental runs, the difference of temperatures between the outer ($T_{s,o}$) and inner ($T_{s,i}$) sides of the tube was observed to be no more than 0.03°C , since the tubes are made of copper with very thin wall (i.e. only 0.825 mm thick). Therefore, for the ease of analysis, the inner and outer surface temperatures of the tube could be assumed to be the same. Thus the inner surface temperature was set to the outer surface temperature as

$$T_{s,i} \approx T_{s,o}. \quad (4.5.10)$$

For the waterside convection heat transfer rate, Eq. (4.5.5) was rewritten as

$$q = h_w A_{s,i} (T_{w,b} - T_{s,i}) = h_w A_{s,i} \Delta T_{w-s}, \quad (4.5.11)$$

where again the positive q indicates the air-cooling process and the negative q signifies the air-heating process. From Eq. (4.5.11), the waterside heat transfer coefficient, h_w , was estimated as,

$$h_w = \frac{q}{A_{s,i} \Delta T_{w-s}}. \quad (4.5.12)$$

The waterside Nusselt number, Nu_w , was estimated using Eq. (4.4.1) as

$$Nu_w = \frac{h_w D_{h,i}}{k_w}. \quad (4.5.13)$$

Thermal Resistance (R_{th}):

Based on the assumption in Eq. (4.5.10), total thermal resistance (R_{th}) for the heat transfer between the water and air sides was estimated as follows

$$\begin{aligned} R_{th} &= \frac{T_{w,b} - T_{a,i}}{q} = R_{th,w} + R_{th,tube} + R_{th,a} \\ &= \frac{1}{h_w A_{s,i}} + \frac{\ln(D_{h,o}/D_{h,i})}{2 \pi k L} + \frac{1}{h_a A_{s,o}} \approx \frac{1}{h_w A_{s,i}} + \frac{1}{h_a A_{s,o}}. \end{aligned} \quad (4.5.14)$$

The airside thermal resistance is given by

$$R_{th,a} = \frac{1}{h_a A_{s,o}}, \text{ and} \quad (4.5.15a)$$

the waterside thermal resistance is given by

$$R_{th,w} = \frac{1}{h_w A_{s,i}} \quad (4.5.15b)$$

CHAPTER 5

RESULTS AND DISCUSSIONS

5. RESULTS AND DISCUSSIONS

The principal focus of current study was to obtain the airside side Nusselt number (Nu_a) and Reynolds number (Re_a) relationship. The experiments on air-cooling and heating processes were conducted in four phases depending on the operating conditions as specified in Table 3.3.1.

Two types of temperature loading were executed. The air and water inlet temperatures were maintained constant in the first type for the experimental Phase-I and Phase-II, and the difference between the air and water inlet temperatures were kept constant in the second type for the experimental Phase-III and Phase-IV. In Phase-I (air cooling process), hot airflow across the tube array was maintained at $T_{a,i} = 41.5 \pm 1.5^\circ\text{C}$ (for $10000 \leq Re_a \leq 33200$) and cold water entering inside the tubes was kept at $T_{w,i} = 6.5 \pm 1.0^\circ\text{C}$ (for $1100 \leq Re_w \leq 3500$). Phase-II was an air heating process, where cold airflow was kept at $T_{a,i} = 17.5 \pm 1.5^\circ\text{C}$ (for $10600 \leq Re_a \leq 33500$) and hot inlet water entering the tubes was maintained at $T_{w,i} = 38.8 \pm 0.8^\circ\text{C}$ (for $1500 \leq Re_a \leq 7300$). For Phase-III (air cooling process) and Phase-IV (air heating process), the temperature differences between the mean approach air and the inlet water was maintained at $(\Delta T_{a,w} = |T_{a,i} - T_{w,i}| = 15.7 \pm 1.5^\circ\text{C})$. For Phase-III (air cooling process), the air inlet temperature changed between 27.5 and 37°C in the range $10300 \leq Re_a \leq 33500$ and the water inlet temperature varied from 13 to 21°C in the range $3300 \leq Re_w \leq 6100$. During Phase-IV (air heating process), the air inlet temperature varied between 6.5 and 10°C in the range $10800 \leq Re_a \leq 36000$ and the water inlet temperature changed from 23.5 to 25°C in the range $4000 \leq Re_w \leq 7100$. The experimental results, e.g. the effect of Reynolds number on the heat transfer rate, and the Nusselt number for both air-cooling

and heating processes are discussed in the following sections. It is worth mentioning that some of the results and observations from each experimental phase are disseminated and documented in the form of journal publication, conference presentations and transaction publications as Khan et al. 2004a (Phase-I), Khan et al. 2004b (Phase-II), and Khan et al. 2005 (Phase-III and Phase-IV).

5.1 Airside Analysis – both Air-cooling ($T_{a,i} > T_s > T_{w,i}$) and Air-heating ($T_{a,i} < T_s < T_{w,i}$) processes

From all the experimental phases, the effects of Re_a on the heat transfer rate (q) and Nusselt number (Nu_a) were analyzed. In addition, the variation of airflow pressure drop across the tube array (C_{press}) with respect to Re_a was also observed. All of which are discussed in the following subsections.

5.1.1 Effect of Reynolds number on the Heat Transfer rate (q - Re_a relationship)

The heat transfer rate (q) was calculated using Eq. (4.5.3), while the airside Reynolds number (Re_a) and waterside Reynolds number (Re_w) were deduced from Eq. (4.3.1). From the analysis, the uncertainty in q was found to be in the range 3 – 12% for all the tests, depending on the temperature loadings and the air and water flow rates.

To observe the effects of airside Reynolds number on the heat transfer rate, the q as a function of Re_a was plotted in Figures 5.1.1 to 5.1.4 for both cooling and heating tests. A number of curve fits were executed to optimize the manner of q - Re_a relationship. Although the variation of q with Re_a apparently looks linear, the power law curve fit covered data very well with high R^2 values in the following form

$$q = C_1 Re_a^{C_2}, \text{ for } 10000 < Re_a < 36000. \quad (5.1.1)$$

The curve fit coefficients, C_1 and C_2 , and the coefficients of determination (R^2 values) for each curve fit are listed in Table 5.1.1.

Table 5.1.1 Curve fit Coefficients and R^2 Values for Eq. (5.1.1) and Figures 5.1.1 to 5.1.4 ($q - Re_a$ variation)

Experimental phases and test conditions	Re_w	C_1 (Watt)	C_2	R^2
PHASE-I: Air Cooling ($T_{a,i}$ and $T_{w,i}$ maintained constant)	1100	27.94	0.365	0.93
	1800	10.43	0.478	0.98
	2600	6.64	0.530	0.99
	3500	4.65	0.570	0.96
PHASE-II: Air Heating ($T_{a,i}$ and $T_{w,i}$ maintained constant)	1500	62.46	0.240	1.00
	3400	13.67	0.410	0.99
	5300	5.91	0.490	0.99
	7300	9.38	0.440	1.00
PHASE-III: Air Cooling (ΔT_{a-w} maintained constant)	3300	9.18	0.413	0.99
	6100	6.48	0.457	0.99
PHASE-IV: Air Heating (ΔT_{a-w} maintained constant)	4000	9.78	0.410	0.99
	7100	4.92	0.484	0.96

In general, it is seen from Figures 5.1.1 to 5.1.4 that, for a given Re_w , the q/Re_w ratio increases and the q/Re_a ratio decreases with the increase of Re_a , which is qualitatively and quantitatively similar for all the tests. Except for some scatters in the data mostly in the range $27000 \leq Re_a \leq 34000$ that are attributable to the experimental errors, the change in q per unit change in Re_a (dq/dRe_a ratio) generally decreases with increasing Re_a . This diminishing effect could be best represented by the obtained $q - Re_a$ power law relationship as given in Eq. (5.1.1). As observed in the analysis, the airside thermal resistance ($R_{th,a}$) was relatively higher at lower Re_a for all the cases, which

decreased with increasing Re_a . In the analysis for all the experiments, the $R_{th,a}$ was found to vary between 95% (at $Re_a \approx 10000$ and $Re_w \approx 7300$) and 83% (at $Re_a \approx 33000$ and $Re_w \approx 1100$) of the total thermal resistance, R_{th} . The diminishing character of q/Re_a with increasing Re_a can be explained that the increasing airflow in the range $10000 \leq Re_a \leq 20000$ somewhat stirs up the fluid layer on the tube surface, which resists the boundary layer formation and thus increases the value of q . With further increase in Re_a , the boundary layer does not alter significantly and this situation slows down the increase in q with further increase in Re_a .

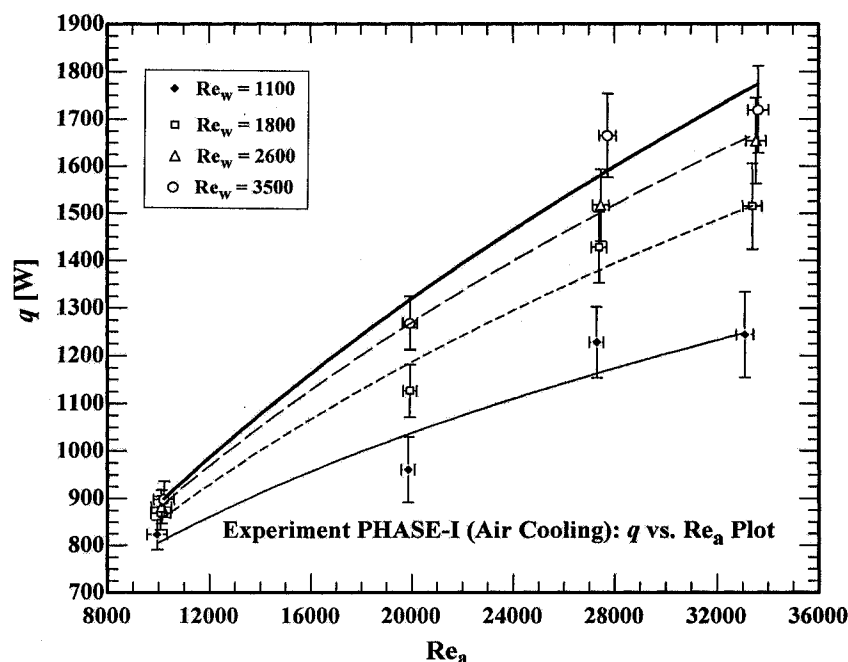


Figure 5.1.1 Change of q with Re_a for different Re_w (Phase-I: Air-cooling Test)

(Note: $q = 1269$ W at $Re_w = 2600$ and $q = 1268$ W at $Re_w = 3500$ overlap each other)

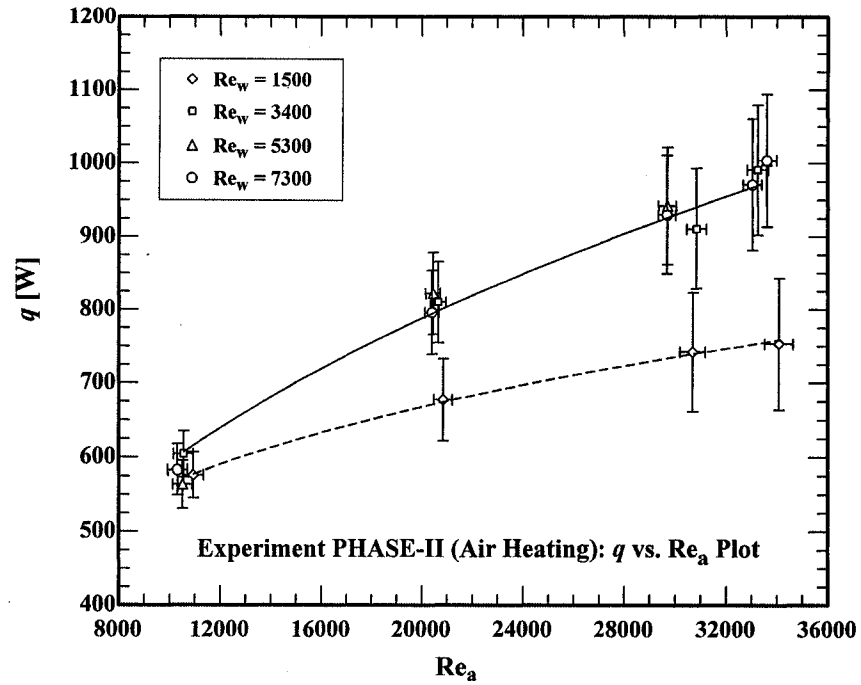


Figure 5.1.2 Change of q with Re_a for different Re_w (Phase-II: Air-heating Test)

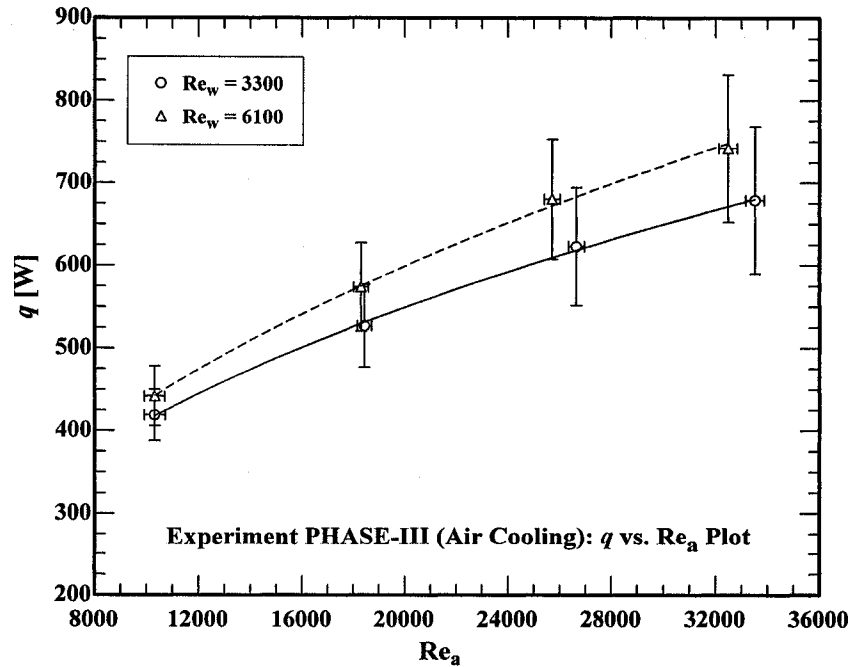


Figure 5.1.3 Change of q with Re_a for different Re_w (Phase-III: Air-cooling Test)

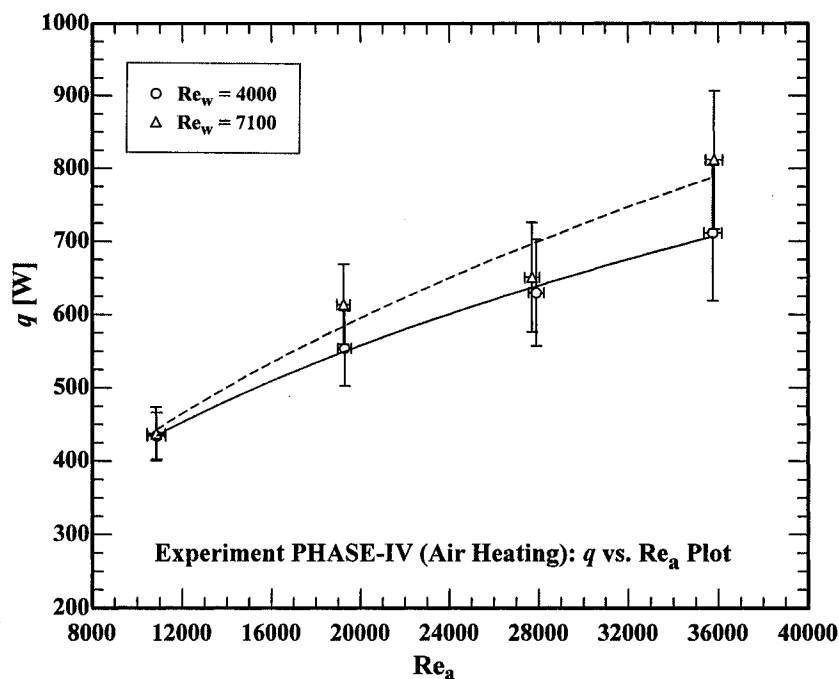


Figure 5.1.4 Change of q with Re_a for different Re_w (Phase-IV: Air-heating Test)

The increase in q per unit increase in Re_w , dq/dRe_w , also increases with increasing Re_a for both cooling and heating tests. As can be seen in Figures 5.1.1 to 5.1.4, the dq/dRe_w increases comparatively rapidly at lower Re_a in the range $10000 \leq Re_a \leq 20000$ beyond which the change of dq/dRe_w is relatively slower up to $Re_a = 36000$. This is because of the total R_{th} , which is relatively large at small Re_a and thus, any decrease in R_{th} , may it be from the waterside or the airside, can lead to significant increase in q . At higher Re_a , the total R_{th} is relatively smaller and hence, decreasing $R_{th,w}$ via increasing Re_w lead to a smaller percentage increase in q . Figure 5.1.2 shows an important phenomenon for the variation of q with Re_w especially in the higher range of Re_w , where the data points for $q-Re_a$ curves at different Re_w are much closer. That means the increase in q with increasing Re_w is not prominent at higher Re_w . For a given Re_a , as observed in

other experiments, the increase in q with increasing Re_w is significant in the lower range of Re_w from 1500 to 3400, but in the higher range of Re_w from 3400 to 7300 the increase in q with Re_w is less significant. The q/Re_w ratio for a given Re_a usually decreases with the increase of Re_w , indicating that at greater Re_w the effect of Re_w on q significantly slows down due to the restrictions of the thermal resistance (R_{th}). In the analysis, it was observed that for a given R_{th} , the $R_{th,w}$ was somewhat higher in the range $1500 \leq Re_w \leq 3400$ compared to the range $3400 \leq Re_w \leq 7300$. As Re_w increases, flow changes from laminar to turbulent regime in the range $1500 \leq Re_w \leq 3400$, the laminar boundary layer breaks and the $R_{th,w}$ decreases. In this circumstance the q increased significantly with increasing Re_w only in the lower range $1500 \leq Re_w \leq 3400$. Although the flow becomes more turbulent with further increase in Re_w , the boundary layer agitation at waterside approaches its saturation state, which causes the increase in q with Re_w to slow down. This is true, because, the $R_{th,w}$ in the range $3400 \leq Re_w \leq 7300$ was found not only smaller but also similar in magnitudes and in this event any further increase in q through increasing Re_w was restricted by the higher $R_{th,a}$. This is the reason for the Figure 5.1.2 to show the $q-Re_a$ curves much closer for $Re_w > 3400$.

Overall the q invariably increased with increasing Re_a in the power law manner for all the cases. However, for the case of Re_w , q increased with increasing Re_w significantly in the lower range of Re_w and slowed down in the higher range of Re_w . No noticeable difference in the variation of q with Re_a was distinguished between the air cooling and heating processes. The apparent differences are well within the estimated uncertainty as shown in the respective figure with associated error bars.

5.1.2 Effect of Reynolds number on Nusselt number (Nu_a - Re_a relationship)

The airside Nusselt number (Nu_a) was deduced using Eq. (4.5.8). The average Nu_a values respect to Re_a corresponding to different Re_w are given in Table B.1 and B.2 in Appendix B. The estimated uncertainty for Nu_a varied from 4 to 13% in all the experiment phases.

To observe the dependency of Nu_a on Re_a , Nu_a as a function of Re_a is plotted in Figures 5.1.5 to 5.1.8 for both cooling and heating tests. As expected, Nu_a invariably increased mainly with the increase of Re_a for all the experiments both for cooling and heating tests. Based on physics, one may expect to see progressively smaller Nu_a/Re_a and hence $\frac{dNu_a}{dRe_a}$ at higher Re_a , beyond the tested range. Various curve fits were applied to optimize the Nu_a - Re_a relationship. In spite of the qualitatively linear appearance of the Nu_a - Re_a relation, the power law relationship fits data very well with high R^2 values. The Nu_a - Re_a relationship was obtained in the following form

$$Nu_a = C_3 Re_a^{C_4} \text{ in the range } 10000 < Re_a < 36000, \quad (5.1.2)$$

where C_3 and C_4 are the curve fit coefficients, which in addition to the respective coefficients of determination (R^2 values), are tabulated in Table 5.1.2.

In general, for a given Re_w , for all the experiments, the values of Nu_a increased with the increase of Re_a , which can be clearly seen in Figures 5.1.5 through 5.1.8. On the other hand, for a given Re_a , the values of Nu_a for all the water mass flow rates, and hence for all the Re_w , were roughly the same as seen from Tables B.1 and B.2 in Appendix B. While the q - Re_a relationship is influenced by the change of Re_w , especially in the lower

range of Re_w , the corresponding Nu_a - Re_a relationship is not expected to be so, as long as the airside thermal resistance is much larger than the waterside, i.e. $R_{th,a} \gg R_{th,w}$, which is the case here. In the experiments, depending on the nature of the total R_{th} guided by the heat transfer mechanism, the $R_{th,a}$ was found to vary between 0.0125 and 0.0374°C/W, which was higher than $R_{th,w}$ by 250 to 1750%. Thus, Nu_a - Re_a relationship is approximately independent of Re_w , over the ranges of conditions considered.

Table 5.1.2 Curve fit Coefficients and R^2 Values for Eq. (5.1.2) and Figures 5.1.5 to 5.1.8 (Nu_a - Re_a variation)

Experimental phases and test conditions	Re_w	C_3	C_4	R^2
PHASE-I: Air Cooling ($T_{a,i}$ and $T_{w,i}$ maintained constant)	1100	0.420	0.607	0.99
	1800	0.290	0.638	0.99
	2600	0.228	0.661	0.99
	3500	0.154	0.702	0.97
PHASE-II: Air Heating ($T_{a,i}$ and $T_{w,i}$ maintained constant)	1500	0.426	0.609	0.99
	3400	0.218	0.674	1.00
	5300	0.134	0.719	0.99
PHASE-III: Air Cooling (ΔT_{a-w} maintained constant)	7300	0.305	0.638	0.99
	3300	0.338	0.632	0.99
PHASE-IV: Air Heating (ΔT_{a-w} maintained constant)	6100	0.311	0.630	0.99
	4000	0.296	0.633	0.99
PHASE-IV: Air Heating (ΔT_{a-w} maintained constant)	7100	0.200	0.673	0.96

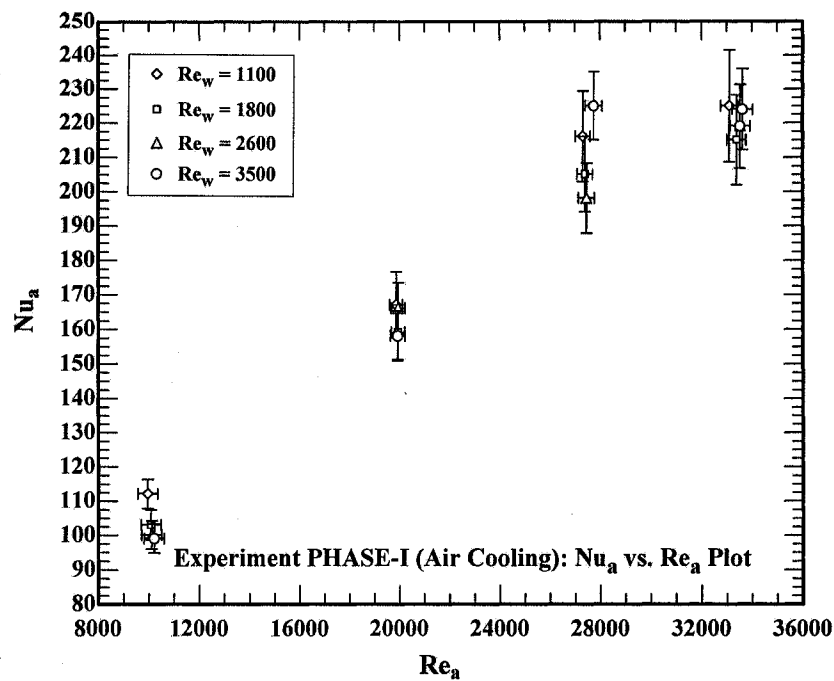


Figure 5.1.5 Change of Nu_a with Re_a for different Re_w (Phase-I: Air-cooling Test)

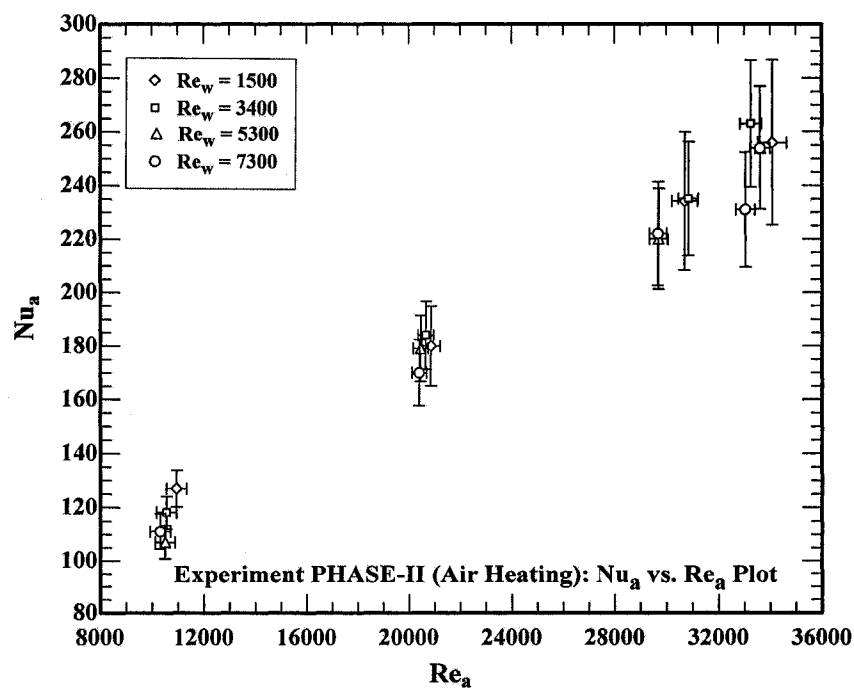


Figure 5.1.6 Change of Nu_a with Re_a for different Re_w (Phase-II: Air-heating Test)

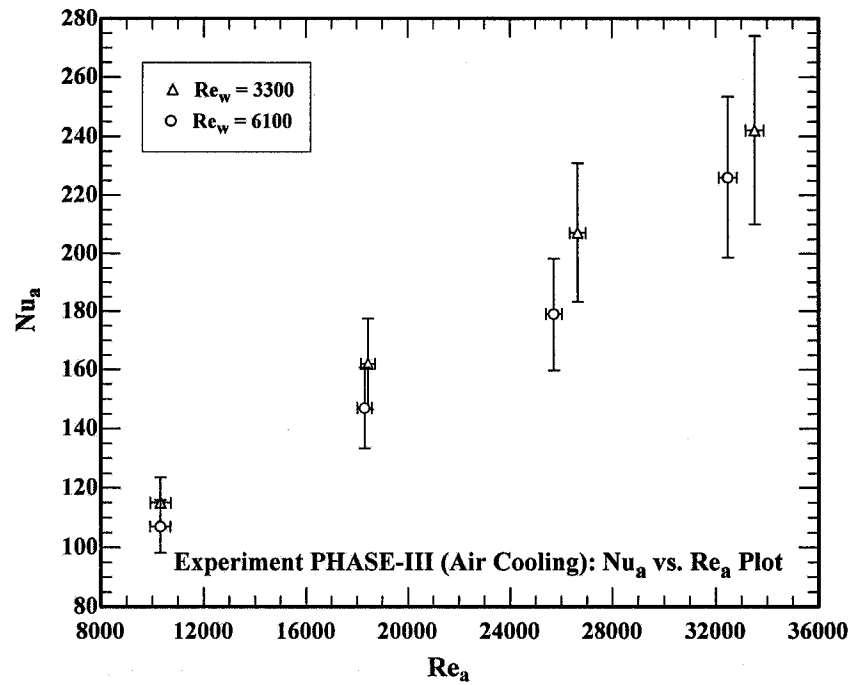


Figure 5.1.7 Change of Nu_a with Re_a for different Re_w (Phase-III: Air-cooling Test)

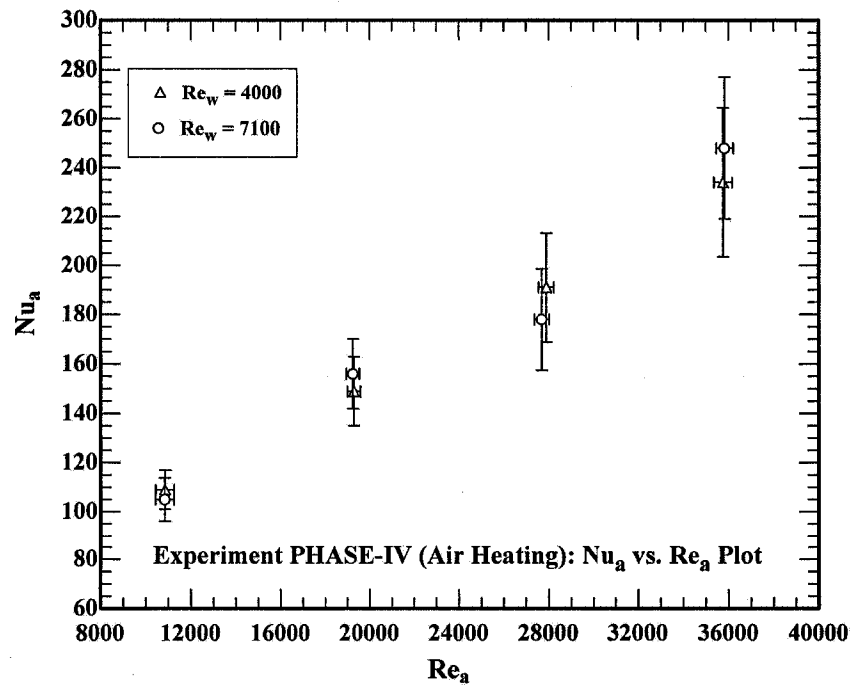


Figure 5.1.8 Change of Nu_a with Re_a for different Re_w (Phase-IV: Air-heating Test)

In Figures 5.1.5 and 5.1.6, the variations of Nu_a with Re_a are plotted corresponding to four different Re_w in the range $1100 \leq Re_w \leq 3500$ and $1500 \leq Re_w \leq 7300$ respectively. In Figures 5.1.7 and 5.1.8, the changes of Nu_a with Re_a are plotted for two different Re_w in the range $3300 \leq Re_w \leq 6100$ and $4000 \leq Re_w \leq 7100$ respectively. All the figures covered the observable variations of Nu_a with Re_a for the entire investigated range of Re_w , i.e. $1100 \leq Re_w \leq 7300$. As discussed below, the nature of the variations of Nu_a with Re_a was found to be the same for all the ranges of Re_a in all figures.

It is observable in all figures that, for a given Re_w , the ratio Nu_a/Re_w increases with the increase of Re_a , which shows that only Re_a dominates the increase in Nu_a with increasing Re_a . At lower Re_a , the q/Re_a ratio is larger and hence the Nu_a is relatively smaller, whereas, at higher Re_a the q/Re_a ratio is smaller that gives a comparatively larger Nu_a . Although the $q-Re_a$ relationship is somewhat influenced by the change of Re_w especially in the lower range of Re_w (around somewhat smaller values of $R_{th,a}$), Nu_a-Re_a relationship is not affected by the Re_w , rather it is dictated by the heat transfer mechanism between the air and the outer surface of the tube. This is expected because the $R_{th,a}$ is much higher than the $R_{th,w}$ as a result Re_w cannot influence the Nu_a-Re_a relationship.

As seen in Figures 5.1.5 through 5.1.8 and Table B.2, very small effect of Re_w on Nu_a is observed throughout the investigated range of Re . For a given Re_a the Nu_a values are in similar magnitudes for all the water flow rates in the range $1100 \leq Re_w \leq 7300$. The only exceptions are noticed at $Re_w = 1100$ in Figure 5.1.5 and $Re_w = 3300$ in Figure 5.1.7 for air-cooling tests, where the Nu_a values are a little higher, although they are well within the estimated uncertainty. In these two ranges of Re_w , the R_{th} were found to be

somewhat less and the $R_{th,w}$ a little higher compared to other ranges, which brought a slightly lower $R_{th,a}$ and thus an increased Nu_a . This is because, as the $R_{th,a}$ is always much higher than the $R_{th,w}$, increased $R_{th,w}$ decreases the $R_{th,a}$ for a given R_{th} , which promotes Nu_a . Thus, in these two situations the Nu_a – Re_a relation might have been slightly influenced by the Re_w . The only scatters in data are found at $Re_a \approx 27500$ in Figure 5.1.5, at $Re_a \approx 33000$ in Figure 5.1.6, at $Re_a \approx 25700$ in Figure 5.1.7, and at $Re_a \approx 27700$ in Figure 5.1.8. These scatters are within the expected experimental uncertainty as shown in respective figures by the respective error bars. For all the phases of experiments considered, however, a little higher Nu_a was observed in heating tests than in cooling; on average approximately by up to 7% depending on the Re_a investigated. This may have been attributed to the nature of the development of boundary layers and relatively wider wake in the air-heating test. In air heating, the warm tube surface may have pushed away the cold air molecule flowing over it. This situation caused an unstable boundary layer during air heating and thus the Nu_a somewhat increased compared to air-cooling. However, whether this variation in Nu_a between air-cooling and air-heating tests is due to the Prandtl effect is investigated next in subsection 5.1.3 below.

5.1.3 Effect of Reynolds number on Nusselt number with Prandtl effect (Nu_a – Re_a – Pr_a relationship)

For the determination of Nu_a – Re_a relationship in Eq. (5.1.2) and plotting them in Figures 5.1.5 to 5.1.8, the Prandtl effect was not included because of the constant nature of airside Prandtl number ($Pr_a \approx 0.72$), which suggests that the Nu_a predominantly is a function of Re_a in this case. However, as the airside film temperature, $T_{f,a}$, ranged

between 13 and 34°C during the tests, the evaluation of Prandtl number also slightly varied in the range between 0.733 and 0.727. Whatever little it may be, this variation may have some contribution on the airside boundary layer formation, and hence on the heat transfer. As portrayed in Figure 5.1.9, with the negligible influence of Re_w and with the inclusion of Prandtl effects (Pr_a), the overall Nu_a – Re_a correlations separately for cooling and heating of air were obtained in the form of Eq. (4.4.3b) in Section 4.4 as,

$$Nu_a = 0.248 Re_a^{0.668} Pr_a^{1/3}, \text{ for } 9900 \leq Re_a \leq 33600 \text{ (Cooling the Air)}, \quad (5.1.3)$$

and

$$Nu_a = 0.282 Re_a^{0.658} Pr_a^{1/3}, \text{ for } 10300 \leq Re_a \leq 34100 \text{ (Heating the Air)}. \quad (5.1.4)$$

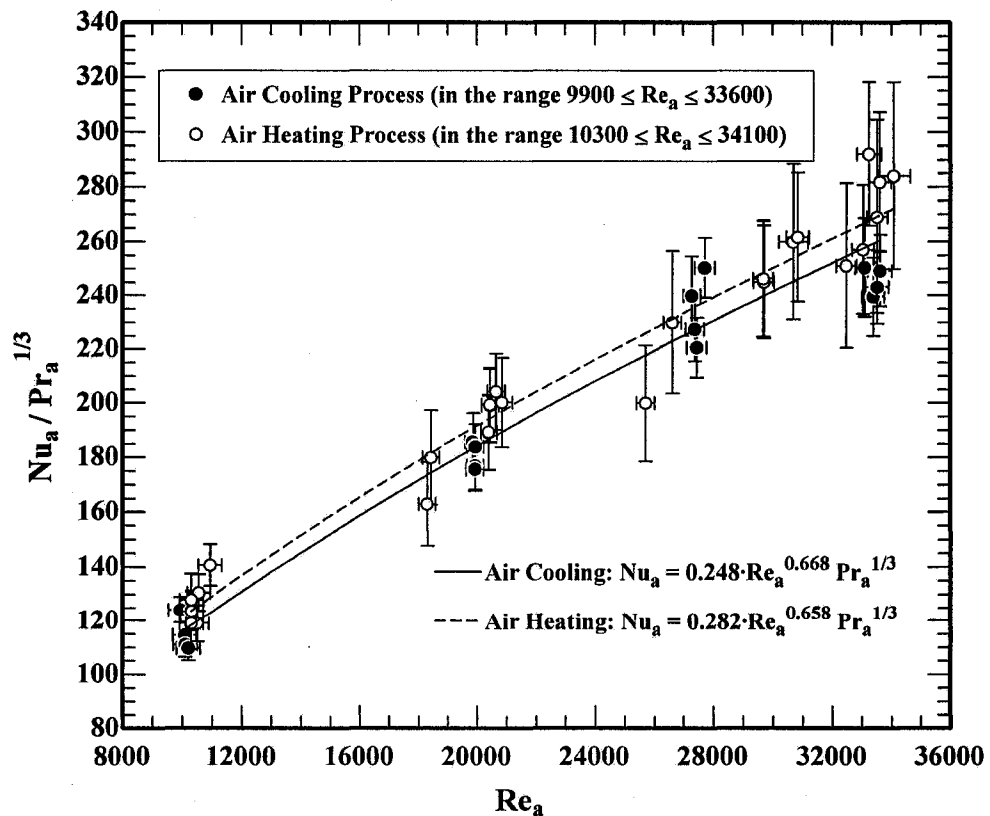


Figure 5.1.9 Nu_a – Re_a – Pr_a relationships for cooling and heating (Error bars shown)

It is observed that the inclusion of Prandtl effect somewhat minimized the Nu_a - Re_a relational differences between the cooling and heating tests but did not diminish. This scenario indicates that the slightly higher heat transfer in heating than in cooling test is not only due to the Prandtl effect, additionally it may be due to the $T_{f,a}$ effect (other than that via Pr_a) in the boundary layer and wake. In air heating test, early flow separation may have been occurred that made somewhat wider wake compared to cooling test and this wider wake enhanced heat transfer. The $T_{f,a}$ effect in the boundary layer may also include the non-linear variation of temperature between the tube surface ($T_{s,o}$) and the approach air ($T_{a,i}$) as contrast to the linear assumption made for the estimation of $T_{f,a}$. Within the set experimental limitations, however, any difference in heat transfer between the cooling and heating tests cannot be confidently concluded from this observation, because the results are well within the estimated experimental uncertainties (i.e. 4 to 13% for both cooling and heating tests) as seen from the respective error bars in Figure 5.1.9. Thus, from all the data sets, in the presence of Pr_a , an overall correlation between Nu_a and Re_a , which is applicable for both cooling and heating the air, could be proposed in the following form,

$$Nu_a = 0.263 Re_a^{0.663} Pr_a^{1/3}, \text{ for } 9900 \leq Re_a \leq 34100. \quad (5.1.5)$$

This overall correlation is compared with other available similar studies as described in subsection 5.1.4 and as shown in Figure 5.1.10.

5.1.4 Comparison of Current Proposed Nu_a - Re_a - Pr_a Correlation with other Available Studies

Experimentally obtained current correlations are compared with other available studies as shown in Figure 5.1.10. Most widely referred one of such generalized correlations is that proposed by Žukauskas (1972) and Žukauskas and Žiugžda (1985), as referenced in Sadik et al. (1987), is

$$Nu_a = 0.27 Re_a^{0.60} Pr_a^{0.37} \left(\frac{Pr_{a,b}}{Pr_{a,s}} \right)^{0.20}, \text{ for } 1000 \leq Re_a \leq 200000, \quad (5.1.6a)$$

where the Prandtl number, $Pr_{a,b}$, is evaluated at airside bulk temperature as defined by Eq. (4.1.3) and the $Pr_{a,s}$ is evaluated at the tube outer surface temperature ($T_{s,o}$). Equation (5.1.6a) represents the average Nu_a for forced convection heat transfer from an elliptical cylinder at cross flow of air under both constant surface temperature and uniform heat flux conditions. The calculation of Re_a for Eq. (5.1.6a) was based on the streamwise outer major axis length of the cylinder. By employing the current experimental parameters and conditions, Žukauskas' correlation in Eq. (5.1.6a) could be reduced to

$$Nu_a = 0.28 Re_a^{0.594} Pr_a^{1/3}, \text{ for } 10000 \leq Re_a \leq 35000. \quad (5.1.6b)$$

For a given Re_a , this correlation predicts a relatively lower Nu_a (on average by 45%) compared to that of the current study. This is expected because the correlation in Eq. (5.1.6a) was established for a single elliptic cylinder with a higher axis ratio ($AR = 0.50$), whereas a single array of elliptical tubes with a lower axis ratio ($AR = 0.30$)

was examined in the current study. However, the result from Žukauskas correlation has very good qualitative agreement with that of the present study.

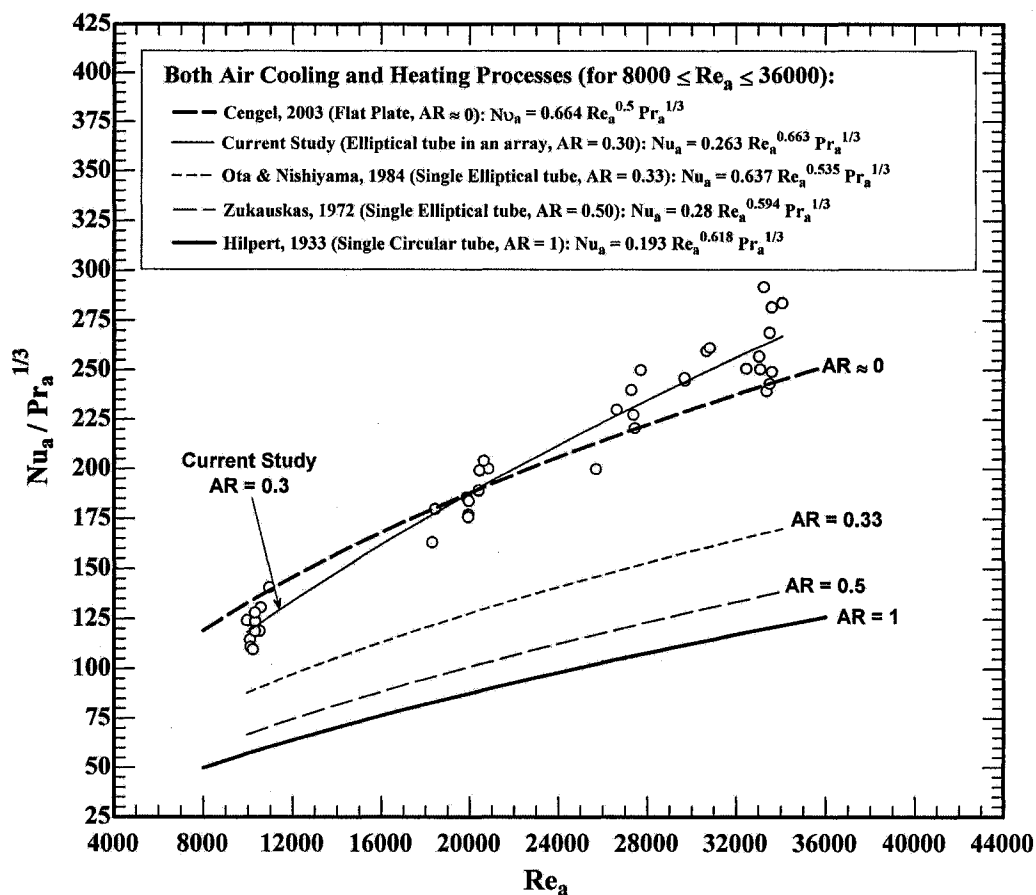


Figure 5.1.10 Comparison of current Nu_a - Re_a - Pr_a relationship with other correlations

Another correlation that was proposed by Ota and Nishiyama (1984) for a single elliptical cylinder of $AR = 0.33$ at zero angle of attack under the condition of uniform heat flux (electrically heated) in the following form,

$$Nu_a = 0.55 Re_a^{0.54}, \text{ for } 8000 \leq Re_a \leq 79000, \quad (5.1.7a)$$

where Re_a was based on the streamwise major axis length of the tube. Like before, by employing the current experimental parameters and conditions, this correlation could be reduced to

$$\text{Nu}_a = 0.61 \text{Re}_a^{0.535} \text{Pr}_a^{1/3}, \text{ for } 10000 \leq \text{Re}_a \leq 35000. \quad (5.1.7b)$$

Although Ota and Nishiyama (1984) used a higher Re_a range compared to current study, the correlation was compared in the range of Re_a as investigated in current study. For a given Re_a , this correlation also predicts a relatively lower Nu_a (roughly by 31%) compared to current study. Their correlation, however, leads to the Nu_a - Re_a results, which are in very good agreement with that of the current results as can be seen in Figure 5.1.10. It is to be noted here that the correlation in Eq. (5.1.7) was obtained for a single elliptic cylinder compared to current study where a single array of elliptical tubes with $\text{AR} = 0.30$ was examined.

It is also interesting to see how the current results compare with that of the heat transfer correlations for flat plate ($\text{AR} = 0$) and for circular tubes ($\text{AR} = 1$). In this view, in addition to the above correlations (Ota and Nishiyama 1984 and Žukauskas 1972), the correlations for circular tubes and flat plate are also plotted in Figure 5.1.10. To compare the current result with circular and flat plate situations, the elliptical tube dimension from current study was theoretically transformed into representative circular tube (i.e. same the perimeter) giving an AR of 1 and into equivalent flat plate tube (i.e. the half the perimeter of the elliptic tube) giving an AR of approximately zero. For the single circular tube at constant surface temperature, the correlation (proposed by Hilpert 1933 as mentioned in Incropera and DeWitt 2002) $\text{Nu}_a = 0.193 \text{Re}_a^{0.618} \text{Pr}_a^{1/3}$ in the range $4000 < \text{Re}_a < 40000$ was compared. For the flat plate tube at constant surface temperature condition, the correlation (Cengel, 2003) $\text{Nu}_a = 0.664 \text{Re}_a^{1/2} \text{Pr}_a^{1/3}$ in the range $0.6 < \text{Pr}_a < 10$ and $\text{Re}_a < 10^5$ was compared. The outer diameter of the transformed circular tube was used as the characteristic length to deduce the Re_a and Nu_a for circular tube case while the half of the perimeter of elliptical tube (i.e. in the direction of airflow) was used as the characteristic length for the transformed flat plate case.

The effect of AR on heat transfer can be clearly seen in Figure 5.1.10. Heat transfer increases with the decrease of AR in the range $1 \geq AR \geq 0$. As seen, the heat transfer for a flat plate or for an elliptic tube is always higher than the circular tube. Also, heat transfer is seen higher for an elliptic AR of 0.33 (Ota and Nishiyama 1984) compared to the AR of 0.50 (Žukauskas 1972) and the current result with an AR of 0.30 is further higher. It is seen that the difference of heat transfer with respect to AR between current study (AR = 0.3) and Ota and Nishiyama (AR = 0.33) is significantly higher compared to the difference of heat transfer between the studies of Ota and Nishiyama (AR = 0.33) and Žukauskas (AR = 0.5). In current study, in addition to smaller AR, an array of tubes was used that might have resulted this higher heat transfer. Although the heat transfer increases with the decrease of AR, there is however a critical AR value beyond which increase in heat transfer is insignificant. In contrast with current elliptical tube array situation, it is observed that the equivalent flat plate provides higher heat transfer only at lower Re_a in the range $8000 \leq Re_a \leq 20000$. At higher Re_a in the range $20000 \leq Re_a \leq 36000$, the elliptic tube array provides higher heat transfer compared to that of the equivalent flat plate.

In short, even though there are some variations in the experimental results from one study to another, the trends of current results satisfactorily converged with those of others. Other than the variation in elliptic AR, part of the quantitative variations from study to study is attributable to the large spectrum of different conditions, which include the tube bundle arrangement, internal-external flow regimes, characteristic lengths used, boundary conditions etc.

5.1.5 Pressure drop across the Tube Array (i.e. $C_{press} - Re_a$ relationship)

The procedures for the measurements of airflow pressure drop across the tube array (Δp_{array}) are described in Section 3.4.2 and the measuring pressure taps are shown in

Figure 3.4.6. The pressure drops, Δp_{array} , were measured for both air-cooling and -heating tests as well as for condition of no heat transfer. The pressure drop across the taps A-A' and B-B' were found to be similar in magnitudes, within $\pm 3\%$, for respective cooling and heating tests. The Δp_{array} values measured across the tap C-C' were 11 to 37% higher than the values measured across the taps A-A' and B-B'. This phenomenon is possibly due to the near wake location of the C-C' pressure taps. As the Δp_{array} values across the pressure tap A-A' and B-B' were similar, the Δp_{array} values measured across the taps B-B' were used in this study.

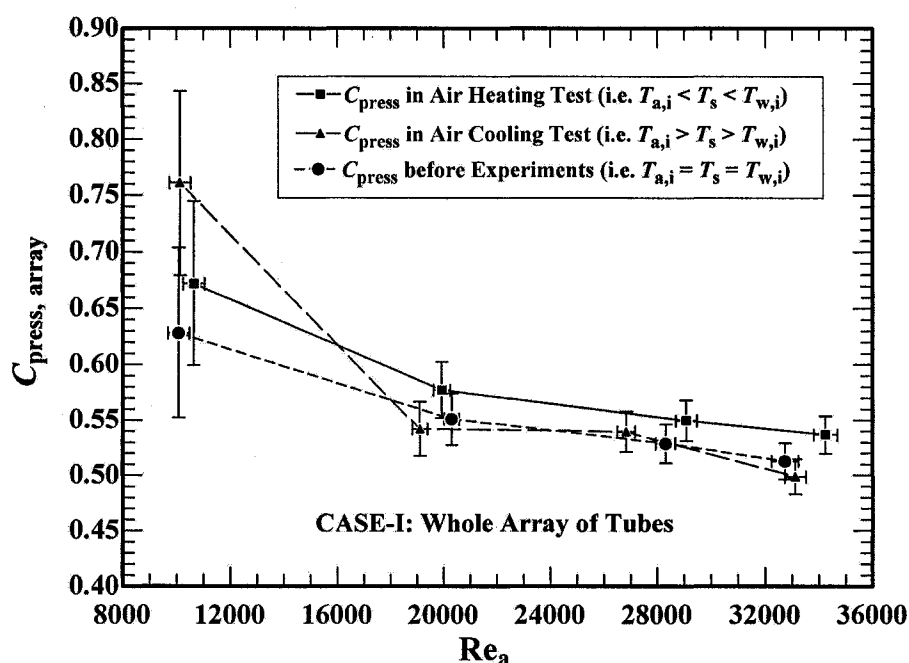


Figure 5.1.11 Case-I: Variation of $C_{press,array}$ with Re_a for the whole array of elliptical tubes (Error bars are shown)

From the measured Δp_{array} values, the dimensionless forms of the pressure drop, i.e. the pressure coefficients (C_{press}), as defined in Section 4.3, were estimated using

Eqs. (4.3.8) and (4.3.7) for the whole array of tubes (Case-I) and for a single tube in the array (Case-II) respectively. The average C_{press} values for each setting of the air velocity are plotted against the Re_a in Figure 5.1.11 for Case-I and in Figure 5.1.12 for Case-II, where the value of the flow obstruction medium for all cases is $N_T = 18$.

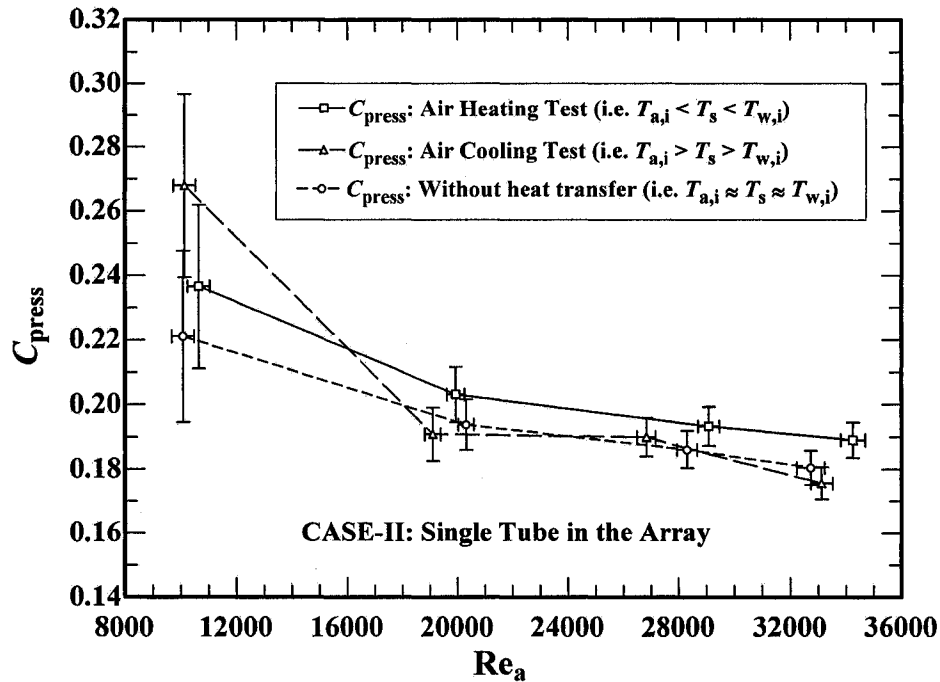


Figure 5.1.12 Case-II: Variation of C_{press} with Re_a for a single elliptical tube in the array (Error bars are shown)

The obtained pressure coefficient values for both cases and at different Re_a are tabulated in Table 5.1.3 with their respective uncertainties. As seen in Figure 5.1.11 (for Case-I), the maximum $C_{\text{press,array}}$ value for the in-line single-array heat exchanger reached to 0.76 at $Re_a \approx 10100$ in cooling tests, 0.67 at $Re_a \approx 10650$ in heating tests, and 0.63 at $Re_a \approx 10100$ without the heat transfer. On the other hand, for Case-II (as seen in Figure 5.1.12), the maximum C_{press} value for a single tube in the in-line single-array heat

exchanger attained 0.27 at $Re_a \approx 10100$ in cooling tests, 0.24 at $Re_a \approx 10650$ in heating tests, and 0.22 at $Re_a \approx 10100$ without the heat transfer. In both Case-I and Case-II, the values of the pressure coefficients sharply decreased in the range $10100 \leq Re_a \leq 19100$ in cooling tests, $10600 \leq Re_a \leq 19900$ in heating tests, and $10100 \leq Re_a \leq 20300$. After these ranges of Re_a , the pressure coefficient remained nearly unchanged (with slight lowering tendency) with further increase in Re_a up to 36000. As the total drag is a combination of friction and pressure drag, at the low Re_a range, the C_{press} was slightly higher and possibly was dictated by the friction drag. With an increase in Re_a , the relative influence of viscous forces decreased while that of the inertial forces increased. As the flow shifted to more turbulent region, the separation point also traveled farther downstream, reducing the size of the wake and the magnitude of the pressure drag. This presumably caused the C_{press} value to decrease with increasing Re_a initially and to remain constant at about 0.54 (for the whole array) and 0.19 (for single tube) beyond $Re_a \approx 20000$, that is, no significant changes in separation point location.

Even though it is within the estimated uncertainty, the C_{press} curve for heating test is found slightly higher than the curves for cooling and without heat transfer tests, as seen in both Figures 5.1.11 and 5.1.12. However, if this were true, it may be due to the variation of fluid properties, which in this case is the airside density (ρ_a). The air density decreases with the increase of temperature. Air heating means to heat up the cold air, which initially possesses a little higher density. Thus the ρ_a , evaluated at air film temperature ($T_{f,a}$), was relatively higher in heating test than in cooling test. In the estimation of C_{press} , the approach air velocity (V_a) in Eq. (3.4.4b) was calculated based on this ρ_a , which may have caused a slightly higher C_{press} in heating than other tests. The

percentage increase of C_{press} for heating tests than cooling and no heat transfer tests, however, were similar for the whole array (Case-I) as well as for the single tube in the array (Case-II).

The individual effect of the air cooling and heating processes on C_{press} could not be ascertained due to the fact that, for a given Re_a the C_{press} values for all the tests fall within the estimated experimental uncertainty. Thus it is concluded that the pressure drop, and hence the C_{press} , is a function of Re_a alone and it is not influenced by the nature of the heat transfer mechanism. To obtain an overall C_{press} versus Re_a relationship for the current experimental configuration, all the available experimental data were unified in Figure 5.1.13 for curve fitting. The inverse power law curve fitted data well (with an average R^2 value of 0.85) than any other curve fittings. The variation could be represented as follows

$$C_{\text{press,array}} = \frac{7.70}{Re_a^{0.263}} \text{ for the whole array (Case-I),} \quad (5.1.8)$$

and

$$C_{\text{press}} = \frac{2.70}{Re_a^{0.263}} \text{ for a single tube in the array (Case-II).} \quad (5.1.9)$$

From the analysis, it is observed that the normalized pressure drop for the whole array is about 2.8 times higher than that of the pressure drop for a single tube in the array. The results are compared with other available studies as shown in Figure 5.1.13 (Case-III).

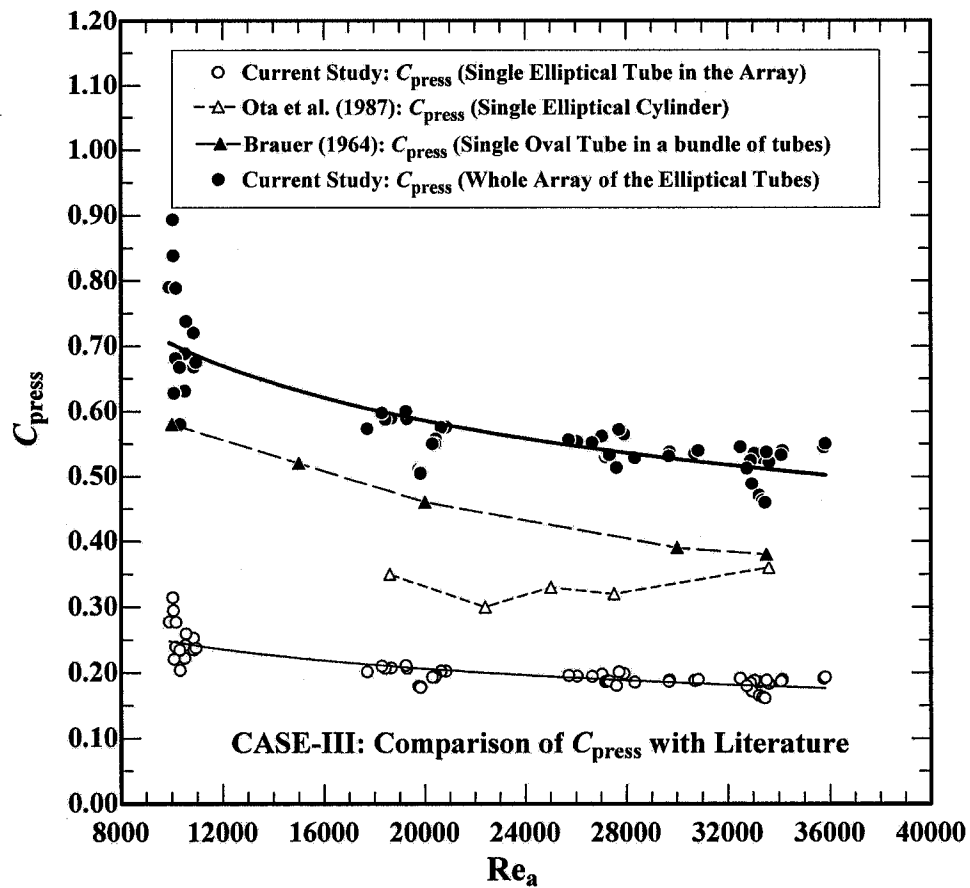


Figure 5.1.13 Case-III: Comparison of current C_{press} – Re_a relation with available studies

The values of C_{press} from other studies, such as the one by Brauer (1964) and another one by Ota et al. (1987), are plotted in Figure 5.1.13 for comparison with current experimental results. The curves obtained in current experiments are in good qualitative agreements with that of Brauer (1964) for a single tube in a bundle of in-line oval finned tubes with an AR of 0.56. The C_{press} values presented by Brauer appear to decrease asymptotically to 0.38 beyond Re_a of 32000. The result is higher than that of the current study for Case-II (single tube in the array), significantly in the lower range of Re_a , which is anticipated since Brauer used finned oval tubes with a higher AR. The pressure drop is mainly driven by the Reynolds number and somewhat by the flatness factor (i.e. the AR

in this case) of the tube. It is well established fact that, for a circular cylinder at cross flow of air, the flow separation occurs somewhere around 80° from the front stagnation point and that for an elliptical tube it is further down at around 95 to 100° depending on the nature of the flow and the axis ratio (AR). Early separation of flows, may it be due to low Re_a or higher axis ratio, makes a wider wake behind the cylinder, which causes a larger pressure drop. The less the size of the wake the less the pressure drop is. The study by Ota et al. (1987) shows that the C_{press} remained approximately at 0.32 in the range $22000 \leq Re_a \leq 33000$ for a single elliptical cylinder having an AR of 0.33 and at zero angle of attack. Compared to current study for Case-I, this value is also higher. This is also rational, because Ota et al. used an elliptical axis ratio (AR = 0.33), which is slightly higher than the one used in the current study (AR = 0.30). The results of both Brauer and Ota et al. for single tube are lower than current study for the Case-II, where the whole array of tubes was presented. This is also expected because the pressure drop for an array or for a bank is always higher than that of a single tube due to the presence of more flow obstruction medium. Other than some data variations at the beginning that are well within the experimental uncertainty, present result, both for cooling and heating processes, satisfactorily agreed with the trends of Brauer and Ota et al. studies.

Table 5.1.3 Values of Airside Pressure Coefficients (C_{press}) at different Re_a

Cases Analyzed	Test conditions	Re_a	C_{press} or	$U_{C_{press}}$ or
			$C_{press,array}$	$U_{C_{press,array}}$ (%)
Case-I (Whole array of tubes)	Air cooling	10129	0.67	10.81
		19104	0.58	4.38
		26816	0.55	3.34
		33124	0.54	3.15
	Air heating	10645	0.76	10.77
		19935	0.54	4.52
		29076	0.54	3.39
		34242	0.50	3.15
	Without heat transfer	10079	0.63	12.08
		20302	0.55	4.24
		28311	0.53	3.33
		32738	0.51	3.19
Case-II (A single tube in the array)	Air cooling	10129	0.27	10.69
		19104	0.19	4.32
		26816	0.19	3.12
		33124	0.18	2.87
	Air heating	10645	0.24	10.73
		19935	0.20	4.19
		29076	0.19	3.08
		34242	0.19	2.88
	Without heat transfer	10079	0.22	12.00
		20302	0.19	4.02
		28311	0.19	3.06
		32738	0.18	2.96

5.2 Waterside Analysis – both Air-cooling ($T_{a,i} > T_s > T_{w,i}$) and Air-heating ($T_{a,i} < T_s < T_{w,i}$) processes

As mentioned before, the main focus of the current study was to deduce the Nu_a – Re_a relationship. However, the Nu_w – Re_w variation is also of interest and hence, is estimated and presented here. The effects of variations of Re_w on the heat transfer rate (q) and waterside Nusselt number (Nu_w) were analyzed. All of which are discussed in the following subsections.

5.2.1 Effect of Reynolds number on the Heat Transfer rate (q – Re_w relationship)

The heat transfer rate (q) was calculated using Eq. (4.5.3), while the waterside Reynolds number (Re_w) and airside Reynolds number (Re_a) were deduced from Eq. (4.3.1). From the analysis, the uncertainty in q was found in the range 3 – 12% for all the tests depending on the temperature loadings and the air and water flow rates. To present the variation of q with Re_w , the q as a function of Re_w are plotted for two representative cases in Figures 5.2.1 and 5.2.2 for both cooling and heating tests. Various curve fits were verified to observe the nature of q – Re_w relationship. It was seen that the data sets fit quite well with the power law curve fit with comparatively high R^2 value in the following form

$$q = C_5 Re_a^{C_6}, \text{ for } 1100 < Re_a < 7300. \quad (5.2.1)$$

For a given Re_a , the curve fit coefficients, C_5 and C_6 , and the coefficients of determination (R^2 values) for each curve fit are listed in Table 5.2.1.

Table 5.2.1 Curve fit Coefficients and R^2 Values for Eq. (5.2.1) and Figures 5.2.1 and 5.2.2 (q - Re_w variation)

Experimental phases and test conditions	Re_a	C_5 (Watt)	C_6	R^2
Phase-I: Air Cooling ($T_{a,i}$ and $T_{w,i}$ maintained constant)	10000	493	0.074	0.97
	19800	148	0.268	0.94
	27300	159	0.292	0.96
	33200	176	0.283	0.99
Phase-II: Air Heating ($T_{a,i}$ and $T_{w,i}$ maintained constant)	10600	514	-0.010	0.02*
	20600	308	0.111	0.70
	30200	253	0.151	0.85
	33500	233	0.168	0.77

* This lower R -squared value is due to non-changing q with respect to Re_w .

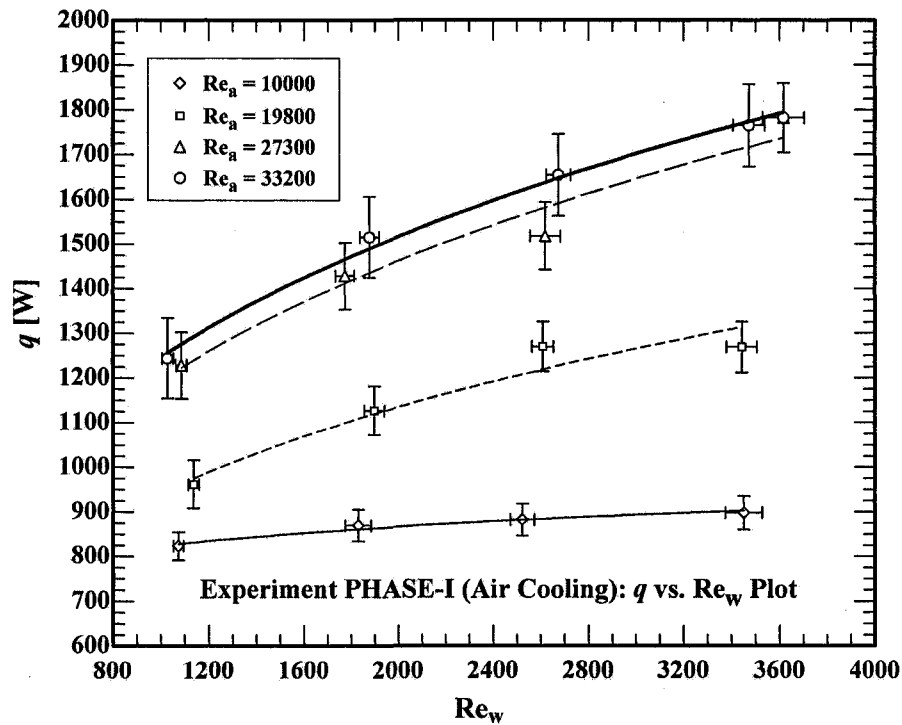


Figure 5.2.1 Change of q with Re_w for different Re_a (Phase-I: Air-cooling Test)

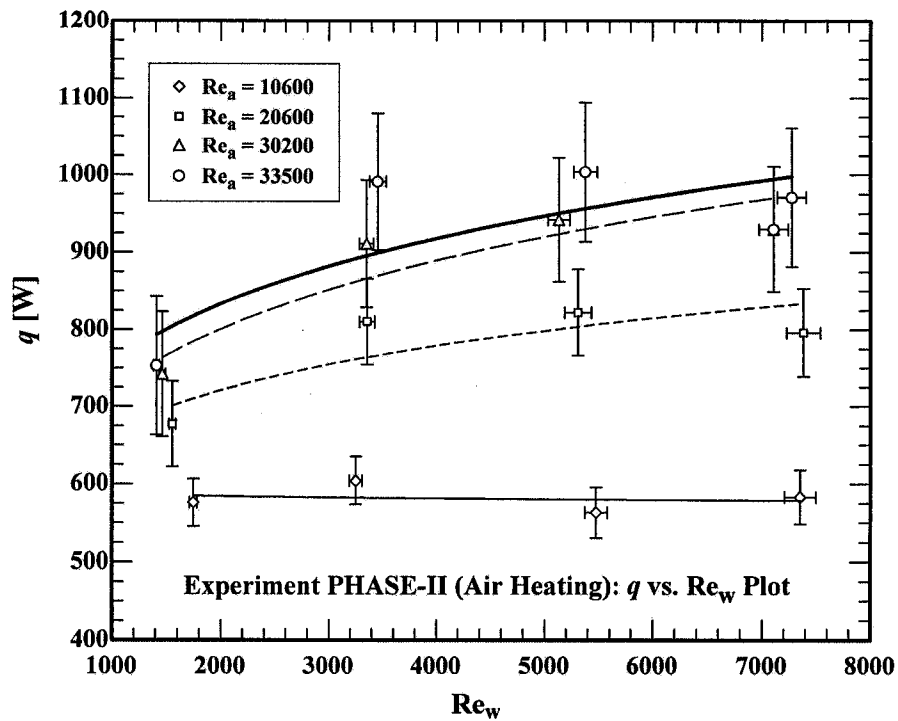


Figure 5.2.2 Change of q with Re_w for different Re_a (Phase-II: Air-heating Test)

In general, the q increases with the increase of both Re_w and Re_a for both cooling and heating tests, which is expected. The increase in q with increasing Re_w is slow compared to the increase in q with increasing Re_a . This trend shows that the increase in q is greatly dominated by the Re_a . The increase in q with respect to Re_a is clearly portrayed by the changing values of C_5 and C_6 . The effects of Re_a on q are discussed in greater details in Subsection 5.1.1. Corresponding to four different Re_a , Figure 5.2.1 shows the variation of q with Re_w in the range $1100 \leq Re_w \leq 3500$ and Figure 5.2.2 shows the variation in the range $1500 \leq Re_w \leq 7300$.

The nature of the variation of q with Re_w was found to be the same for all the ranges of Re_w as seen in Figures 5.2.1 and 5.2.2. The q/Re_w ratio and hence the increase in q per unit increase in Re_w , dq/dRe_w , decreases with increasing Re_w . This is consistent

with the power law effect of Re on q , that is, the effect of Re diminishes at large Re . The $\frac{\Delta q}{q}$ ratio is almost constant for different Re_a , but the $\frac{\Delta q}{\Delta Re_w}$ ratio for any given Re_a is smaller for smaller Re_a . Since the total thermal resistance R_{th} is larger for smaller Re_a , the q and hence the Δq are smaller for smaller Re_a .

For a given Re_w , it is seen that the value of q significantly increases with increasing Re_a in the range $10000 \leq Re_a \leq 27300$ in Figure 5.2.1 and in the range $10600 \leq Re_a \leq 30200$ in Figure 5.2.1 after that the q is less influenced by the change of Re_a . This can be clearly seen by the closeness of the $q-Re_w$ curves in the range $27300 < Re_a < 33200$ (Figure 5.2.1) and in the range $30200 < Re_a < 33500$ (Figure 5.2.2). This is may be due to the perturbation of boundary layer with increasing Re_a in the lower range of Re_a , which is described in Section 5.1.1. On the other hand, for a given Re_a , q was less influenced by the change of Re_w in the range $5300 \leq Re_w \leq 7300$ for the air-heating test (Figure 5.2.2). This slow down of q is due to the restrictions of the total thermal resistance R_{th} . The $R_{th,w}$ in the range $5300 \leq Re_w \leq 7300$ was found to be smaller compared to Re_w less than 5300, nevertheless any further increase in q through increasing Re_w was restricted by the higher $R_{th,a}$. There were some scatters in data attributable to the experimental error, which are within the estimated uncertainty as shown by the error bars in respective figures.

5.2.2 Effect of Reynolds number on Nusselt number ($Nu_w - Re_w$ relationship)

The waterside Nusselt number (Nu_w) was deduced using Eq. (4.5.13). The average Nu_w values with respect to Re_a corresponding to different Re_w are given in Tables B.1 and B.2 in Appendix B. The estimated uncertainty for Nu_w varied from 4.5 to 13.5% in all the experiment phases. To observe the variation of Nu_w with Re_w , Nu_w as a function of Re_w are plotted in Figures 5.2.3 and 5.2.4 corresponding to four different Re_a . Several curve fits have been examined and the power law fit in the following form was found to cover data better than others with reasonably high R^2 values,

$$Nu_w = C_7 Re_w^{C_8} \text{ in the range } 1100 \leq Re_a \leq 7300, \quad (5.2.2)$$

where C_3 and C_4 are the curve fit coefficients, which in addition to the respective coefficients of determination (R^2 values), are tabulated in Table 5.2.2.

Table 5.2.2 Curve fit Coefficients and R^2 Values for Eq. (5.2.2) and Figures 5.2.3 and 5.2.4 ($Nu_w - Re_w$ variation)

Experimental phases and test conditions	Re_a	C_7	C_8	R^2
Phase-I: Air Cooling ($T_{a,i}$ and $T_{w,i}$ maintained constant)	10000	1.636	0.206	0.98
	19800	0.919	0.286	0.93
	27300	0.477	0.381	0.99
	33200	0.529	0.365	0.99
Phase-II: Air Heating ($T_{a,i}$ and $T_{w,i}$ maintained constant)	10600	1.366	0.233	0.82
	20600	0.824	0.296	0.96
	30200	0.984	0.275	0.87
	33500	1.446	0.224	0.84

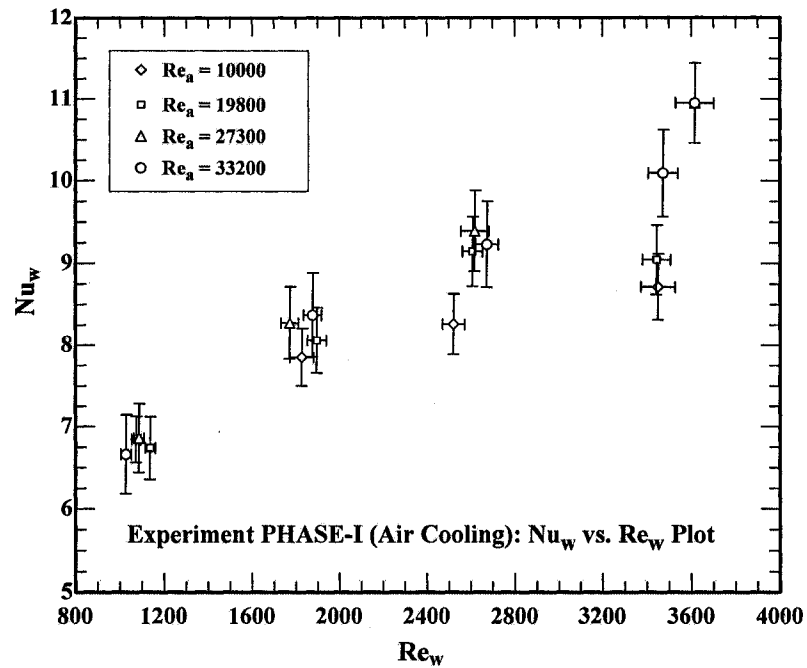


Figure 5.2.3 Change of Nu_w with Re_w for given Re_a (Phase-I: Air-cooling Test)

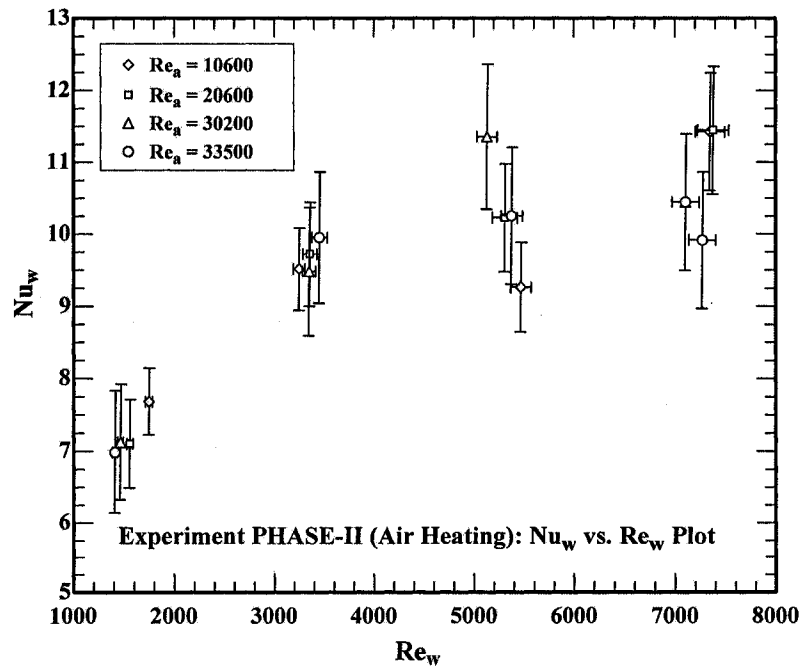


Figure 5.2.4 Change of Nu_w with Re_w for given Re_a (Phase-II: Air-heating Test)

Two representative cases, one for cooling (Phase-I) and the other for the heating (Phase-II) test, are presented here. Figure 5.2.3 shows the variation of Nu_w with Re_w in the range $1100 \leq Re_w \leq 3500$ and Figure 5.2.4 in the range $1500 \leq Re_w \leq 7300$. The trend of the variation of Nu_w with Re_w is found to be similar for both cooling and heating tests for all the Re_w investigated. That means, except for the few scatter data, for a given Re_a , the Nu_w increased with the increase of Re_w .

From Figures 5.2.3 and 5.2.4 and Table B.2, it is seen that as Re_a increases, the dq/dRe_w and dNu_w/dRe_w also change. For a given Re_a , the dq/dRe_w ratio is large at low Re_a where h_a is much lesser than h_w . That is, at $Re_a \approx 10000$ for cooling test: $h_a \approx 84$ as compared to $h_w \approx 391$ and at $Re_a \approx 10600$ for heating test: $h_a \approx 93$ as compared to $h_w \approx 523$. On the other hand, for the larger Re_a , the dq/dRe_w ratio is relatively smaller and h_a is relatively closer to h_w . For example for cooling test at $Re_a \approx 33000$, $h_a \approx 183$ as compared to $h_w \approx 426$ and for heating test at $Re_a \approx 33500$, $h_a \approx 182$ as compared to $h_w \approx 426$.

For cooling test in Figure 5.2.3, the negligible effect of Re_a is observed in the range $1100 \leq Re_w \leq 1800$ whereas for $Re_w \geq 2600$ much scatter is found, possibly due to the instability in the water flow. It is also noticed that for $Re > 20000$ the Nu_w - Re_w relation is not affected by Re_a . On the other hand, for air heating test in Figure 5.2.4, the negligible effect of Re_a is observed in the range $1500 \leq Re_w \leq 3400$ whereas for $Re_w > 5300$ many scatters are found, possibly due to instability in the water flow. These scatters in data are however within the expected uncertainty, which are shown in respective error bars in each of Figures 5.2.3 and 5.2.4.

Although the water mass flow rate was kept similar for both cooling and heating, in the analysis, in heating test a higher Nu_w (approximately by 20% higher than cooling tests) is found depending on the Re_w investigated. This higher heat transfer may have been attributed to the nature of the boundary layers, because hot water inside the tube possibly may have an unstable boundary layer causing the heat transfer to increase. As far as the variation of heat transfer due to the variation of fluid property is concerned, it is the viscosity at waterside that plays the major role. In heating test, the waterside bulk temperature was higher and hence the viscosity was smaller compared to the cooling test. For this reason, for a given water mass flow rate, the value of Re_w was higher in air heating than in air cooling test, causing the flow to become more turbulent and hence the increased heat transfers in heating test. Even in the same range of Re_w , the heat transfer was higher in heating process, which may have been attributed by the nature of development of the thermal over velocity boundary layer.

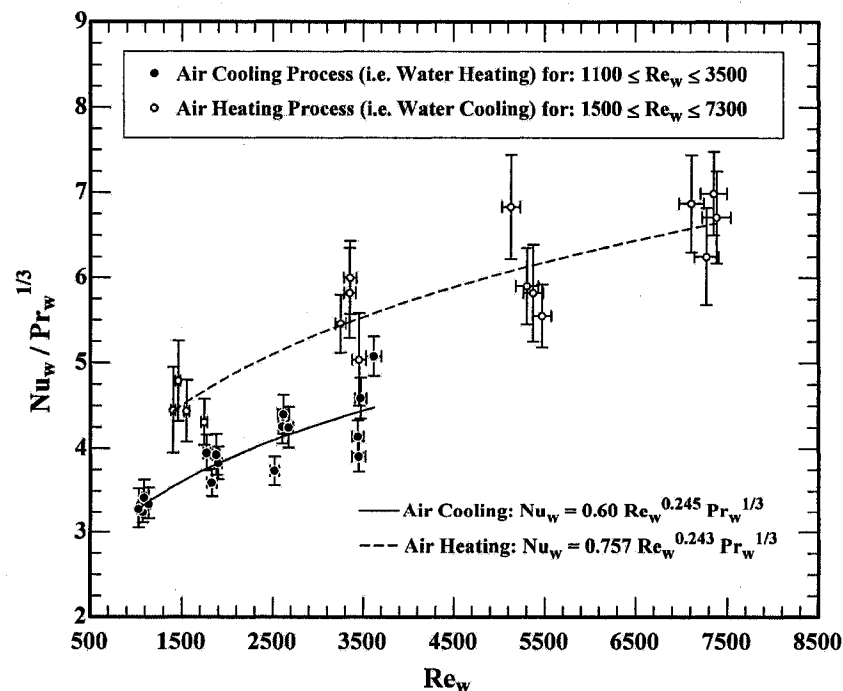


Figure 5.2.5 Nu_w – Re_w – Pr_w relationships for air cooling and heating (Error bars shown)

For the determination of Nu_w - Re_w relationship in Eq. (5.2.2) and plotting them in Figures 5.2.3 and 5.2.4, the Prandtl effect was not included. As the waterside bulk temperature, $T_{w,b}$, varied between 5.5 and 38°C during the tests, the Prandtl number also considerably varied, i.e. from 4.5 to 11. This variation was taken into account by introducing the Pr_w in the Nu_w - Re_w relationship. As shown in Figure 5.2.5, with the inclusion of Prandtl effects (Pr_w), the overall average Nu_w - Re_w correlations were obtained for both cooling and heating in light of Eq. (4.4.5) in Section 4.4 as follows

$$Nu_w = 0.60 Re_w^{0.245} Pr_w^{1/3}, \text{ for } 1100 \leq Re_a \leq 3500 \text{ (Cooling the Air)}, \quad (5.2.3)$$

and

$$Nu_w = 0.76 Re_w^{0.243} Pr_w^{1/3}, \text{ for } 1500 \leq Re_a \leq 7300 \text{ (Heating the Air)}. \quad (5.2.4)$$

The results were compared with other available similar studies as described in subsection 5.2.3 and as shown in Figure 5.2.6.

5.2.3 Comparison of Current Nu_w - Re_w - Pr_w Correlations with other Studies

The waterside Reynolds number investigated was in the range $1100 \leq Re_w \leq 7300$, which indicates that the flow was both in the laminar, transition and turbulent regimes. In addition to this, the tube bends, flow fluctuations from supply line and structural vibration might have added some extra turbulence in the flow. In reality the flow probably was neither fully developed laminar nor fully developed turbulent one. To check this, experimentally obtained current correlations are compared in Figure 5.2.6 with other available similar studies and correlations that relate the Nusselt number with Reynolds number. These correlations can be very useful in determining the Nusselt

number for flow inside a tube, especially when the tube surface temperature is not known or difficult to quantify.

One such correlation proposed by Sieder and Tate (1936) for laminar flow inside a single straight circular tube at average tube surface temperature is

$$\text{Nu}_w = 1.86 \underbrace{\left(\frac{\text{Re}_w \text{Pr}_w}{L_t / D_{h,i}} \right)^{1/3}}_X \left(\frac{\mu_w}{\mu_{w,s}} \right)^{0.14}, \text{ for } 0.48 \leq \text{Pr}_w \leq 16700, \quad (5.2.5a)$$

where $\mu_{w,s}$ is taken at the tube surface temperature. The use of the above equation was recommended by Whitaker (1972) for $X \geq 2$. In current experiment X was always greater than 2 and the waterside Prandtl number ranged from 4.5 to 11. For non-circular cross section, the hydraulic diameter, $D_{h,i}$ is used in Eq. (5.2.5a). By introducing other parameters and conditions from the present experiment, Eq. (5.2.5a) can be modified to

$$\text{Nu}_w = 0.28 \text{Re}_w^{0.312} \text{Pr}_w^{1/3}, \text{ for } 4.5 \leq \text{Pr}_w \leq 11 \text{ and } 1100 \leq \text{Re}_w \leq 7300. \quad (5.2.5b)$$

This correlation leads to results, which though slightly lower, are quantitatively and qualitatively in satisfactory agreement with current results as shown in Figure 5.2.6.

Another correlation for fully developed laminar flow inside smooth straight circular duct under constant wall heat flux proposed by Shah and London (1978) and Shah and Bhatti (1987) (for $Y > 100$) is

$$\text{Nu}_w = \left[1.953 \left(\frac{\text{Re}_w \text{Pr}_w D_{h,i}}{L_t} \right)^{1/3} \right]. \quad (5.2.6a)$$

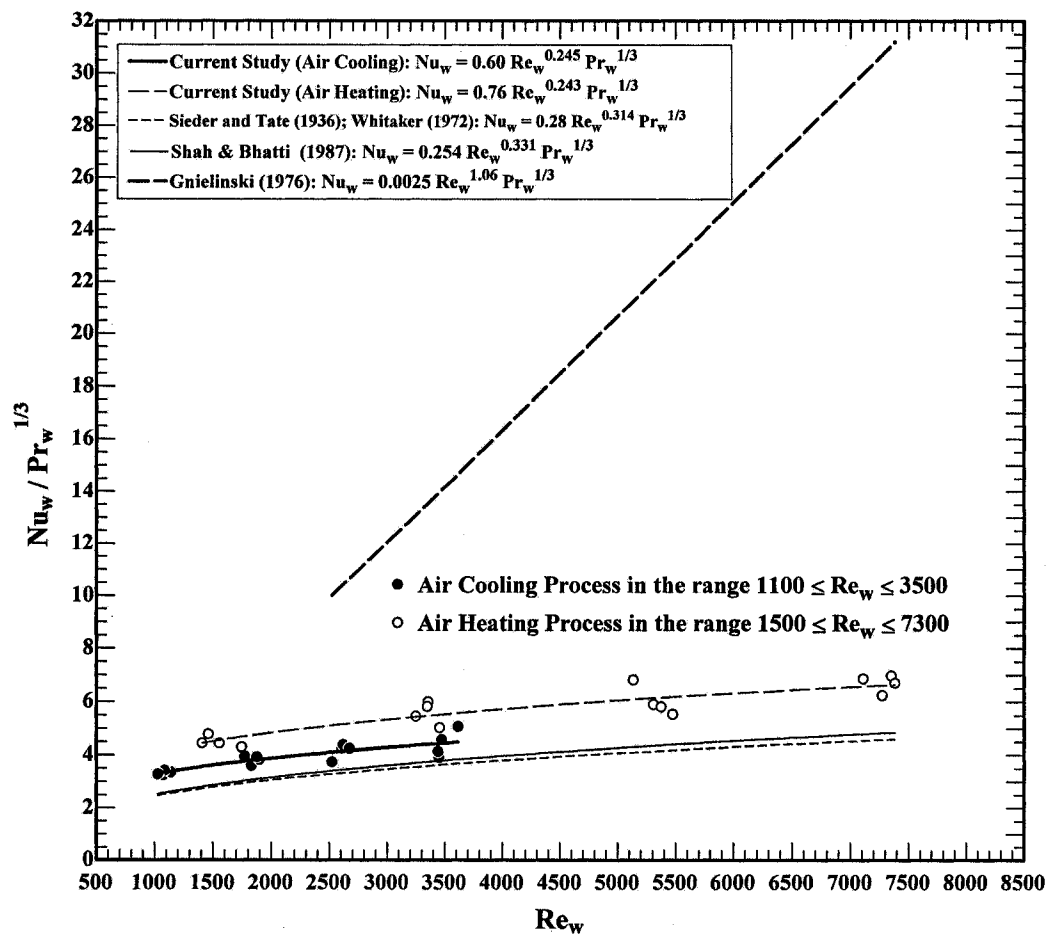


Figure 5.2.6 Comparison of current Nu_w - Re_w - Pr_w relationship with other correlations

Employing the conditions and parameters from the present experiment, Eq. (5.2.6a) can be re-written as

$$Nu_w = 0.25 Re_w^{0.32} Pr_w^{1/3}, \text{ for } 4.5 \leq Pr_w \leq 11 \text{ and } 1100 \leq Re_w \leq 7300. \quad (5.2.6b)$$

For the current study, Y values were less than 100. Nevertheless, results predicted using this correlation agreed reasonably well with the current values.

For the case of fully developed turbulent flow inside circular tube under constant heat flux condition, Gnielinski (1976) recommended a correlation for the range of $2300 \leq Re_w \leq 10000$ under constant heat flux condition as follows,

$$\text{Nu}_w = \frac{(f/2)(\text{Re}_w - 1000) \text{Pr}_w}{1 + 12.7(f/2)^{1/2}(\text{Pr}_w^{2/3} - 1)} \quad (5.2.7a)$$

The pipe friction factor in Eq. (5.2.7a) is evaluated from the following relation as cited by Sadik and Hongtan (2002):

$$f = (1.58 \ln \text{Re}_w - 3.28)^{-2} \quad (5.2.7b)$$

Sadik and Hongtan also mentioned that the effect of thermal boundary conditions can be neglected in turbulent forced convection and Eq. (5.2.7a) can be used for both constant wall heat flux and constant wall surface temperature conditions. Like before, under the current experimental conditions, Eq. (5.2.7a), could be reduced to

$$\text{Nu}_w = 0.0025 \text{Re}_w^{1.1} \text{Pr}_w^{1/3}, \text{ for } 4.5 \leq \text{Pr}_w \leq 11 \text{ and } 1100 \leq \text{Re}_w \leq 7300. \quad (5.2.7c)$$

From Figure 5.2.6, it is clear that Gnielinski's correlation for turbulent flow highly over-predicted the waterside Nusselt number in contrast to the current experimental results. This is expected, because turbulence lowers the thermal resistance and hence increases Nu and $d\text{Nu}/d\text{Re}$ is much larger for turbulent flow.

In terms of both qualitative and quantitative comparison, the current experimental results agreed well with the correlations proposed by Sieder and Tate (1936), Shah and London (1978), and Shah and Bhatti (1987) but not with the correlation of Gnielinski (1976). The present Nu_w values are somewhat higher, which is expected because in addition to the flow itself the flow was also disturbed by tube bends (similar to the effect made by tube entrance). However, it is obvious that the Reynolds number is a key factor to the heat transfer for the waterside too.

CHAPTER 6

CONCLUSIONS AND RECOMMENDATIONS

6. CONCLUSIONS AND RECOMMENDATIONS

Cooling and heating heat transfers of air flowing over an elliptical tube array heat exchanger were studied experimentally to investigate the effect of Reynolds number on Nusselt number. The cross flow heat transfer experiments, divided into four phases, were conducted in a closed-loop thermal wind tunnel, where air was flowing over the surface of the tube array and water was passing through inside of the tube array.

Two types of temperature loadings were applied. In first two phases (Phase - I and Phase - II), the inlet temperatures of the approach air and the entering water were maintained constant. In details they were $T_{a,i} \approx 41.5 \pm 1.5^\circ\text{C}$ and $T_{w,i} \approx 6.5 \pm 1.0^\circ\text{C}$ in Phase - I (air-cooling) and $T_{a,i} \approx 17.5 \pm 1.5^\circ\text{C}$ and $T_{w,i} \approx 38.8 \pm 0.8^\circ\text{C}$ in Phase - II (air heating) respectively. In the other two phases, Phase - III (air-cooling) and Phase - IV (air heating), the temperature difference between the approach air and the entering water was kept constant at $\Delta T_{a-w} \approx 15.7 \pm 1.5^\circ\text{C}$. The inner hydraulic diameter and the mean flow velocity of water inside the tube were used to determine the waterside Reynolds number (Re_w), and Nusselt number (Nu_w) while that of the streamwise outer major axis length of the tube and mean free stream air velocity at the test section inlet were used to estimate the airside Reynolds number (Re_a) and Nusselt number (Nu_a). The airside Reynolds numbers investigated were in the range $10000 < Re_a < 36000$ for all the experimental phases. The investigated waterside Reynolds number, on the other hand, was in the range $1100 < Re_w < 7300$ in Phase - I and Phase - II, and in the range $3300 < Re_w < 7100$ in Phase - III and Phase - IV. From the experimental and analytical observations, the following conclusions and recommendations are summarized from current study.

6.1 Conclusions

As the main objective of the current study was to investigate the Nu_a - Re_a relationship, the conclusions from the current study for airside analyses are presented below.

Airside Analysis

- Overall, the Reynolds number was found to be the key factor affecting the heat transfer mechanism. The Re_a dominated the increase in Nu_a . Also, the airside thermal resistance was found to be much higher, i.e. between 83 and 95% of the total thermal resistance, which dictated the overall heat transfer.
- The heat transfer rate (q) increased with increasing Re_a in a power law relationship and the increment was relatively faster at lower Re_a in the range $10000 \leq Re_a \leq 20000$ and slower afterwards up to $Re_a = 36000$. Increase in q with increasing Re_a was larger compared to the increase in q with increasing Re_w . Although the q - Re_a relationship was somewhat influenced by Re_w especially in the lower range of Re_w , it was however less affected by Re_w in the higher range of Re_w .
- The Nu_a invariably increased with increasing Re_a and the variation followed a power law relationship over the range and conditions considered. Expectedly, the Nu_a - Re_a relationship was found to be nearly independent of Re_w because of the higher airside thermal resistance.
- The direction of heat flow (i.e. the air cooling over heating) appeared to influence the Nu_a slightly. That means, for a given Re_a , the Nu_a was a little higher in air heating than in

cooling process over the range of Re_a investigated. However, within the experimental limitations and the estimated uncertainty; the difference of heat transfer between air-cooling and air heating tests could not be concluded. Thus, from all the tests, with negligible influence of Re_w , an overall unified Nu_a versus Re_a correlation was obtained in the presence of Pr_a as follows

$$Nu_a = 0.263 Re_a^{0.663} Pr_a^{1/3} \text{ for } 10000 < Re_a < 36000. \quad (5.1.5)$$

The correlation indicates that the incremental change in Nu_a per unit change in Re_a decreases with increasing Re_a and this diminishing trend is consistent with the power law relationship between Nu_a and Re_a .

- The current idealized experiment satisfactorily agreed with the qualitative results found in the literatures except a few scatters in data, which in most cases were within the estimated experimental uncertainties. Quantitatively current results predicted a higher Nu_a , which is expected because the results reported here are based on a very specific set of conditions tested, e.g. a relatively lower axis ratio, an array of tubes instead of a single cylinder and a unique characteristic length used to determine the Re and Nu .
- The dimensionless airflow pressure drop (C_{press}) across the tube array decreased with increasing Re_a and remained almost constant at 0.54 (for the whole array) and at 0.19 (for a single tube in the array) in the range $20000 < Re_a < 36000$. The C_{press} was found to vary with Re_a in an inverse power law manner. Within the experimental constraints, set conditions, and the locations of the pressure drop measuring taps used, the C_{press} - Re_a correlations were obtained in the range $20000 < Re_a < 36000$ as follows

$$C_{\text{press,array}} = \frac{7.70}{\text{Re}_a^{0.263}}, \text{ (Case-I: for whole array),} \quad (5.1.8)$$

and

$$C_{\text{press}} = \frac{2.70}{\text{Re}_a^{0.263}} \text{ (Case-II: for a single tube in the array).} \quad (5.1.9)$$

The $C_{\text{press}}\text{-Re}_a$ was compared with available literatures and very good qualitative and quantitative agreement was noticed.

Waterside Analysis

While the main focus of current study was on airside heat transfer characteristics, the analysis of waterside is also of interest. Thus, within the experimental set conditions and limitations, the following conclusions for waterside are summarized below.

- The Reynolds number was found to be the key factor influencing the heat transfer at waterside as well. Waterside thermal resistance was found to be relatively smaller i.e. between 5 and 17% of the total thermal resistance.
- The heat transfer rate (q) increased with increasing Re_w in a power manner. That is, the increase in q per unit increase in Re_w decreased with increasing Re_w . This diminishing effect is consistent with the power law relationship between q and Re_w . The increase in q with increasing Re_w could be observed to be significant in the lower range of Re_w and slow in the higher range of Re_w , which is expected because the airside thermal resistance ($R_{\text{th,a}}$) is higher and that it does not increase with increasing Re_w .

- The Nu_w increased with increasing Re_w in a power law relationship over the range of conditions considered. The Nu_w - Re_w relationship was less influenced by Re_a in the lower range of Re_w , i.e. $1100 \leq Re_w \leq 1800$ for air cooling and $1800 \leq Re_w \leq 3400$ for air heating. Unlike the airside, the direction of heat flow (i.e. the air cooling over heating) clearly influenced the Nu_w . That means, for a given Re_w , the Nu_w is always higher in air heating (approximately by 20%) than in air cooling process over the range of Re_w considered. The inclusion of Prandtl effect (Pr_w) somewhat minimized the Nu_w - Re_w relational differences between the air-cooling and air-heating tests but did not diminish. Thus, introducing the Pr_w , the following Nu_w - Re_w relationships for air-cooling and air-heating processes were obtained separately in the form,

$$Nu_w = 0.60 Re_w^{0.245} Pr_w^{1/3} \text{ (air cooling for } 1100 < Re_w < 3500), \quad (5.2.3)$$

and

$$Nu_w = 0.76 Re_w^{0.243} Pr_w^{1/3}, \text{ (air heating for } 1500 < Re_w < 7300). \quad (5.2.4)$$

- Although predicted somewhat higher Nu_w , the current result satisfactorily agreed with the results found in the literature.
- There were some scatters in data; however, in most cases they were found to be within the estimated experimental uncertainties.

6.2 Recommendations

The observations from the current study might help carrying forward further study and work in this subject area. The obtained correlations may be useful in real field

applications, where the heat exchanger configuration and the set operating conditions are similar to that of the current study. Nevertheless, present result can be verified and improved by further study with a broad spectrum of internal and external flow regimes and heat transfer conditions and by changing the shape, orientation, and spacing of the tubes in the array.

The current study can further be extended in at least the following ways, which the author strongly believes and recommends to be worthy are:

- o Comparison of current results with those of the circular ones within the similar set conditions,
- o Investigation of the current in-line single array heat exchanger by introducing fins,
- o Numerical investigation using current geometric configuration, parameters, and the set operating conditions, and
- o Use of a long pipe at the waterside inlet to eliminate the entrance effect on the experimental results.

If the existing experimental facility has to be used in further any such study, the following replacements and/or addition to the test rig are sincerely recommended, which the author believes will greatly help the experimenter to carryout efficient experimental works as well as will help improve the experimental results through the data collection accuracy.

1. Replacement of the current bucket-stopwatch-balance method for measuring water mass flow rate with any easily controllable device such as a flow meter or a mass flow controller,
2. Building of water supply and reservoir system, which is capable of controlling and supplying smooth water flow with a variety of temperature,
3. Replacement of the thermocouples with RTDs,
4. Installation of hot-wire anemometer or digital Pitot static tube (with traversing mechanism) for air velocity measurement,
5. Arrange a pressure measuring device to measure the absolute and differential pressures inside the test section,
6. Making sufficient pressure taps in the test chamber to measure the airflow pressure drop at a variety of locations,
7. Addition of a humidity sensor capable of controlling and monitoring the airside humidity inside the test section, and finally
8. Introduction of a data acquisition system for automated data collection for most of the associated parameters.

It is noted here that among the above-recommended experimental facilities, item 3 and 8 are already acquired, which can be used in any future studies on this area.

REFERENCES

REFERENCES

- Abernethy, R. B., Benedict, R. P. and Dowdell, R. B. 1985. ASME Measurement uncertainty. J. Fluids Eng., Trans. ASME, Vol. 107, pp. 161-164.
- Badr, H. M. 1998. Forced convection from a straight elliptical tube. Heat and Mass Transfer, Vol. 34, pp. 229-236.
- Brauer, H. 1964. Compact Heat Exchangers. Chem. Process Eng., pp. 451-460.
- Cengel, Y. A. 2003. Heat Transfer - a practical approach. New York: McGraw-Hill Companies, Inc.
- Churchill, S. W. and Brier, I. C. 1955. Convective heat transfer from a gas stream at high temperature to a circular cylinder normal to the flow. Chem. Eng. Prog. Symp. Ser., Vol. 51, pp. 57-65.
- Coleman, H. W. and Steele, W. G. 1989. Experimentation and uncertainty analysis for engineers. New York: John Wiley & Sons.
- Dittus, F. W. and Boelter, L. M. K. 1930. Heat transfer in automobile radiators of the tubular type. University of California Publications in Engineering, Vol. 2, pp. 443-461.
- Ebadian, M. A., Topakoglu, H. C. and Arnas, O. A. 1986. On the convective heat transfer in a tube of elliptic cross section maintained under constant wall temperature. Journal of Heat Transfer, Trans. ASME, Vol. 108, pp. 33-39.
- Eckert, E. R. and Livingood, J. N. B. 1953. Method for calculation of laminar heat transfer in airflow around cylinders of arbitrary cross section. NASA-NACA Report No. 1118, pp. 223-251.
- Editorial. 1991. Journal of Fluids Engineering: Policy on Reporting Uncertainties in Experimental Measurements and Results. Journal of Fluids Engineering, Trans. ASME, Vol. 113, pp. 313-314.

- Editorial. 1993. Journal of Heat Transfer: Policy on Reporting Uncertainties in Experimental Measurements and Results. Journal of Heat Transfer, Trans. ASME, Vol. 115, pp. 5-6.
- Flow Kinetics LLC 2002. Using a Pitot static tube for velocity and flow measurements. An Internet article [Source - <http://www.flowmeterdirectory.com>].
- Gaddis, E. S. and Gnielinski, V. 1985. Pressure drop in cross flow across tube bundles. Int. J. Chem. Eng., Vol. 25, No. 1, pp. 1-15.
- Gaddis, E. S. and Gnielinski, V. 1997. Pressure drop on the shell side of shell-and-tube heat exchangers with segmental. J. Chem. Eng. Processing, Vol. 36, pp. 149-159.
- Gnielinski, V. 1976. New equations for heat and mass transfer in turbulent pipe and channel flow. Int. J. Chem. Eng. Vol. 16, No. 2, pp. 359-368.
- Gnielinski, V. 1979. Equations for calculating heat transfer in single tube rows and banks of tubes in transverse flow. Int. J. Chem. Eng., Vol. 19, No. 3, pp. 380-391.
- Gnielinski, V. 1983. Forced convection ducts. Heat Exchanger Design Handbook. Schlünder, E. U. ed., Washington, D. C.: Hemisphere.
- Gnielinski, V. 2002. Forced convection in ducts in Heat Exchanger Design Handbook 2002, Part 2, Edited by Hewitt, G. F. New York: Begell House, Inc.
- Harris, D. K. and Goldschmidt, V. W. 2002. Measurements of the overall heat transfer from combustion gases confined within elliptical tube heat exchangers. Experimental Thermal and Fluid Science, Vol. 26, pp. 33-37.
- Hasan, A. and Sirén, K. 2004. Performance investigation of plain circular and oval tube evaporatively cooled heat exchangers. Applied Thermal Engineering, Vol. 24, pp. 777-790.
- Hilpert, R.. 1933. Forsch. Gebiete Ingenieurwes., Vol. 4, p. 215.

- Incropera, F. P. and DeWitt, D. P. 2002. Fundamentals of Heat and Mass Transfer. 5th ed. New York: John Wiley & Sons, Inc.
- Kanefsky, P., Nelson, V. A., and Mary, R. 1999. A Systems Engineering Approach to Engine Cooling Design, S-1541, Society of Automotive Engineers, Inc., PA, (SAE Technical Paper # 1999-01-3780)
- Khan, M. G., Fartaj, A. and Ting, D. S-K. 2004a. An experimental characterization of cross-flow cooling of air via an in-line elliptical tube array. Int. Journal of Heat and Fluid Flow, Vol. 25, No. 4, pp. 636-648.
- Khan, M. G., Fartaj, A. and Ting, D. S-K. 2004b. An elliptical tube array as a cross flow heat exchanger in Heat Exchangers and Their Simulation, Thermal Management, and Fundamental Advances in Thermal and Fluid Sciences, Published by the Society of Automotive Engineers, Inc., PA, (SAE Technical Paper # 2004-01-0217), Vol. S-1818, pp. 151-160. (Presented at the SAE 2004 World Congress, March 2004, Detroit, USA).
- Khan, M. G., Fartaj, A. and Ting, D. S-K. 2005. Study of cross-flow cooling and heating of air via an elliptical tube array (Paper # TECH-00077-2004), American Society of Heating, Refrigerating, and Air-conditioning Engineers, Inc. (ASHRAE). Accepted for presentation in 2005 ASHRAE Winter Meeting, Feb. 2005, Orlando, FL, USA and accepted for subsequent publication in the ASHRAE Transaction.
- Shah, R. K. and Bhatti, M. S., 1987. Laminar convective heat transfer in ducts in Handbook of Single-Phase Convective Heat Transfer, Edited by Kakac, S., Shah, R. K. and Aung, W. (Chapter-3). New York: John Wiley & Sons.
- Kline, S. J. 1985. The purposes of uncertainty analysis. Journal of Fluids Engineering, Trans. ASME, Vol. 107, pp. 153-160.
- Kline, S. J. and McClintock, F. A. 1953. Describing uncertainties in single-sample experiments. Mechanical Engineering, Vol. 75, pp. 3-8.

- Laetitia G. and Kondjoyan, A. 2002. Complete map out of the heat transfer coefficient at the surface of two circular cylinders $H/D = 3.0$ and 0.30 subjected to a cross-flow of air. Int. Journal of Heat and Mass Transfer, Vol. 45, pp. 2597-2609.
- Lassahn, G. D. 1985. Uncertainty definition. Journal of Fluids Engineering, Trans. ASME, Vol. 107, pp. 179-182.
- Lienhard, J. H. IV and Lienhard, J. H. V. 2003. A Heat transfer textbook. 3rd ed., Phlogiston Press: Cambridge, Massachusetts.
- Lloyd, J. R. and Sparrow, E. M. 1970. Combined forced and free convection flow on vertical surfaces. Int. Journal of Heat and Mass Transfer, Vol. 13, pp 434-438.
- Merker, G. P. and Hanke, H. 1986. Heat transfer and pressure drop on the shell-side of tube-banks having oval-shaped. Int. Journal of Heat and Mass Transfer, Vol. 29, pp. 1903-1909.
- Matos, R. S., Vargas, J. V. C., Laursen, T. A. and Saboya, F. E. M. 2001. Optimization study and heat transfer comparison of staggered circular and elliptic tubes in forced convection. Int. Journal of Heat and Mass Transfer, Vol. 44, pp. 3953-3961.
- McAdams, W. H. 1942. Heat Transmission, 2nd edition. New York: McGraw-Hill.
- Moffat, R. J. 1985. Using uncertainty analysis in the planning of an experiment. J. Fluids Engg, Trans. ASME, Vol. 107, pp. 173-178.
- Nishiyama, H., Ota, T. and Matsuno, T. 1988. Heat transfer and flow around elliptic cylinders in tandem arrangement. JSME Int. Journal, Series II, Vol. 31, 3, pp. 410-419.
- Olsson, C.-O. and Sundén, B. 1996. Heat transfer and pressure drop characteristics of ten radiator tubes. Int. Journal of Heat and Mass Transfer, Vol. 39, No. 15, pp. 3211-3220.

- Ota T. and Nishiyama, H. 1984. Heat transfer and flow around an elliptic cylinder. Int. Journal of Heat and Mass Transfer, Vol. 27, No. 10, pp. 1771-1779.
- Ota, T., Nishiyama, H. and Taoka, Y. 1987. Flow around an elliptic cylinder in the critical Reynolds number regime. Journal of Fluids Eng., Trans. ASME, Vol. 109, pp. 149-155.
- Petukhov, B. S. 1970. Heat transfer and friction in turbulent pipe flow in Advances in Heat Transfer, Edited by Hartnett, J. P. and Irvine, T. F. Jr., New York: Academic Press. Vol. 6, pp. 503-564.
- Rahman, M. M., Salminen, E., and Siikonen, T. 2001. Heat transfer from circular and elliptic cylinders in cross-flow. 4th International Conference on Mechanical Engineering, Bangladesh University of Engineering and Technology, Dhaka, Bangladesh, Vol. 2, pp. 203-207.
- Rocha, L. A. O., Saboya, F. E. M. and Vargas, J. V. C. 1997. A comparative study of elliptical and circular sections in one- and two-row tubes and plate fin heat exchangers. Int. Journal of Heat and Fluid Flow, Vol. 18, No. 2, pp. 247-252.
- Rugh, J. P., Pearson, J. T., and Ramadhyani, S. 1992. A study of a very compact heat exchanger used for passenger compartment heating in automobiles. Compact Heat Exchangers for Power and Process Industries, Heat Transfer Division, ASME, Vol. 201, pp. 15-24.
- Sadik, K. and Hongtan, L. 2002. Heat Exchangers: Selection, Rating, and Thermal Design. Florida: CRC Press LLC.
- Sadik, K., Shah, R. K. and Aung, W. 1987. Handbook of Single-Phase Convective Heat Transfer. New York: John Wiley & Sons.
- Scholten, J. W. and Murray, D. B. 1995. Influence of direction of heat flow on Nusselt numbers for a gas-particle crossflow. Journal of Heat Transfer, Trans. ASME, Vol. 117, pp. 1088-1090.

- Schulenberg, F. J. 1966. Finned elliptical tubes and their application in air-cooled heat exchangers. Journal of Engineering for Industry, Trans. ASME, pp. 179-190.
- Seban, R.A. and Drake, R. M. 1955. Local heat transfer coefficients on the surface of an elliptical cylinder in a high-speed air. Trans. ASME, Vol. 75, pp. 235-240.
- Shah, R. K. and Bhatti, M. S., 1987. Laminar convective heat transfer in ducts in Handbook of Single-Phase Convective Heat Transfer, Edited by Kakac, S., Shah, R. K. and Aung, W. (Chapter-3). New York: John Wiley & Sons.
- Shah, R. K. and London, A. L. 1978. Laminar Forced Convection in Ducts. New York: Academic Press.
- Sieder, E. N. and Tate, G. E. 1936. Heat transfer and pressure drop of liquids in tubes. Ind. Eng. Chem. Vol. 28, pp. 1429-1436.
- Sohal, M. S. and O'Brien, J. E. 2001. Improving air-cooled condenser performance using winglets and oval tubes in a geothermal power plant. Geothermal Resources Council Transactions, Vol. 25, pp. 1-7.
- Sparrow, E. M. and Ramsey, J. W. 1978. Heat transfer and pressure drop for a staggered wall-attached array of cylinders with tip clearance. Int. Journal of Heat and Mass Transfer, Vol. 21, pp. 1369-1377.
- Wang, C.-C. 2000. Recent progress on the air-side performance of fin-and-tube heat exchangers. Int. Journal of Heat Exchangers, Vol. 1, pp. 49-76.
- Whitaker, S. 1972. Forced convection heat transfer correlations for flow in pipes, past flat plates, single cylinders, single spheres, and flow in packed beds and tubes. AIChE J., Vol. 18, pp. 361-371.
- Winterton, R. H. S. 1998. Where did the Dittus and Boelter equation come from? Int. Journal of Heat and Mass Transfer, Vol. 41, pp. 809-810.

- Žukauskas, A. 1972. Heat transfer from tubes in crossflow in Advances in Heat Transfer, Edited by Hartnett, J. P. and Irvine, T. F. Jr., New York: Academic Press. Vol. 8, pp. 93-160.
- Žukauskas, A. and Ambrazyavičius, A. B. 1961. Heat transfer of a plate in a liquid flow. Int. Journal of Heat and Mass Transfer, Vol. 3, pp. 305-309.
- Žukauskas, A. and Ulinskas, R. 1988. Heat transfer in tube banks in cross flow. Washington: Hemisphere Publishing Corporation.
- Žukauskas, A. and Žiugžda, R. 1985. Heat transfer of a cylinder in cross flow. Washington: Hemisphere Publishing Corporation.
- Žukauskas, A., Skrinska, A., Žiugžda, J., and Gnielinski, V. 2002. Banks of plain and finned tubes in Heat Exchanger Design Handbook 2002, Part 2, Edited by Hewitt, G. F. New York: Begell House, Inc.

APPENDIX - A

UNCERTAINTY ANALYSES AND ERROR ESTIMATIONS

APPENDIX – A: UNCERTAINTY ANALYSES AND ERROR ESTIMATIONS

An experimental investigation and the subsequent analyses may involve several parameters of various kinds. The experimental errors may originate from many sources, which influence each of the measured independent parameter. The errors from individual and independent parameters then propagate into the dependent parameters and finally into the end results according to the parametric relationships involved in the analysis. Each of the error sources may have two components, one is the *bias* and the other is the *precision*. For identifying the error limits, different assumptions and considerations were made and some logics and judgments were applied depending on the overall experimental situation. The issues were dealt in light of the ASME Journal of Heat Transfer Editorial (1993) and by consulting some other notable works on experimental uncertainty including Kline and McClintock (1953), Abernethy et al. (1985), Kline (1985), Lassahn (1985), Moffat (1985), Coleman and Steele (1989), and the ASME Journal of Fluids Engineering Editorial (1991).

A.1. Procedures of Addressing Uncertainty Issues

In current study, two kinds of key parameters were identified one is the independent and the other is the dependent parameters. The independent parameters are the basic fundamental parameters that were measured directly using instruments before or during the experimental runs. In this study, these were generally the basic dimensions of the tubes and the array such as $2a$, $2b$, a , b , L , and S_T and the basic experimental variables such as T , ΔT , p , Δp , m_w , and t . The dependent parameters, on the other hand are functions of the independent parameters and/or the thermophysical properties. The dependent parameters were not be measured directly. They could be calculated from the

measured independent parameters according to their functional relationships. The dependent parameters in current study were the dimensions of the elliptical tubes (i.e. L_t , A_c , P , D_h , and A_s), and the experimental variables (i.e. $T_{f,a}$, $T_{w,b}$, \dot{m} , q , h , V , Δp , C_{press} , Nu , Re , Pr etc.).

For the independent parameters that were directly measured from single sample measurements, the various bias (B) and precision (P) errors were calculated by using the root sum square (RSS) method as follows:

$$B = \pm\sqrt{B_1^2 + B_2^2 + \dots + B_x^2}, \quad (\text{A.1.1})$$

and

$$P = \pm\sqrt{P_1^2 + P_2^2 + \dots + P_x^2}, \quad (\text{A.1.2})$$

where, x = total number of error sources. The combined 95% confidence uncertainty (U) of all the errors were estimated by joining the individual elemental errors according to the following relation

$$U = \pm\sqrt{B^2 + P^2}. \quad (\text{A.1.3})$$

To find out the 0th order and also the 1st order uncertainty, the instruments' resolution and accuracy were considered as the *bias* errors and from the known and judged sources of information other associated error components (both *bias* and *precision*) were quantified.

For the independent parameters, which were directly measured as multiple sample measurements (i.e. the population is more than one); the bias errors (B) were taken to be the same as single measurement but the precision errors (P) at 95% confidence limit were calculated from statistical method using the standard deviation of the sample mean ($S_{\bar{H}}$) and t -distribution value as $P_{\bar{H}} = (t_{N-1,95\%})(S_{\bar{H}})$.

For the dependent parameters that were calculated from measured independent parameters, their uncertainties (U) were estimated by following the root sum square (RSS) method based on their functional relationships. Let us assume a dependent parameter, H , which is a function of other independent parameters such as $H_1, H_2, H_3 \dots$ etc. Then their relationship can be represented by,

$$H = f(H_1, H_2, H_3, \dots), \quad (\text{A.1.4})$$

and the absolute uncertainty can be estimated as,

$$U_H = \sqrt{\left(\frac{\partial H}{\partial H_1} U_{H_1}\right)^2 + \left(\frac{\partial H}{\partial H_2} U_{H_2}\right)^2 + \left(\frac{\partial H}{\partial H_3} U_{H_3}\right)^2 + \dots}, \quad (\text{A.1.5})$$

where the partial derivatives $\left(\frac{\partial H}{\partial H_1}, \frac{\partial H}{\partial H_2}, \frac{\partial H}{\partial H_3}, \dots\right)$ are derived from the functional relationship as given in Eq. (A.1.4) and the uncertainties of the independent parameters ($U_{H_1}, U_{H_2}, U_{H_3}, \dots$) are obtained from Eq. (A.1.3). As the uncertainty for any parameter, H , is generally represented by $H \pm U_H$, for clarity the sign for estimating uncertainty of the individual parameter is ignored in the analysis. The relative uncertainty is generally estimated as follows,

$$\frac{U_H}{H} = \frac{\sqrt{\left(\frac{\partial H}{\partial H_1} U_{H_1}\right)^2 + \left(\frac{\partial H}{\partial H_2} U_{H_2}\right)^2 + \left(\frac{\partial H}{\partial H_3} U_{H_3}\right)^2 + \dots}}{f(H_1, H_2, H_3, \dots)}, \quad (\text{A.1.6})$$

In the current study, there were as many as 48 individual experimental runs. The uncertainty analysis for each test case, for all the parameters involved in the experiment, was carried out explicitly and independently. However, without any preference, the sample uncertainty calculations of one typical run for air heating test was chosen to present in this thesis. The data of the typical run is given in Table A.1.1. The sample parametric calculations are presented below at the end of each subsection.

Table A.1.1 Sample Data for Air-heating test ($T_{w,i} > T_s > T_{a,i}$) – Measured and Calculated Values (Operating conditions: $\dot{m}_w \approx 0.06$ kg/s and $V_a \approx 9$ m/s)

Parameters	Mean value	Parameters	Mean value	Parameters	Mean value
$\overline{T_{a,i}}$	6.97 °C	$\overline{\Delta p_{array}}$	181.00 Pa	$\overline{Pr_w}$	6.45
$\overline{T_{a,o}}$	7.52 °C	$\overline{C_{press}}$	0.2073	$\overline{V_w}$	0.3382 m/s
$\overline{T_{a,o} - T_{a,i}}$	0.55 °C	$\overline{m_w}$	18.7674 kg	$\overline{Re_w}$	4232
$\overline{T_{s,o}}$	19.52 °C	\overline{t}	293.10 sec	$\overline{q_w}$	562.67 W
$\overline{T_{f,a}}$	13.25 °C	$\overline{\dot{m}_w}$	0.0641 kg/s	$\overline{q_a}$	559.40 W
$T_{f,a,max}$	14.09 °C	$\overline{T_{w,i}}$	24.10 °C	\overline{q}	561.04 W
$T_{f,a,min}$	12.64 °C	$\overline{T_{w,o}}$	22.00 °C	$\overline{h_a}$	116.30 W/m ² °C
$\overline{T_{s,o} - T_{a,i}}$	12.55 °C	$\overline{T_{w,i} - T_{w,o}}$	2.10 °C	$\overline{Nu_a}$	150
$\overline{c_{p,a}}$	1006.55 J/kg°C	$\overline{T_{w,b}}$	23.05 °C	$\overline{h_w}$	443 W/m ² °C
$\overline{k_a}$	0.02463 W/m°C	$T_{w,b,max}$	23.10 °C	$\overline{Nu_w}$	8.31
$\overline{\rho_a}$	1.2326 kg/m ³	$T_{w,b,min}$	23.00 °C	$\overline{T_{s,o,1}}$	21.03 °C
$\overline{\nu_a}$	1.455 x 10 ⁻⁵ m ² /s	$\overline{T_{s,i}}$	19.53 °C	$\overline{T_{s,o,2}}$	19.90 °C
$\overline{Pr_a}$	0.7328	$\overline{T_{w,b} - T_{s,i}}$	3.52 °C	$\overline{T_{s,o,3}}$	19.80 °C
$\overline{\Delta p_{pitot}}$	48.50 Pa	$\overline{c_{p,w}}$	4183.03 J/kg°C	$\overline{T_{s,o,4}}$	19.65 °C
$\overline{V_a}$	8.92 m/s	$\overline{k_w}$	0.60383 W/m°C	$\overline{T_{s,o,5}}$	18.95 °C
$\overline{Re_a}$	19292	$\overline{\rho_w}$	997.55 kg/m ³	$\overline{T_{s,o,6}}$	18.90 °C
$\overline{\dot{m}_a}$	1.011 kg/s	$\overline{\nu_w}$	9.338 x 10 ⁻⁷ m ² /s	$\overline{T_{s,o,7}}$	18.40 °C

A.2. Instrumental and Measurements' Uncertainties – Independent Parameters

Each of the instruments used in the study and the related individual measurements have errors associated with them. The way of addressing these errors are described in the following sections and subsections.

A.2.1. Measurement Uncertainties – Basic Independent Geometric Dimensions of the Tubes and the Array ($H = 2a_i, 2b_i, 2a_o, 2b_o, S_T$, or L)

All the dimensions of the elliptical tubes were measured for 18 populations using a DiGIMATIC 500-321 digital caliper. The caliper has an instrumental error (i.e. the accuracy) of $B_{\text{accuracy}} = B_I = 0.0254 \text{ mm} = 0.0000254 \text{ m}$ and an instrumental zero-order bias limit (i.e. the resolution) of $B_{\text{resolution}} = B_0 = 0.0127 \text{ mm} = 0.0000127 \text{ m}$. According to Eq. (A.1.1), the total 0th order bias error, which is fixed for other dimensional measurements in this series, was estimated to be,

$$B_{\overline{H}} = B_{\text{dimension}} = \sqrt{B_I^2 + B_0^2} = 2.8398 \times 10^{-2} \text{ mm} = 2.8398 \times 10^{-5} \text{ m} \quad (\text{A.2.1})$$

For each of the tubes, three to four repeated measurements were taken for every dimension and the data was recorded according to Eq. (A.2.2), where H is any parameter.

$$H_j = \frac{1}{n} \sum_{i=1}^n H_i, \text{ where } n = 3 \text{ to } 4 \text{ repeated measurements and } j = 1 \dots 18. \quad (\text{A.2.2})$$

The measured dimensions are tabulated in Table A.2.1. The sample mean (\overline{H}) and the sample standard deviation (S_H) of total 18 similar tubes were calculated as,

$$\overline{H} = \frac{1}{N} \sum_{j=1}^N H_j, \text{ where } N = \text{sample size or the total population} = 18, \quad (\text{A.2.3})$$

and

$$S_H = \sqrt{\frac{1}{N-1} \sum_{j=1}^N (H_j - \bar{H})^2} . \quad (\text{A.2.4})$$

The standard deviation of the mean ($S_{\bar{H}}$) for the sample was deduced using the following relation,

$$S_{\bar{H}} = \frac{S_H}{\sqrt{N}} . \quad (\text{A.2.5})$$

Table A.2.1 Tubes' independent dimensions, H , as measured by the digital Caliper

Inner sides of the tubes		Outer sides of the tubes		Tube-to-tube gap/spacing, $S_T \times 10^3$ (m)	Spanwise each tube length, L $\times 10^3$ (m)
Major Axis, $2a_i \times 10^3$ (m)	Minor Axis, $2b_i \times 10^3$ (m)	Major Axis, $2a_o \times 10^3$ (m)	Minor Axis, $2b_o \times 10^3$ (m)		
29.98	7.68	31.66	9.50	6.14	304.20
29.60	8.05	31.62	9.58	6.32	304.00
29.53	8.08	31.73	9.74	6.58	303.80
29.68	8.18	31.48	9.67	6.41	303.50
30.00	7.83	31.42	9.62	6.40	302.00
29.73	7.50	31.68	9.56	6.42	303.00
29.88	8.06	31.60	9.78	6.37	300.50
29.66	7.85	31.65	9.62	6.26	302.80
29.50	7.64	31.78	9.67	6.31	303.90
29.60	8.12	31.63	9.64	6.22	301.60
29.93	8.16	31.60	9.76	6.34	300.80
29.99	7.85	31.72	9.60	6.30	304.10
30.10	7.55	31.52	9.48	6.20	304.30
30.05	7.80	31.64	9.52	6.25	303.80
29.95	7.90	31.75	9.50	6.45	302.00
29.97	7.66	31.70	9.70	6.34	301.40
29.85	7.78	31.58	9.68	6.52	302.50
29.67	7.60	31.74	9.55	6.28	300.90
29.82*	7.85*	31.64*	9.62*	6.34*	302.73*

* Mean value of the sample, i.e. \bar{H}

Now using the student-t distribution at 95% confidence interval for $N-1$ degrees of freedom, the overall precision error limits, $P_{\text{dimension}}$ for all the dimensions were accounted as,

$$P_{\overline{H}} = P_{\text{dimension}} = t_{(N-1), 95\%} S_{\overline{H}} \cdot \quad (\text{A.2.6})$$

The overall uncertainties (absolute and relative) in dimensional measurements of the elliptical tubes and the array were calculated from the following relation,

$$U_{\overline{H}} = U_{\text{dimension}} = \pm \sqrt{\left(\frac{B_{\overline{H}}}{H}\right)^2 + \left(\frac{P_{\overline{H}}}{H}\right)^2} \text{ m, (absolute uncertainty),} \quad (\text{A.2.7a})$$

and

$$\frac{U_{\overline{H}}}{\overline{H}} = \frac{U_{\text{dimension}}}{\text{mean dimension}} = \pm \sqrt{\left(\frac{B_{\overline{H}}}{H}\right)^2 + \left(\frac{P_{\overline{H}}}{H}\right)^2} \text{ (relative uncertainty).} \quad (\text{A.2.7b})$$

SAMPLE CALCULATION – Uncertainty in Tube Outer Major Axis ($H = 2a_o$):

A sample calculation process is presented here for the overall uncertainty in the measurement of tube major axis length at outer side, $2a_o$. For the measurement of this dimension, the followings were calculated:

The bias error limit (Eq. A.2.1), which was fixed for all other dimensional measurements:

$$B_{\overline{H}} = B_{2a_o} = \sqrt{B_1^2 + B_0^2} = 2.8398 \times 10^{-2} \text{ mm} \approx 2.84 \times 10^{-5} \text{ m.} \quad (\text{A.2.8})$$

The sample mean, $\overline{H} = \overline{2a_o}$ (Eq. A.2.3):

$$\overline{H} = \overline{2a_o} = \frac{1}{N} \sum_{j=1}^N (2a_o)_j = \frac{1}{18} \sum_{j=1}^{18} (2a_o)_j = 31.64 \times 10^{-3} \text{ m.} \quad (\text{A.2.9})$$

The standard deviation of the sample, $S_H = S_{2a_o}$ (Eq. A.2.4):

$$S_H = S_{2a_o} = \sqrt{\frac{1}{N-1} \sum_{j=1}^N ((2a_o)_j - \overline{2a_o})^2} = \sqrt{\frac{1}{18-1} \sum_{j=1}^{18} ((2a_o)_j - \overline{2a_o})^2} = 9.63 \times 10^{-5} \text{ m.} \quad (\text{A.2.10})$$

The standard deviation of the sample mean, $S_{\overline{H}} = S_{\overline{2a_o}}$ (Eq. A.2.5):

$$S_{\overline{H}} = S_{\overline{2a_o}} = \frac{S_{2a_o}}{\sqrt{N}} = \frac{9.63 \times 10^{-5}}{\sqrt{18}} = 2.27 \times 10^{-5} \text{ m.} \quad (\text{A.2.11})$$

For $N - 1 = 18 - 1 = 17$ degrees of freedom, the t-distribution value at 95% confidence interval could be taken to be 2.11 (Coleman and Steele 1989). Thus the overall mean precision error limits, $P_{\overline{H}} = P_{\overline{2a_o}}$, was calculated by,

$$P_{\overline{H}} = P_{\overline{2a_o}} = t_{17, 95\%} S_{\overline{2a_o}} = 2.11 \times (2.27 \times 10^{-5}) = 4.79 \times 10^{-5} \text{ m.} \quad (\text{A.2.12})$$

The overall uncertainties in the measurement of tubes' mean outer major axis length was estimated using Eq. (A.2.7) and values from Eqs. (A.2.8), (A.2.9), and (A.2.12) as,

$$U_{\overline{H}} = U_{\overline{2a_o}} = \sqrt{\left(\frac{B_{\overline{2a_o}}}{2a_o}\right)^2 + \left(\frac{P_{\overline{2a_o}}}{2a_o}\right)^2} = 5.58 \times 10^{-5} \text{ m,} \quad (\text{A.2.13a})$$

in absolute value, or

$$\frac{U_{\overline{H}}}{\overline{H}} = \frac{U_{\overline{2a_o}}}{\overline{2a_o}} = \sqrt{\left(\frac{B_{\overline{2a_o}}}{\overline{2a_o}}\right)^2 + \left(\frac{P_{\overline{2a_o}}}{\overline{2a_o}}\right)^2} = 1.76 \times 10^{-3}, \quad (\text{A.2.13b})$$

in relative term or

$$U_{\overline{H}} (\%) = U_{\overline{2a_o}} (\%) = \left(\frac{U_{\overline{2a_o}}}{\overline{2a_o}}\right) \times 100 = (1.76 \times 10^{-3}) \times 100 \approx 0.18 \% , \quad (\text{A.2.13c})$$

in percentile form.

The overall measurement uncertainties of the other basic and independent dimensions of the tubes and the array such as $H = 2a_i$, a_i , $2b_i$, b_i , a_o , $2b_o$, b_o , S_T , and L ; whose calculations are not presented here; were estimated in the same way and are listed in Table A.2.2.

Table A.2.2 Uncertainties in Tubes' Basic Independent Dimensions (measured)

Tubes' Dimensional Parameters	Mean Value, $\bar{H} \times 10^3$ m	Bias Error, $B_{\bar{H}} \times 10^5$ m	Precision Error, $P_{\bar{H}} \times 10^5$ m	Absolute Uncertainty, $U_{\bar{H}} \times 10^5$ m	Relative (%) Uncertainty $\frac{U_{\bar{H}}}{\bar{H}} \times 100$	
Inner-side	Major Axis, $2a_i$	29.82	2.84	9.60	10.01	0.34
	Semi-major Axis, a_i	14.91	2.84	4.80	5.58	0.37
	Minor Axis, $2b_i$	7.85	2.84	10.85	11.22	1.43
	Semi-minor axis, b_i	3.92	2.84	5.43	6.12	1.56
Outer-side	Major Axis, $2a_o$	31.64	2.84	4.79	5.57	0.18
	Semi-major Axis, a_o	15.82	2.84	2.39	3.71	0.23
	Minor Axis, $2b_o$	9.62	2.84	4.58	5.39	0.56
	Semi-minor axis, b_o	4.81	2.84	2.29	3.65	0.76
Tube-to-tube gap, S_T	6.34	2.84	5.57	6.25	0.99	
Length of a single tube, L	302.73	2.84	64.57	64.63	0.21	

A.2.2. Measurement Uncertainties – Airside Pressure Differences ($H = \Delta p_{\text{pitot}}$ and Δp_{array})

The dynamic pressure (Δp_{pitot}) at the test section inlet by means of a Pitot static tube and the airflow pressure drop (Δp_{array}) across the tube array were measured to be the fundamental independent parameters to the calculations of the air velocity (V_a) and the airflow pressure coefficient (C_{press}). In both the measurements, a digital manometer

(Dwyer series 475 Mark III) was used, which measures pressures directly in Pa. The manometer has an accuracy of $\pm 1.5\%$ of the reading in Pa, giving an instrumental error of $B_{\text{accuracy}} = B_I = 1.5\%$ of $\Delta p_{\text{pitot}} = 0.015 \Delta p_{\text{pitot}}$. In absence of the resolution, this instrumental error could be considered to be the total 0th order bias error

$$B_{\overline{H},0} = B_{\text{manometer}} = \sqrt{B_I^2 + B_0^2} = \sqrt{B_I^2 + 0} = B_I = 0.015 \overline{\Delta p_{\text{pitot}}} \text{ Pa.} \quad (\text{A.2.14})$$

Due to different physical settings of the above two measurements, the associated bias (B) and the precision (P) errors, and hence the uncertainty (U) were estimated separately as described in the following sections.

Uncertainty in the Airside Dynamic Pressure at the Test section Inlet ($H = \Delta p_{\text{pitot}}$):

The Pitot-static tube has to be right-aligned for accurate measurement. Practically this may not be the case always, and in such situations some misalignment errors should be considered. To account for this error, an installation bias error of $\pm 1\%$ of the measured Δp_{pitot} was introduced (Coleman and Steele 1989) leading to a 1st order bias error of

$$B_{\overline{H},1} = B_{\text{installation}} = 0.01 \overline{\Delta p_{\text{pitot}}} \text{ Pa.} \quad (\text{A.2.15})$$

From Eqs. (A.2.14) and (A.2.15), the total bias errors for this measurement were estimated to be,

$$B_{\overline{H}} = B_{\overline{\Delta p_{\text{pitot}}}} = \sqrt{B_{\overline{H},0}^2 + B_{\overline{H},1}^2} = \sqrt{B_{\text{manometer}}^2 + B_{\text{installation}}^2} = 0.01803 \overline{\Delta p_{\text{pitot}}} \text{ Pa.} \quad (\text{A.2.16})$$

Based on the responses of the last digit of the manometer, a digital error (response of last digit) of $P_{\text{digit}} = \pm 0.5$ Pa was introduced as a precision error. In addition to this, a readability error of $P_{\text{reading}} = \pm 1$ Pa was considered as a precision error. Thus the total precision errors were estimated as

$$P_{\overline{H}} = P_{\Delta p_{\text{pitot}}} = \sqrt{P_{\text{digit}}^2 + P_{\text{reading}}^2} = \sqrt{(0.5)^2 + (1)^2} = 1.12 \text{ Pa} . \quad (\text{A.2.17})$$

The overall uncertainty in Δp_{pitot} measurement was estimated from Eq. (A.2.16) and (A.2.17) as

$$U_{\overline{H}} = U_{\Delta p_{\text{pitot}}} = \sqrt{\frac{B^2}{\Delta p_{\text{pitot}}} + \frac{P^2}{\Delta p_{\text{pitot}}}} = \sqrt{(0.01803 \Delta p_{\text{pitot}})^2 + 1.25} \text{ Pa} . \quad (\text{A.2.18a})$$

SAMPLE CALCULATION – Example experimental data Table A.1.1 ($H = \Delta p_{\text{pitot}}$):

For the mean airflow dynamic pressure at the test section inlet, $\overline{\Delta p_{\text{pitot}}} = 48.50 \text{ Pa}$, the absolute uncertainty were calculated from Eq. (A.2.18a) as

$$U_{\overline{H}} = U_{\Delta p_{\text{pitot}}} = \sqrt{(0.01803 \times 48.50)^2 + 1.25} \approx 1.42 \text{ Pa} , \quad (\text{A.2.18b})$$

and the relative uncertainty as

$$\frac{U_{\overline{H}}}{\overline{H}} = \frac{U_{\Delta p_{\text{pitot}}}}{\Delta p_{\text{pitot}}} = \frac{1.4194}{48.50} = 0.0293 \approx 2.93 \% . \quad (\text{A.2.18c})$$

Uncertainty in Airflow Pressure Difference across the Tube Array ($H = \Delta p_{\text{array}}$):

Based on measurement settings, the connecting tubes between the manometer and the pressure measuring taps were needed to open and refix several times during measurements, which may cause some error in instrumental readings. A tube fixation bias error of $\pm 1\%$ of the measured Δp_{array} was introduced to account for this error, giving a 1st order bias error of

$$B_{\overline{H},1} = B_{\text{tube fixation}} = 0.01 \overline{\Delta p_{\text{array}}} \text{ Pa} . \quad (\text{A.2.19})$$

From Eqs. (A.2.14) and (A.2.19), the total bias errors for this measurement were estimated to be,

$$B_{\overline{H}} = B_{\overline{\Delta p_{\text{array}}}} = \sqrt{B_{\text{manometer}}^2 + B_{\text{tube fixation}}^2} = 0.01803 \overline{\Delta p_{\text{array}}} \text{ Pa} . \quad (\text{A.2.20})$$

In this measurement, the readings of Δp_{array} were fluctuating especially in the lower range of air velocity. The digital error (response of last digit) of the manometer, as explained above in the Δp_{pitot} measurement section, is thus suppressed by this fluctuating nature of Δp_{array} readings. Thus an unsteadiness error of ± 5 Pa was considered as a precision error rather than the digital error. In addition to this, a readability error of $P_{\text{reading}} = \pm 1$ Pa, including the effect of the pressure tap locations, was also considered as a precision error. Thus the total precision error was estimated to be

$$P_{\overline{H}} = P_{\overline{\Delta p_{\text{array}}}} = \sqrt{P_{\text{fluctuation}}^2 + P_{\text{reading}}^2} = \sqrt{(5)^2 + (1)^2} = 5.10 \text{ Pa} . \quad (\text{A.2.21})$$

The overall uncertainty in Δp_{array} measurement was estimated from Eq. (A.2.20) and (A.2.21) as

$$U_{\overline{H}} = U_{\overline{\Delta p_{\text{array}}}} = \sqrt{B_{\overline{\Delta p_{\text{array}}}}^2 + P_{\overline{\Delta p_{\text{array}}}}^2} = \sqrt{(0.01803 \overline{\Delta p_{\text{array}}})^2 + 26} \text{ Pa} . \quad (\text{A.2.22a})$$

SAMPLE CALCULATION – Example experimental data Table A.1.1 ($H = \Delta p_{\text{array}}$):

For the mean airflow pressure difference across the tube array, $\overline{\Delta p_{\text{array}}} = 181.00$ Pa, the absolute uncertainty was calculated from Eq. (A.2.22a) as

$$U_{\overline{H}} = U_{\overline{\Delta p_{\text{array}}}} = \sqrt{(0.01803 \times 181)^2 + 26} \approx 6.05 \text{ Pa} , \quad (\text{A.2.22b})$$

and the relative uncertainty as

$$\frac{U_{\overline{H}}}{\overline{H}} = \frac{U_{\overline{\Delta p_{\text{array}}}}}{\overline{\Delta p_{\text{array}}}} = \frac{6.05392}{181.00} = 0.0334 \approx 3.34 \% . \quad (\text{A.2.22c})$$

A.2.3. Measurement Uncertainties – Temperatures ($H = T$ and ΔT)

As mentioned in subsection 3.4.1, all the temperatures were measured using a hand-held OMEGA HH506R digital thermometer and type-T thermocouples. The thermometer has an accuracy of $\pm(0.05\%$ of the reading $+ 0.2)^\circ\text{C}$ and a resolution of 0.05°C . Each of the thermocouple probes has an accuracy of $\pm 1^\circ\text{C}$ and a resolution of 0.025°C . The total elemental errors originating from the thermometer as well as from the thermocouples were considered separately as described below.

Errors associated with the digital thermometer alone:

The thermometer has two instrumental bias error components from its accuracy limit, which are $B_{\text{accuracy}, 1} = B_{I, 1} = 0.0005\bar{T}^\circ\text{C}$ and $B_{\text{accuracy}, 2} = B_{I, 2} = 0.2^\circ\text{C}$ and the instrumental zero-order bias limit (i.e. the resolution) of $B_{\text{resolution}} = B_0 = 0.05^\circ\text{C}$. According to Eq. (A.1.1), the total 0th order bias error was estimated to be,

$$B_{\bar{H}} = B_{\text{thermometer}} = \sqrt{B_{I,1}^2 + B_{I,2}^2 + B_0^2} = \sqrt{(0.0005\bar{T})^2 + 0.0425}. \quad (\text{A.2.23})$$

The temperature readings sometimes were fluctuating. There may also be an error associated with the recording of readings (human error). These sources of errors were considered to be the precision error. To account for these sources, an unsteadiness factor of 0.05°C and a readability error (usually the half of the least scale division of the thermometer) of 0.05°C were introduced. The total precision error was calculated as

$$P_{\bar{H}} = P_{\text{thermometer}} = \sqrt{P_{\text{fluctuation}}^2 + P_{\text{readability}}^2} = \sqrt{(0.05)^2 + (0.05)^2} = 0.07^\circ\text{C}. \quad (\text{A.2.24})$$

From Eqs. (A.2.23) and (A.2.24), the total uncertainty at the thermometer end was estimated to be

$$U_{\bar{H}} = \sqrt{B_{\bar{H}}^2 + P_{\bar{H}}^2} \Rightarrow U_{\text{thermometer}} = \sqrt{B_{\text{thermometer}}^2 + P_{\text{thermometer}}^2}, \quad (\text{A.2.25})$$

$$= \sqrt{(0.0005\bar{T})^2 + 0.0425 + (0.07)^2} = \sqrt{(0.0005\bar{T})^2 + 0.047} \text{ } ^\circ\text{C}.$$

Errors associated with the thermocouple probes and wires:

For the thermocouple probe, an instrumental bias error (i.e. the accuracy) of $B_{\text{accuracy}} = B_1 = 1^\circ\text{C}$ and an instrumental zero-order bias limit (i.e. the resolution) of $B_{\text{resolution}} = B_0 = 0.025^\circ\text{C}$ were considered. As many as 10 thermocouples were used in the experiment and each had a long wire to connect to the thermometer for reading temperature. The lengths of the wires were not the same and there may exist some probe-to-probe variations. To account for these errors, a factor for probe of $B_{\text{probe}} = 0.1^\circ\text{C}$ was introduced. Following Eq. (A.1.1), the total 0th order bias error for the thermocouple probes and the wires was estimated to be,

$$B_{\bar{H}} = B_{\text{thermocouple}} = \sqrt{B_1^2 + B_0^2 + B_{\text{probe}}^2} = \sqrt{1^2 + (0.025)^2 + (0.1)^2} = 1.005^\circ\text{C}. \quad (\text{A.2.26})$$

The thermocouple probes were placed at various locations in the test setup especially noticeable for the tube outer surface locations. This spatial variation may cause some precision errors in the reading for which a spatial error of $P_{\text{spatial}} = 0.05^\circ\text{C}$ was considered. Also, due to the measurement limitations (i.e. the usage of a single thermometer for recording all the temperatures) the terminals of these wires at thermometer end were repeatedly connected and disconnected, which may cause some errors. A temporal precision error of $P_{\text{temporal}} = 0.05^\circ\text{C}$ was considered. The conduction

along and the radiation from the leads were considered to be very less and thus were neglected and the total precision error at thermocouple end was calculated as

$$P_{\bar{H}} = P_{\text{thermocouple}} = \sqrt{P_{\text{spatial}}^2 + P_{\text{temporal}}^2} = \sqrt{(0.05)^2 + (0.05)^2} = 0.07^\circ\text{C}. \quad (\text{A.2.27})$$

From Eqs. (A.2.26) and (A.2.27), the total uncertainty at the thermocouple end was estimated to be

$$\begin{aligned} U_{\bar{H}} &= \sqrt{B_{\bar{H}}^2 + P_{\bar{H}}^2} \Rightarrow U_{\text{thermocouple}} = \sqrt{B_{\text{thermocouple}}^2 + P_{\text{thermocouple}}^2}, \quad (\text{A.2.28}) \\ &= \sqrt{(1.005)^2 + (0.07)^2} = 1.01^\circ\text{C}. \end{aligned}$$

Uncertainty in the non-differential Temperature Measurement ($H = T$):

From Eqs. (A.2.25) and (A.2.28), the overall uncertainty in temperature measurement together with the thermometer and thermocouple was estimated as

$$\begin{aligned} U_{\bar{H}} = U_{\bar{T}} &= \sqrt{U_{\text{thermometer}}^2 + U_{\text{thermocouple}}^2}, \quad (\text{A.2.29}) \\ &= \sqrt{(0.0005\bar{T})^2 + 0.047 + (1.01)^2} = \sqrt{(0.0005\bar{T})^2 + 1.06} \text{ } ^\circ\text{C}. \end{aligned}$$

Uncertainty in the differential Temperature Measurement ($H = \Delta T$):

The thermometer had a differential reading function by which, where applicable, the temperature differences such as $\Delta T_w = |T_{w,i} - T_{w,o}|$ and $\Delta T_a = |T_{a,i} - T_{a,o}|$, were measured directly. This correlated measurement helped damped out the bias errors leaving only some precision errors, which were accounted from Eqs. (A.2.24) and (A.2.27) as

$$U_{\bar{H}} = U_{\Delta T} = \sqrt{P_{\text{thermometer}}^2 + P_{\text{thermocouple}}^2} = \sqrt{(0.07)^2 + (0.07)^2} = 0.10^\circ\text{C}. \quad (\text{A.2.30})$$

A.2.4. Measurement Uncertainties – Water mass and collection time ($H=m_w$ & t)

For the calculation of water mass flow rate (\dot{m}_w), the fundamental parameters measured were the water mass (m_w) and the time (t) required to collect this mass in the flow. As mentioned in Section 3.4, the stopwatch-bucket-balance method was used for this measurement. The uncertainty associated with each component of the method are estimated separately as explained below.

Uncertainty in Recording the Time using a stopwatch ($H = t$):

The stopwatch has an instrumental bias error (i.e. the accuracy) of $B_{\text{accuracy}} = B_1 = 0.5$ sec and an instrumental zero-order bias limit (i.e. the half of the resolution) of $B_{\text{resolution}} = B_0 = 0.125$ sec. Any digital instrument may have a kind of digital error, which is usually taken as one half times the least digit of the instrument and is treated as bias error. For this stopwatch, the digital error was $B_{\text{digit}} = 0.05$ sec. Following Eq. (A.1.1), the total bias error associated with the stopwatch was estimated to be,

$$B_H = B_{\text{stopwatch}} = \sqrt{B_1^2 + B_0^2 + B_{\text{digit}}^2} = \sqrt{0.5^2 + 0.125^2 + 0.05^2} = 0.518 \text{ sec.} \quad (\text{A.2.31})$$

The error associated with readability, taken as one half times the least scale division of the stopwatch (i.e. 0.05 sec), was considered as precision error. A stopwatch handling precision error of 1 sec was also introduced to account for the errors in switching the stopwatch on and off in proper time during the collection of water mass. These gave a total precision error at the stopwatch end of

$$P_H = P_{\text{stopwatch}} = \sqrt{P_{\text{reading}}^2 + P_{\text{handling}}^2} = \sqrt{(0.05)^2 + 1^2} = 1.001 \text{ sec} \quad (\text{A.2.32})$$

From Eqs. (A.2.31) and (A.2.32), the overall uncertainty in recording time using the stopwatch was estimated as

$$U_{\bar{H}} = U_{\bar{t}} = \sqrt{B_{\text{stopwatch}}^2 + P_{\text{stopwatch}}^2} = \sqrt{(0.518)^2 + (1.001)^2} = 1.13 \text{ sec.} \quad (\text{A.2.33})$$

Uncertainty in Water Mass Measurement using bucket and balance ($H = m_w$):

The balance used in the experiment is graduated in pound scale (lb) to read any weight. The accuracy of the balance was taken to be equal to the least scale division of the balance (i.e. 0.1 lb = 0.046 kg) giving an instrumental bias error of $B_{\text{accuracy}} = B_1 = 0.046$ kg. The resolution of the balance was taken to be half of the accuracy (i.e. 0.05 lb = 0.023 kg) that gave an instrumental zero-order bias limit of $B_{\text{resolution}} = B_0 = 0.023$ kg. The bucket itself had no bias error involved. So, the total bias error for the balance was estimated according to Eq. (A.1.1) as

$$B_{\bar{H}} = B_{\text{balance}} = \sqrt{B_1^2 + B_0^2} = \sqrt{(0.046)^2 + (0.023)^2} = 0.0514 \text{ kg.} \quad (\text{A.2.34})$$

There were some errors involved in relation to bucket handling, which were treated as the precision errors. To account for this error, a precision error of $P_{\text{bucket}} = 0.2 \text{ lb} = 0.092 \text{ kg}$ was introduced. There may be some parallax error (human eyes) in recording the reading. To account for this error, a precision error equal to the least scale division of the balance was considered, which was $P_{\text{reading}} = 0.1 \text{ lb} = 0.023 \text{ kg}$. During the entire experiment, the water flow from the supply line was not always uniform. The fluctuating flow might have generated some errors in the process. A precision error for this fluctuation, equal to the least scale division of the balance, was

also considered. This error was $P_{\text{fluctuation}} = 0.1 \text{ lb} = 0.046 \text{ kg}$. The total precision error for bucket and balance was estimated as

$$\begin{aligned} P_{\overline{H}} = P_{\text{bucket-balance}} &= \sqrt{P_{\text{bucket}}^2 + P_{\text{reading}}^2 + P_{\text{fluctuation}}^2} \\ &= \sqrt{(0.092)^2 + (0.023)^2 + (0.046)^2} = 0.1054 \text{ kg}. \end{aligned} \quad (\text{A.2.35})$$

From Eqs. (A.2.34) and (A.2.35), the overall uncertainty in measuring the water mass using the bucket-balance was estimated to be

$$U_{\overline{H}} = U_{\overline{m_w}} = \sqrt{B_{\text{balance}}^2 + P_{\text{bucket-balance}}^2} = \sqrt{0.0514^2 + 0.1054^2} = 0.1173 \text{ kg}. \quad (\text{A.2.36})$$

All the uncertainties estimated above in subsections A.2.2, A.2.3, and A.2.4 are tabulated in Table A.2.3 below.

Table A.2.3 Uncertainties in Independent Experimental Parameters (measured)

Independent / fundamental Parameters	Representing Equation	Absolute Uncertainty, $U_{\overline{H}}$
Airside pressure difference by Pitot static tube at test section inlet, $U_{\overline{\Delta p_{\text{pitot}}}}$	(A.2.18a)	$\sqrt{(0.018 \overline{\Delta p_{\text{pitot}}})^2 + 1.25} \text{ Pa}$
Airside pressure difference across the elliptical tube array, $U_{\overline{\Delta p_{\text{array}}}}$	(A.2.22a)	$\sqrt{(0.01803 \overline{\Delta p_{\text{array}}})^2 + 26} \text{ Pa}$
Non-differential temperature, $U_{\overline{T}}$	(A.2.29)	$\sqrt{(0.0005 \overline{T})^2 + 1.06} \text{ }^\circ\text{C}$
Differential temperature, $U_{\overline{\Delta T}}$	(A.2.30)	0.10 $^\circ\text{C}$
Time for water mass collection, $U_{\overline{t}}$	(A.2.33)	1.13 sec
Water mass, $U_{\overline{m_w}}$	(A.2.36)	0.1173 kg

A.3. Uncertainties in the Evaluation of Thermophysical Properties of Air and Water ($H = c_p, \mu, \nu, Pr, \rho$)

All the thermophysical properties, if taken from any table, can be considered to bias error limit even they may have some precision error. Thus the uncertainty for thermophysical property is normally taken as the bias error. According to the Editorial of ASME Journal of Heat Transfer (1993) and Coleman and Steele (1989), the uncertainty for respective thermophysical property may be 0.25 to 0.5 times the absolute value or even higher. If not mentioned otherwise, the evaluations of the thermophysical properties were based on air film temperature ($T_{f,a}$) for air and water bulk temperatures ($T_{w,b}$) for water. As mentioned by Eq. (3.4.1) in Section 3.4, for a given operating condition, several times the temperatures were measured to give different population. From this populations, the mean, maximum, and minimum value could be obtained as required. As mentioned in Sections 4.2 and 4.5, the conduction and radiation heat transfers were ignored as such their effects in the evaluations of $T_{f,a}$ and $T_{w,b}$ were also neglected. The uncertainties in thermophysical properties of air and water at atmospheric pressure were estimated for airside as,

$$U_{\text{property}_a} = \frac{1}{2} \left| \left(\text{Property @ } T_{f,a, \max} - \text{Property @ } T_{f,a, \min} \right) \right|, \quad (\text{A.3.1})$$

and for waterside as,

$$U_{\text{property}_w} = \frac{1}{2} \left| \left(\text{Property @ } T_{w,b, \max} - \text{Property @ } T_{w,b, \min} \right) \right|. \quad (\text{A.3.2})$$

For evaluating fluid properties, the $T_{f,a}$ and $T_{w,b}$ need to be calculated first and so their uncertainties. To calculate the uncertainties in $T_{f,a}$, the uncertainties in $T_{s,o}$ needs to

be estimated first. In the following subsections, the calculations of uncertainties in $T_{s,o}$, $T_{f,a}$, and $T_{w,b}$ are presented.

A.3.1. Uncertainties in Tube Outer Surface Temperature Measurements ($H = T_{s,o}$):

As mentioned in Section 3.4.1, seven thermocouple probes were placed on seven suitably chosen tubes in the array. The variation of tube outer surface temperature from its inlet to exit were fairly linear as observed in the experiment. Thus the arithmetic average of these seven temperatures were taken to be the average tube outer surface temperature for all the analysis. The uncertainty associated with tube outer surface temperature, as a result of this linearized average, was dealt statistically as described below.

The total bias errors were taken from Eqs. (A.2.23) and (A.2.26) to be

$$B_{\overline{H}} = B_{\overline{T_{s,o}}} = \sqrt{B_{\text{thermometer}}^2 + B_{\text{thermocouple}}^2} \text{ } ^\circ\text{C} \quad (\text{A.3.3})$$

$$\text{or, } B_{\overline{T_{s,o}}} = \sqrt{(0.0005\overline{T_{s,o}})^2 + 0.0425 + (1.005)^2} = \sqrt{(0.0005\overline{T_{s,o}})^2 + 1.012} \text{ } ^\circ\text{C}.$$

The estimation of precision errors is as follows. For each of the seven tubes, three to four repeated measurements were taken for every operating condition and the data was recorded according to

$$H_j = (\overline{T_{s,o}})_j = \frac{1}{n} \sum_{i=1}^n (T_{s,o})_i, \text{ where } n = 3 \text{ to } 4 \text{ and } j = 1 \dots 7. \quad (\text{A.3.4})$$

The mean of the samples ($\overline{T_{s,o}}$) and the sample standard deviation (S_H) were calculated as,

$$\bar{H} = \overline{T_{s,o}} = \frac{1}{N} \sum_{j=1}^N (T_{s,o})_j = \frac{1}{7} \sum_{j=1}^7 (T_{s,o})_j, \text{ where } N = \text{sample size} = 7, \quad (\text{A.3.5})$$

and

$$S_H = S_{T_{s,o}} = \sqrt{\frac{1}{N-1} \sum_{j=1}^N ((T_{s,o})_j - \overline{T_{s,o}})^2} = \sqrt{\frac{1}{6} \sum_{j=1}^7 ((T_{s,o})_j - \overline{T_{s,o}})^2}. \quad (\text{A.3.6})$$

The standard deviation of the mean ($S_{\bar{H}}$) was deduced using the following relation,

$$S_{\bar{H}} = S_{\overline{T_{s,o}}} = \frac{S_{T_{s,o}}}{\sqrt{N}} = \sqrt{\frac{1}{42} \sum_{j=1}^7 ((T_{s,o})_j - \overline{T_{s,o}})^2}. \quad (\text{A.3.7})$$

Now using the student-t distribution at 95% confidence interval for $N-1 = 6$ degrees of freedom (i.e. $t = 2.447$), the overall precision error limits was estimated as,

$$P_{\bar{H}} = P_{\overline{T_{s,o}}} = t_{(6), 95\%} S_{\overline{T_{s,o}}} = (2.447) \left(\sqrt{\frac{1}{42} \sum_{j=1}^7 ((T_{s,o})_j - \overline{T_{s,o}})^2} \right). \quad (\text{A.3.8})$$

The overall uncertainties, absolute and relative (or percentage), were estimated from Eqs. (A.3.3) and (A.3.8) as,

$$U_{\bar{H}} = U_{\overline{T_{s,o}}} = \sqrt{B_{\overline{T_{s,o}}}^2 + P_{\overline{T_{s,o}}}^2} \text{ } ^\circ\text{C (absolute uncertainty),} \quad (\text{A.3.9a})$$

and

$$\frac{U_{\bar{H}}}{\bar{H}} (\%) = \frac{U_{\overline{T_{s,o}}}}{\overline{T_{s,o}}} (\%) = \sqrt{\left(\frac{B_{\overline{T_{s,o}}}}{\overline{T_{s,o}}} \right)^2 + \left(\frac{P_{\overline{T_{s,o}}}}{\overline{T_{s,o}}} \right)^2} \times 100\% \text{ (relative uncertainty).} \quad (\text{A.3.9b})$$

SAMPLE CALCULATION – Example Experimental Data Table A.1.1 ($H = T_{s,o}$):

The mean tube outer surface temperatures $T_{s,o,1}, T_{s,o,2}, \dots, T_{s,o,7}$, were measured to be 21.03, 19.90, 19.80, 19.65, 18.95, 18.90, and 18.40°C respectively. The mean of these seven temperatures were calculated from Eq. (A.3.5) to be $\overline{H} = \overline{T_{s,o}} = 19.52^\circ\text{C}$. The sample standard deviation (S_H) can be calculated from Eq. (A.3.6) to be $S_H = S_{T_{s,o}} = 0.863^\circ\text{C}$. The standard deviation of the mean ($S_{\overline{H}}$) is calculated from Eq. (A.3.7) to be $S_{\overline{H}} = S_{\overline{T_{s,o}}} = 0.326^\circ\text{C}$. So, the precision error can be calculated from Eq. (A.3.8) to be $P_{\overline{H}} = P_{\overline{T_{s,o}}} = 0.798^\circ\text{C}$. By taking the bias error from Eq. (A.3.3), the absolute uncertainty can be estimated from Eq. (A.3.9a) as

$$U_{\overline{T_{s,o}}} = \sqrt{B_{\overline{T_{s,o}}}^2 + P_{\overline{T_{s,o}}}^2} = \sqrt{(0.0005 \times 19.52)^2 + 1.012 + (0.799)^2} = 1.29^\circ\text{C}, \quad (\text{A.3.10a})$$

and the relative uncertainty from Eq. (A.3.9b) in percentile form as

$$\frac{U_{\overline{H}}}{\overline{H}} = \frac{U_{\overline{T_{s,o}}}}{\overline{T_{s,o}}} = \sqrt{\left(\frac{B_{\overline{T_{s,o}}}}{\overline{T_{s,o}}}\right)^2 + \left(\frac{P_{\overline{T_{s,o}}}}{\overline{T_{s,o}}}\right)^2} = 0.0666 = 6.66\%. \quad (\text{A.3.10b})$$

A.3.2. Uncertainties in the Determination of Airside Film Temperature ($H = T_{f,a}$):

The airside film temperature ($T_{f,a}$), generally used to evaluate the thermophysical properties of air, is defined as

$$\overline{H} = \overline{T_{f,a}} = \frac{\overline{T_{a,i}} + \overline{T_{s,o}}}{2} \text{ } ^\circ\text{C} \quad (\text{A.3.11})$$

and its partial derivatives are

$$\frac{\partial \overline{T_{f,a}}}{\partial \overline{T_{a,i}}} = \frac{1}{2} \quad \text{and} \quad \frac{\partial \overline{T_{f,a}}}{\partial \overline{T_{s,o}}} = \frac{1}{2}. \quad (\text{A.3.12})$$

The uncertainty associated with this film temperature is given by

$$U_{\overline{H}} = U_{\overline{T_{f,a}}} = \sqrt{\left(\frac{\partial \overline{T_{f,a}}}{\partial \overline{T_{a,i}}} U_{\overline{T_{a,i}}}\right)^2 + \left(\frac{\partial \overline{T_{f,a}}}{\partial \overline{T_{s,o}}} U_{\overline{T_{s,o}}}\right)^2} = \frac{1}{2} \sqrt{(U_{\overline{T_{a,i}}})^2 + (U_{\overline{T_{s,o}}})^2} \text{ } ^\circ\text{C}, \quad (\text{A.3.13a})$$

where the partial derivatives are taken from Eq. (A.3.12). The uncertainty components; $U_{\overline{T_{a,i}}}$ is taken from Table A.2.3 or Eq. (A.2.29) and $U_{\overline{T_{s,o}}}$ from Eq. (A.3.9). The relative uncertainty (in percentage) was estimated to be

$$\frac{U_{\overline{H}}}{\overline{H}} (\%) = \frac{U_{\overline{T_{f,a}}}}{\overline{T_{f,a}}} (\%) = \frac{1}{\overline{T_{a,i}} + \overline{T_{s,o}}} \sqrt{(U_{\overline{T_{a,i}}})^2 + (U_{\overline{T_{s,o}}})^2} \times 100\%. \quad (\text{A.3.13b})$$

SAMPLE CALCULATION – Example Experimental Data Table A.1.1 ($H = T_{f,a}$):

For the example experimental run, the mean air inlet and tube outer surface temperatures are listed in Table A.1.1 as $\overline{T_{a,i}} = 6.97^\circ\text{C}$ and $\overline{T_{s,o}} = 19.52^\circ\text{C}$ respectively. The absolute uncertainty in the tube outer surface temperature is obtained from Eq. (A.3.10a) to be $U_{\overline{T_{s,o}}} = 0.97^\circ\text{C}$ and the absolute uncertainty in the air inlet temperature is estimated from Table A.2.3 or Eq. (A.2.29) as

$$U_{\overline{H}} = U_{\overline{T_{a,i}}} = \sqrt{(0.0005\overline{T_{a,i}})^2 + 1.06} = \sqrt{(0.0005 \times 6.97)^2 + 1.06} \approx 1.03^\circ\text{C}.$$

From Eq. (A.3.13a), the absolute uncertainty in $T_{f,a}$ is calculated to be

$$U_{\overline{H}} = U_{\overline{T_{f,a}}} = \frac{1}{2} \sqrt{(U_{\overline{T_{a,i}}})^2 + (U_{\overline{T_{s,o}}})^2} = \frac{1}{2} \sqrt{(1.03)^2 + (1.29)^2} = 0.82^\circ\text{C}, \quad (\text{A.3.13c})$$

and the relative uncertainty is estimated from Eq. (A.3.13b) to be

$$\frac{U_{\overline{H}}}{\overline{H}} = \frac{U_{\overline{T_{f,a}}}}{\overline{T_{f,a}}} = \frac{1}{\overline{T_{a,i}} + \overline{T_{s,o}}} \sqrt{(U_{\overline{T_{a,i}}})^2 + (U_{\overline{T_{s,o}}})^2} \approx 0.0623 \approx 6.23\%. \quad (\text{A.3.13d})$$

A.3.3. Uncertainties in the Determination of Waterside Bulk Temperature ($H=T_{w,b}$)

The waterside bulk temperature ($T_{w,b}$), generally used to evaluate the thermophysical properties of water, is defined as

$$\overline{H} = \overline{T_{w,b}} = \frac{\overline{T_{w,i}} + \overline{T_{w,o}}}{2} \text{ } ^\circ\text{C} \quad (\text{A.3.14})$$

and its partial derivatives are

$$\frac{\partial \overline{T_{w,b}}}{\partial \overline{T_{w,i}}} = \frac{1}{2} \text{ and } \frac{\partial \overline{T_{w,b}}}{\partial \overline{T_{w,o}}} = \frac{1}{2}. \quad (\text{A.3.15})$$

The uncertainty associated with this bulk temperature is given by

$$U_{\overline{H}} = U_{\overline{T_{w,b}}} = \sqrt{\left(\frac{\partial \overline{T_{w,b}}}{\partial \overline{T_{w,i}}} U_{\overline{T_{w,i}}}\right)^2 + \left(\frac{\partial \overline{T_{w,b}}}{\partial \overline{T_{w,o}}} U_{\overline{T_{w,o}}}\right)^2} = \frac{1}{2} \sqrt{(U_{\overline{T_{w,i}}})^2 + (U_{\overline{T_{w,o}}})^2} \text{ } ^\circ\text{C}, \quad (\text{A.3.16a})$$

where the partial derivatives are taken from Eq. (A.3.15) and the uncertainty components; $U_{\overline{T_{w,i}}}$ and $U_{\overline{T_{w,o}}}$ are taken from Table A.2.3 or Eq. (A.2.29). The relative uncertainty (in percentage) was estimated to be

$$\frac{U_{\overline{H}}}{\overline{H}} (\%) = \frac{U_{\overline{T_{w,b}}}}{\overline{T_{w,b}}} (\%) = \frac{1}{\overline{T_{w,i}} + \overline{T_{w,o}}} \sqrt{(U_{\overline{T_{w,i}}})^2 + (U_{\overline{T_{w,o}}})^2} \times 100\%. \quad (\text{A.3.16b})$$

SAMPLE CALCULATION – Example Experimental Data Table A.1.1 ($H = T_{w,b}$):

Table A.1.1: $\overline{T_{w,i}} = 24.10^\circ\text{C}$ and $\overline{T_{w,o}} = 22.00^\circ\text{C}$. The absolute uncertainties in these two temperatures are obtained from Table A.2.3 and Eq. (A.2.29) to be

$$U_{\overline{H}} = U_{\overline{T_{w,i}}} = \sqrt{(0.0005\overline{T_{w,i}})^2 + 1.06} = \sqrt{(0.0005 \times 24.10)^2 + 1.06} \approx 1.03^\circ\text{C}$$

and

$$U_{\overline{H}} = U_{\overline{T_{w,o}}} = \sqrt{(0.0005\overline{T_{w,o}})^2 + 1.06} = \sqrt{(0.0005 \times 22.00)^2 + 0.562} \approx 1.03^\circ\text{C}.$$

The absolute and relative uncertainties in waterside bulk temperatures are estimated from Eqs. (A.3.16a) and (A.3.16b) as

$$U_{\overline{H}} = U_{\overline{T_{w,b}}} = \frac{1}{2} \sqrt{(U_{\overline{T_{w,i}}})^2 + (U_{\overline{T_{w,o}}})^2} = \frac{1}{2} \sqrt{(1.03)^2 + (1.03)^2} = 0.73^\circ\text{C}, \quad (\text{A.3.16c})$$

and

$$\frac{U_{\overline{H}}}{\overline{H}} = \frac{U_{\overline{T_{w,b}}}}{\overline{T_{w,b}}} = \frac{1}{\overline{T_{w,i}} + \overline{T_{w,o}}} \sqrt{(U_{\overline{T_{w,i}}})^2 + (U_{\overline{T_{w,o}}})^2} \approx 0.0315 \approx 3.16\%. \quad (\text{A.3.16d})$$

A.3.4. Sample Calculations of Uncertainties in Thermophysical Properties

$(H = c_p, \mu, \nu, \text{Pr}, \rho)$:

Over the experimental duration, the atmospheric pressure inside test section might have varied. Considering the location and time of the experiments and weather conditions of each experimental day, the variation was observed to be very little, e.g. ± 0.5 kPa. This variation was within the estimated uncertainty. Nevertheless, the fluid properties was evaluated at the actual pressure measured inside the test section inlet during experiment. So, the effect of variation of atmospheric pressure needed not to be considered. For the mean, maximum, and minimum airside film and waterside bulk temperatures, as given in Table A.1.1, the airside and waterside thermophysical properties at atmospheric pressure and hence the respective uncertainty components were estimated according to Eqs. (A.3.1) and (A.3.2) as follows.

AIRSIDE PROPERTIES

As presented in Table A.1.1, the mean value was taken at $\overline{T_{f,a}} = 13.25^\circ\text{C}$, and the uncertainties in absolute and relative terms were within the range of $T_{f,a,\max} = 14.09^\circ\text{C}$, and $T_{f,a,\min} = 12.64^\circ\text{C}$:

Specific Heat at constant pressure ($\overline{c_{p,a}} = 1006.55 \text{ J/kg}^\circ\text{C}$):

$$\text{Absolute: } U_{\overline{c_{p,a}}} = \frac{1}{2} \left| c_{p,a} @ T_{f,a,\max} - c_{p,a} @ T_{f,a,\min} \right| = 0.010735 \frac{\text{J}}{\text{kg}^\circ\text{C}}, \text{ and} \quad (\text{A.3.17a})$$

$$\text{Relative: } \frac{U_{\overline{c_{p,a}}}}{\overline{c_{p,a}}} = \frac{0.010735}{1006.55} = 1.0665 \times 10^{-5} \approx 1.0665 \times 10^{-3} \% . \quad (\text{A.3.17b})$$

Thermal Conductivity ($\overline{k_a} = 0.02463 \text{ W/m}^\circ\text{C}$):

$$\text{Absolute: } U_{\overline{k_a}} = \frac{1}{2} \left| k_a @ T_{f,a,\max} - k_a @ T_{f,a,\min} \right| = 5.434 \times 10^{-5} \frac{\text{W}}{\text{m}^\circ\text{C}}, \text{ and} \quad (\text{A.3.18a})$$

$$\text{Relative: } \frac{U_{\overline{k_a}}}{\overline{k_a}} = \frac{5.434 \times 10^{-5}}{0.024632} = 0.002206 \text{ W/m}^\circ\text{C} \approx 0.221 \% . \quad (\text{A.3.18b})$$

Density ($\overline{\rho_a} = 1.2326 \text{ kg/m}^3$):

$$\text{Absolute: } U_{\overline{\rho_a}} = \frac{1}{2} \left| \rho_a @ T_{f,a,\max} - \rho_a @ T_{f,a,\min} \right| = 3.1177 \times 10^{-3} \frac{\text{kg}}{\text{m}^3}, \text{ and} \quad (\text{A.3.19a})$$

$$\text{Relative: } \frac{U_{\overline{\rho_a}}}{\overline{\rho_a}} = \frac{3.1177 \times 10^{-3}}{1.232631} = 2.59 \times 10^{-3} \approx 0.253 \% . \quad (\text{A.3.19b})$$

Kinematic Viscosity ($\overline{\nu_a} = 1.455 \times 10^{-5} \text{ m}^2/\text{s}$):

$$\text{Absolute: } U_{\overline{\nu_a}} = \frac{1}{2} \left| \left(\nu_a @ T_{f,a, \max} - \nu_a @ T_{f,a, \min} \right) \right| = 6.5 \times 10^{-8} \frac{\text{m}^2}{\text{s}}, \text{ and} \quad (\text{A.3.20a})$$

$$\text{Relative: } \frac{U_{\overline{\nu_a}}}{\overline{\nu_a}} = \frac{6.5 \times 10^{-8}}{1.4548 \times 10^{-5}} = 34.468 \times 10^{-3} \approx 0.447 \%. \quad (\text{A.3.20b})$$

Prandtl Number ($\overline{\text{Pr}_a} = 0.7328$):

$$\text{Absolute: } U_{\overline{\text{Pr}_a}} = \frac{1}{2} \left| \left(\text{Pr}_a @ T_{f,a, \max} - \text{Pr}_a @ T_{f,a, \min} \right) \right| = 1.96 \times 10^{-4}, \text{ and} \quad (\text{A.3.21a})$$

$$\text{Relative: } \frac{U_{\overline{\text{Pr}_a}}}{\overline{\text{Pr}_a}} = \frac{1.96 \times 10^{-4}}{0.7328} = 2.67 \times 10^{-4} \approx 0.028 \%. \quad (\text{A.3.21b})$$

WATERSIDE PROPERTIES

As listed in Table A.1.1, the mean value was taken at $T_{w,b} = 23.05^\circ\text{C}$, and the uncertainties in absolute and relative terms were estimated within the range of $T_{w,b, \max} = 23.10^\circ\text{C}$ and $T_{w,b, \min} = 23.00^\circ\text{C}$:

Specific Heat at constant pressure ($\overline{c_{p,w}} = 4183.03 \text{ J/kg}^\circ\text{C}$):

$$\text{Absolute: } U_{\overline{c_{p,w}}} = \frac{1}{2} \left| \left(c_{p,w} @ T_{w,b, \max} - c_{p,w} @ T_{w,b, \min} \right) \right| = 1.35 \times 10^{-3} \frac{\text{J}}{\text{kg}^\circ\text{C}}, \quad (\text{A.3.22a})$$

$$\text{Relative: } \frac{U_{\overline{c_{p,w}}}}{\overline{c_{p,w}}} = \frac{1.35 \times 10^{-3}}{4183.03} = 3.23 \times 10^{-7} \approx 3.23 \times 10^{-5} \%. \quad (\text{A.3.22b})$$

Thermal Conductivity ($\overline{k_w} = 0.6038 \text{ W/m}^\circ\text{C}$):

$$\text{Absolute: } U_{\overline{k_w}} = \frac{1}{2} \left| (k_w @ T_{w,b,\max} - k_w @ T_{w,b,\min}) \right| = 8.68 \times 10^{-5} \frac{\text{W}}{\text{m}^\circ\text{C}}, \text{ and} \quad (\text{A.3.23a})$$

$$\text{Relative: } \frac{U_{\overline{k_w}}}{\overline{k_w}} = \frac{8.68 \times 10^{-5}}{0.6038} = 0.0001438 \text{ W/m}^\circ\text{C} \approx 0.014 \%. \quad (\text{A.3.23b})$$

Density ($\overline{\rho_w} = 997.55 \text{ kg/m}^3$):

$$\text{Absolute: } U_{\overline{\rho_w}} = \frac{1}{2} \left| (\rho_w @ T_{w,b,\max} - \rho_w @ T_{w,b,\min}) \right| = 0.012 \frac{\text{kg}}{\text{m}^3}, \text{ and} \quad (\text{A.3.24a})$$

$$\text{Relative: } \frac{U_{\overline{\rho_w}}}{\overline{\rho_w}} = \frac{0.012}{997.55} = 1.203 \times 10^{-5} \approx 0.0012 \%. \quad (\text{A.3.24b})$$

Kinematic Viscosity ($\overline{\nu_w} = 9.338 \times 10^{-7} \text{ m}^2/\text{s}$):

$$\text{Absolute: } U_{\overline{\nu_w}} = \frac{1}{2} \left| (\nu_w @ T_{w,b,\max} - \nu_w @ T_{w,b,\min}) \right| = 1 \times 10^{-9} \frac{\text{m}^2}{\text{s}}, \text{ and} \quad (\text{A.3.25a})$$

$$\text{Relative: } \frac{U_{\overline{\nu_w}}}{\overline{\nu_w}} = \frac{1 \times 10^{-9}}{9.338 \times 10^{-7}} = 1.07 \times 10^{-3} \approx 0.11 \%. \quad (\text{A.3.25b})$$

Prandtl Number ($\overline{\text{Pr}_w} = 6.45$):

$$\text{Absolute: } U_{\overline{\text{Pr}_w}} = \frac{1}{2} \left| (\text{Pr}_w @ T_{w,b,\max} - \text{Pr}_w @ T_{w,b,\min}) \right| = 8.48 \times 10^{-3}, \text{ and} \quad (\text{A.3.26a})$$

$$\text{Relative: } \frac{U_{\overline{\text{Pr}_w}}}{\overline{\text{Pr}_w}} = \frac{8.48 \times 10^{-3}}{6.45} = 1.31 \times 10^{-3} \approx 0.13 \%. \quad (\text{A.3.26b})$$

A.4. Propagation of Uncertainties from Independent to Basic Dependent Parameters

The uncertainties of the basic independent parameters, as measured and estimated above, propagate into other dependent parameters (i.e. the basic experimental parameters to current study) according to their corresponding relationships. The uncertainties associated with these dependent parameters are discussed and estimated in the following subsections. The elliptical tubes were drawn from circular tube by pressing to the shape of an axis ratio of 0.3. Although every attention was paid to make each tube a perfect elliptical tube, in reality there might have at least a little variation. To account for this variation, every dimension of each tube was several times measured by a digital caliper and the mean values were used in the analysis. In this view effect of tube shape was not considered in the uncertainty analysis.

A.4.1. Uncertainties in Tube's Basic Dependent Dimensions – ($H = L_t, A_{c,i}, A_{c,o}, P_i, P_o, D_{h,i}, D_{h,o}, A_{s,i},$ or $A_{s,o}$):

The dimensions of the dependent parameters of the tubes such as the total length, cross-sectional area, perimeter, hydraulic diameter, and the surface area were calculated from their functional relationship with that of the above measured basic independent dimensions. The uncertainties associated with the mean values of these dimensions were estimated also from the same functional relationship as stepped below.

Uncertainty in the total Length of the elliptical tubes ($H = L_t$):

The total length of the tubes, excluding square bends at both ends, was calculated as, the numbers of tubes in the array times the length of each tube in the array. This total

length was used in the experimental analysis. For 18 numbers of tubes, the mean tube length was,

$$\bar{H} = \bar{L}_t = 18\bar{L} = 18 \times (302.73 \times 10^{-3}) \text{ m} = 5.45 \text{ m}. \quad (\text{A.4.1})$$

The associated uncertainty was estimated as,

$$U_{\bar{H}} = U_{\bar{L}_t} = \sqrt{\left(\frac{\partial \bar{L}_t}{\partial \bar{L}} U_{\bar{L}}\right)^2} = \frac{\partial \bar{L}_t}{\partial \bar{L}} U_{\bar{L}}, \quad (\text{A.4.2a})$$

where, from Eq. (A.4.1), $\frac{\partial \bar{L}_t}{\partial \bar{L}} = 18$, and from Table A.2.2, $U_{\bar{L}} = 64.63 \times 10^{-5} \text{ m}$.

The absolute uncertainty is thus,

$$\therefore U_{\bar{H}} = U_{\bar{L}_t} = 18 \times (64.63 \times 10^{-5}) \text{ m} = 11.63 \times 10^{-3} \text{ m}, \quad (\text{A.4.2b})$$

and the relative uncertainty is

$$\frac{U_{\bar{L}_t}}{\bar{L}_t} = \frac{11.63 \times 10^{-3}}{5.45} = 2.13 \times 10^{-3}, \text{ giving } U_{\bar{L}_t}(\%) = (2.13 \times 10^{-3}) \times 100 = 0.21\%. \quad (\text{A.4.2c})$$

Uncertainty in the Inner-side Cross-sectional Area of the elliptical tubes ($H = A_{c,i}$):

The mean inner cross-sectional area of the elliptical tube was calculated to be,

$$\bar{H} = \bar{A}_{c,i} = \pi \bar{a}_i \bar{b}_i = \pi \times (14.91 \times 10^{-3}) \times (3.925 \times 10^{-3}) = 1.8385 \times 10^{-4} \text{ m}^2, \quad (\text{A.4.3})$$

where, \bar{a}_i and \bar{b}_i are the mean inner major and minor axis lengths of the tubes the values of which are tabulated in Table A.2.2.

The overall absolute uncertainty associated with this inner cross-sectional area was estimated as,

$$U_{\overline{H}} = U_{\overline{A_{c,i}}} = \sqrt{\left(\frac{\partial \overline{A_{c,i}}}{\partial a_i} U_{\overline{a_i}}\right)^2 + \left(\frac{\partial \overline{A_{c,i}}}{\partial b_i} U_{\overline{b_i}}\right)^2}, \quad (\text{A.4.4})$$

where, the partial derivatives and their magnitudes were derived from Eq. (A.4.3) as,

$$\frac{\partial \overline{A_{c,i}}}{\partial a_i} = \pi \overline{b_i} = 0.012345 \text{ m} \quad \text{and} \quad \frac{\partial \overline{A_{c,i}}}{\partial b_i} = \pi \overline{a_i} = 0.04684 \text{ m}.$$

Now the absolute uncertainty was found from Eq. (A.4.4) to be,

$$\begin{aligned} U_{\overline{H}} = U_{\overline{A_{c,i}}} &= \sqrt{\left(\pi \overline{b_i} U_{\overline{a_i}}\right)^2 + \left(\pi \overline{a_i} U_{\overline{b_i}}\right)^2} \\ &= \sqrt{\left((0.012345)(5.58 \times 10^{-5})\right)^2 + \left((0.04684)(3.92 \times 10^{-5})\right)^2} = 1.961 \times 10^{-6} \text{ m}^2. \end{aligned}$$

The overall relative uncertainty was calculated as,

$$\frac{U_{\overline{H}}}{\overline{H}} = \frac{U_{\overline{A_{c,i}}}}{\overline{A_{c,i}}} = \sqrt{\left(\frac{\pi \overline{b_i} U_{\overline{a_i}}}{\pi \overline{a_i} \overline{b_i}}\right)^2 + \left(\frac{\pi \overline{a_i} U_{\overline{b_i}}}{\pi \overline{a_i} \overline{b_i}}\right)^2} = \sqrt{\left(\frac{U_{\overline{a_i}}}{\overline{a_i}}\right)^2 + \left(\frac{U_{\overline{b_i}}}{\overline{b_i}}\right)^2}, \quad (\text{A.4.5})$$

which, after using values from Table A.2.2, gave uncertainty in percentage form as,

$$\frac{U_{\overline{H}}}{\overline{H}} (\%) = \frac{U_{\overline{A_{c,i}}}}{\overline{A_{c,i}}} (\%) = \sqrt{\left(\frac{5.58 \times 10^{-5}}{14.91 \times 10^{-3}}\right)^2 + \left(\frac{6.12 \times 10^{-5}}{3.92 \times 10^{-3}}\right)^2} \times 100 \approx 1.61 \%.$$

Uncertainty in the Outer-side Cross-sectional Area of the elliptical tubes ($H = A_{c,o}$):

The mean outer cross-sectional area of the elliptical tube was calculated to be,

$$\overline{H} = \overline{A_{c,o}} = \pi \overline{a_o} \overline{b_o} = \pi \times (15.82 \times 10^{-3}) \times (4.81 \times 10^{-3}) = 2.39 \times 10^{-4} \text{ m}^2, \quad (\text{A.4.6})$$

where, \bar{a}_o and \bar{b}_o are the mean outer major and minor axis lengths of the tubes. The values are tabulated in Table A.2.2. The following partial derivatives and their magnitudes, necessary for uncertainty analysis, were derived from Eq. (A.4.6) as,

$$\frac{\partial \bar{A}_{c,o}}{\partial a_o} = \pi \bar{b}_o = 0.01511 \text{ m} \quad \text{and} \quad \frac{\partial \bar{A}_{c,o}}{\partial b_o} = \pi \bar{a}_o = 0.0497 \text{ m}.$$

The overall absolute uncertainty associated with this outer cross-sectional area was estimated like the same way as for the inner-side ($\bar{A}_{c,i}$) estimated in previous section. The calculations are as follows:

$$\begin{aligned} U_{\bar{H}} = U_{\bar{A}_{c,o}} &= \sqrt{\left(\frac{\partial \bar{A}_{c,o}}{\partial a_o} U_{a_o}\right)^2 + \left(\frac{\partial \bar{A}_{c,o}}{\partial b_o} U_{b_o}\right)^2} = \sqrt{(\pi \bar{b}_o U_{a_o})^2 + (\pi \bar{a}_o U_{b_o})^2} \quad (\text{A.4.7}) \\ &= \sqrt{((0.01511)(3.71 \times 10^{-5}))^2 + ((0.0497)(3.65 \times 10^{-5}))^2} = 1.899 \times 10^{-6} \text{ m}^2. \end{aligned}$$

The overall relative uncertainty (in % form) was calculated as,

$$\frac{U_{\bar{A}_{c,o}}}{\bar{A}_{c,o}} = \sqrt{\left(\frac{U_{a_o}}{a_o}\right)^2 + \left(\frac{U_{b_o}}{b_o}\right)^2} = \sqrt{\left(\frac{3.71 \times 10^{-5}}{15.82 \times 10^{-3}}\right)^2 + \left(\frac{3.65 \times 10^{-5}}{4.81 \times 10^{-3}}\right)^2} \times 100 \approx 0.80\%. \quad (\text{A.4.8})$$

Uncertainty in the Inner Perimeter/Circumference of the elliptical tubes ($H = P_i$):

The mean inner-side perimeter of the elliptical tube was calculated to be,

$$\bar{H} = \bar{P}_i = 2\pi \sqrt{\frac{(\bar{a}_i)^2 + (\bar{b}_i)^2}{2}} = 6.494 \times 10^{-2} \text{ m}. \quad (\text{A.4.9})$$

The overall absolute uncertainty associated with this perimeter was estimated as,

$$U_{\bar{H}} = U_{\bar{P}_i} = \sqrt{\left(\frac{\partial \bar{P}_i}{\partial a_i} U_{\bar{a}_i}\right)^2 + \left(\frac{\partial \bar{P}_i}{\partial b_i} U_{\bar{b}_i}\right)^2}, \quad (\text{A.4.10})$$

where, the partial derivatives and their magnitudes were derived from Eq. (A.4.9) as,

$$\frac{\partial \bar{P}_i}{\partial a_i} = \frac{\sqrt{2} \pi \bar{a}_i}{\sqrt{(\bar{a}_i)^2 + (\bar{b}_i)^2}} = 4.2969 \quad \text{and} \quad \frac{\partial \bar{P}_i}{\partial b_i} = \frac{\sqrt{2} \pi \bar{b}_i}{\sqrt{(\bar{a}_i)^2 + (\bar{b}_i)^2}} = 1.1297.$$

Now the absolute uncertainty was found from Eq. (A.4.10) to be,

$$U_{\bar{H}} = U_{\bar{P}_i} = \sqrt{\left((4.29686)(5.58 \times 10^{-5})\right)^2 + \left((1.12969)(3.92 \times 10^{-5})\right)^2} = 2.438 \times 10^{-4} \text{ m.}$$

The overall relative uncertainty (in % form) was calculated as,

$$\begin{aligned} \frac{U_{\bar{H}}}{\bar{H}} (\%) &= \frac{U_{\bar{P}_i}}{\bar{P}_i} (\%) = \frac{1}{(\bar{a}_i)^2 + (\bar{b}_i)^2} \sqrt{\left(\frac{U_{\bar{a}_i}}{1/\bar{a}_i}\right)^2 + \left(\frac{U_{\bar{b}_i}}{1/\bar{b}_i}\right)^2} \times 100, \quad (\text{A.4.11}) \\ &= \frac{1}{\left((14.91 \times 10^{-3})^2 + (3.92 \times 10^{-3})^2\right)} \sqrt{\left(\frac{5.58 \times 10^{-5}}{1/14.91 \times 10^{-3}}\right)^2 + \left(\frac{6.12 \times 10^{-5}}{1/3.92 \times 10^{-3}}\right)^2} \times 100 \approx \pm 0.38\%. \end{aligned}$$

Uncertainty in the Outer Perimeter/Circumference of the elliptical tubes ($H = P_o$):

The mean inner-side perimeter of the elliptical tube was calculated to be,

$$\bar{H} = \bar{P}_o = 2\pi \sqrt{\frac{\bar{a}_o^2 + \bar{b}_o^2}{2}} = 2\pi \sqrt{\frac{(15.82 \times 10^{-3})^2 + (4.81 \times 10^{-3})^2}{2}} = 6.97 \times 10^{-2} \text{ m.} \quad (\text{A.4.12})$$

The following partial derivatives and their magnitudes, necessary for uncertainty analysis, were derived from Eq. (A.4.12) as,

$$\frac{\partial \bar{P}_o}{\partial a_o} = \frac{\sqrt{2} \pi a_o}{\sqrt{(a_o)^2 + (b_o)^2}} = 4.251 \quad \text{and} \quad \frac{\partial \bar{P}_o}{\partial b_o} = \frac{\sqrt{2} \pi b_o}{\sqrt{(a_o)^2 + (b_o)^2}} = 1.292 .$$

The overall absolute uncertainty associated with this outer perimeter was estimated in the same way as for the inner perimeter (\bar{P}_i) estimated above. The calculations are as follows:

$$U_{\bar{H}} = U_{\bar{P}_o} = \sqrt{\left(\frac{\partial \bar{P}_o}{\partial a_o} U_{a_o}\right)^2 + \left(\frac{\partial \bar{P}_o}{\partial b_o} U_{b_o}\right)^2}, \quad \text{using Table A.2.2,} \quad (\text{A.4.13})$$

$$= \sqrt{\left((4.251)(3.71 \times 10^{-5})\right)^2 + \left((1.292)(3.65 \times 10^{-5})\right)^2} = 1.66 \times 10^{-4} \text{ m} .$$

The overall relative uncertainty (in % form) was calculated as,

$$\frac{U_{\bar{H}}}{\bar{H}} (\%) = \frac{U_{\bar{P}_o}}{\bar{P}_o} (\%) = \frac{1}{(a_o)^2 + (b_o)^2} \sqrt{\left(\frac{U_{a_o}}{1/a_o}\right)^2 + \left(\frac{U_{b_o}}{1/b_o}\right)^2} \times 100, \quad (\text{A.4.14})$$

$$= \frac{1}{\left((15.82 \times 10^{-3})^2 + (4.81 \times 10^{-3})^2\right)} \sqrt{\left(\frac{3.71 \times 10^{-5}}{1/15.82 \times 10^{-3}}\right)^2 + \left(\frac{3.65 \times 10^{-5}}{1/4.81 \times 10^{-3}}\right)^2} \times 100 \approx 0.24\% .$$

Uncertainty in the Inner-side Hydraulic Diameter of the elliptical tubes ($H = D_{h,i}$):

From the definition, the mean inner-side hydraulic diameter of the elliptical tube was calculated to be,

$$\bar{H} = \bar{D}_{h,i} = \frac{4 \bar{A}_{c,i}}{\bar{P}_i} = \frac{4 \times (1.8385 \times 10^{-4})}{6.495 \times 10^{-2}} = 1.132 \times 10^{-2} \text{ m} . \quad (\text{A.4.15})$$

The overall absolute uncertainty associated with this parameter was estimated as,

$$U_{\overline{H}} = U_{\overline{D_{h,i}}} = \sqrt{\left(\frac{\partial \overline{D_{h,i}}}{\partial \overline{A_{c,i}}} U_{\overline{A_{c,i}}}\right)^2 + \left(\frac{\partial \overline{D_{h,i}}}{\partial \overline{P_i}} U_{\overline{P_i}}\right)^2}, \quad (\text{A.4.16})$$

where, the partial derivatives and their magnitudes were derived from Eq. (A.4.16) as,

$$\frac{\partial \overline{D_{h,i}}}{\partial \overline{A_{c,i}}} = \frac{4}{\overline{P_i}} = \frac{4}{6.4949 \times 10^{-2}} = 61.586 \text{ m}^{-1} \quad \text{and} \quad \frac{\partial \overline{D_{h,i}}}{\partial \overline{P_i}} = -\frac{4\overline{A_{c,i}}}{(\overline{P_i})^2} = -0.1743.$$

Now the absolute uncertainty was found from Eqs. (A.4.4) and (A.4.10) to be,

$$U_{\overline{H}} = U_{\overline{D_{h,i}}} = \sqrt{\left((61.586)(1.961 \times 10^{-6})\right)^2 + \left(-0.17433(2.4382 \times 10^{-4})\right)^2} = 1.28 \times 10^{-4} \text{ m}.$$

The overall relative uncertainty (in % form) was calculated as,

$$\begin{aligned} \frac{U_{\overline{H}}}{\overline{H}} (\%) &= \frac{U_{\overline{D_{h,i}}}}{\overline{D_{h,i}}} (\%) = \sqrt{\left(\frac{U_{\overline{A_{c,i}}}}{\overline{A_{c,i}}}\right)^2 + \left(\frac{U_{\overline{P_i}}}{\overline{P_i}}\right)^2} \times 100, \quad (\text{A.4.17}) \\ &= \sqrt{\left(\frac{1.961 \times 10^{-6}}{1.8385 \times 10^{-4}}\right)^2 + \left(\frac{2.4382 \times 10^{-4}}{6.4949 \times 10^{-2}}\right)^2} \times 100 \approx 1.13 \%. \end{aligned}$$

Uncertainty in the Outer-side Hydraulic Diameter of the elliptical tubes ($H = D_{h,o}$):

From the definition, the mean outer-side hydraulic diameter of the elliptical tube was calculated to be,

$$\overline{H} = \overline{D_{h,o}} = \frac{4\overline{A_{c,o}}}{\overline{P_o}} = \frac{4 \times (2.3905 \times 10^{-4})}{6.971 \times 10^{-2}} = 1.372 \times 10^{-2} \text{ m}. \quad (\text{A.4.18})$$

The following partial derivatives and their magnitudes, necessary for uncertainty analysis, were derived from Eq. (A.4.18) as,

$$\frac{\partial \overline{D_{h,o}}}{\partial \overline{A_{c,o}}} = \frac{4}{\overline{P_o}} = \frac{4}{6.971 \times 10^{-2}} = 57.381 \text{ m}^{-1} \quad \text{and} \quad \frac{\partial \overline{D_{h,o}}}{\partial \overline{P_o}} = -\frac{4\overline{A_{c,o}}}{(\overline{P_o})^2} = -0.19682 .$$

The overall absolute uncertainty associated with this outer hydraulic diameter was estimated in the same way as for the inner hydraulic diameter ($\overline{D_{h,i}}$) estimated above.

The calculations are as follows, where Eqs. (A.4.7) and (A.4.12) were used)

$$\begin{aligned} U_{\overline{H}} = U_{\overline{D_{h,o}}} &= \sqrt{\left(\frac{\partial \overline{D_{h,o}}}{\partial \overline{A_{c,o}}} U_{\overline{A_{c,o}}}\right)^2 + \left(\frac{\partial \overline{D_{h,o}}}{\partial \overline{P_o}} U_{\overline{P_o}}\right)^2} , \quad (\text{A.4.19}) \\ &= \sqrt{\left((57.381)(1.899 \times 10^{-6})\right)^2 + \left((-0.1968)(1.6603 \times 10^{-4})\right)^2} = 1.14 \times 10^{-4} \text{ m} . \end{aligned}$$

The overall relative uncertainty (in % form) was calculated as,

$$\begin{aligned} \frac{U_{\overline{H}}}{\overline{H}} (\%) &= \frac{U_{\overline{D_{h,o}}}}{\overline{D_{h,o}}} (\%) = \sqrt{\left(\frac{U_{\overline{A_{c,o}}}}{\overline{A_{c,o}}}\right)^2 + \left(\frac{U_{\overline{P_o}}}{\overline{P_o}}\right)^2} \times 100 , \quad (\text{A.4.20}) \\ &= \sqrt{\left(\frac{1.8987 \times 10^{-6}}{2.3905 \times 10^{-4}}\right)^2 + \left(\frac{1.6603 \times 10^{-4}}{6.971 \times 10^{-2}}\right)^2} \times 100 \approx 0.83 \% . \end{aligned}$$

Uncertainty in the Inner-side Surface Area of the elliptical tubes ($H = A_{s,i}$):

From the definition, the mean inner-side surface area of the elliptical tube was calculated to be,

$$\overline{H} = \overline{A_{s,i}} = \overline{P_i} \overline{L_t} = (6.495 \times 10^{-2})(5.45) = 0.35398 \text{ m}^2 . \quad (\text{A.4.21})$$

The following partial derivatives and their magnitudes, necessary for uncertainty analysis, were derived from Eq. (A.4.21) as,

$$\frac{\partial \overline{A_{s,i}}}{\partial P_i} = \overline{L_t} = 5.45 \text{ m} \quad \text{and} \quad \frac{\partial \overline{A_{s,i}}}{\partial L_t} = \overline{P_i} = 6.495 \times 10^{-2} \text{ m}.$$

The overall absolute uncertainty in this inner surface area was estimated as,

$$\begin{aligned} U_{\overline{H}} = U_{\overline{A_{s,i}}} &= \sqrt{\left(\frac{\partial \overline{A_{s,i}}}{\partial P_i} U_{\overline{P_i}}\right)^2 + \left(\frac{\partial \overline{A_{s,i}}}{\partial L_t} U_{\overline{L_t}}\right)^2}, \quad (\text{A.4.22}) \\ &= \sqrt{\left((5.45)(2.4382 \times 10^{-4})\right)^2 + \left((6.495 \times 10^{-2})(11.6334 \times 10^{-3})\right)^2} = 1.529 \times 10^{-3} \text{ m}. \end{aligned}$$

The overall relative uncertainty (in % form) was calculated as,

$$\begin{aligned} \frac{U_{\overline{H}}}{\overline{H}} (\%) &= \frac{U_{\overline{A_{s,i}}}}{\overline{A_{s,i}}} (\%) = \sqrt{\left(\frac{U_{\overline{P_i}}}{\overline{P_i}}\right)^2 + \left(\frac{U_{\overline{L_t}}}{\overline{L_t}}\right)^2} \times 100, \quad (\text{A.4.23}) \\ &= \sqrt{\left(\frac{2.4382 \times 10^{-4}}{6.495 \times 10^{-2}}\right)^2 + \left(\frac{11.6334 \times 10^{-3}}{5.45}\right)^2} \times 100 \approx 0.43 \%. \end{aligned}$$

Uncertainty in the Outer-side Surface Area of the elliptical tubes ($H = A_{s,o}$):

From the definition, the mean outer-side surface area of the elliptical tube was calculated to be,

$$\overline{H} = \overline{A_{s,o}} = \overline{P_o} \overline{L_t} = (6.971 \times 10^{-2})(5.45) = 0.37992 \text{ m}^2. \quad (\text{A.4.24})$$

The following partial derivatives and their magnitudes, necessary for uncertainty analysis, were derived from Eq. (A.4.24) as,

$$\frac{\partial \overline{A_{s,o}}}{\partial P_o} = \overline{L_t} = 5.45 \text{ m} \quad \text{and} \quad \frac{\partial \overline{A_{s,o}}}{\partial L_t} = \overline{P_o} = 6.971 \times 10^{-2} \text{ m}.$$

The overall absolute uncertainty associated with this outer surface area was estimated as,

$$U_{\overline{H}} = U_{\overline{A_{s,o}}} = \sqrt{\left(\frac{\partial \overline{A_{s,o}}}{\partial P_o} U_{\overline{P_o}}\right)^2 + \left(\frac{\partial \overline{A_{s,o}}}{\partial L_t} U_{\overline{L_t}}\right)^2}, \quad (\text{A.4.25})$$

$$= \sqrt{\left((5.45)(1.6603 \times 10^{-4})\right)^2 + \left((6.971 \times 10^{-2})(11.6334 \times 10^{-3})\right)^2} = 1.215 \times 10^{-3} \text{ m}.$$

The overall relative uncertainty (in % form) was calculated as,

$$\frac{U_{\overline{H}}}{\overline{H}} (\%) = \frac{U_{\overline{A_{s,o}}}}{\overline{A_{s,o}}} (\%) = \sqrt{\left(\frac{U_{\overline{P_o}}}{\overline{P_o}}\right)^2 + \left(\frac{U_{\overline{L_t}}}{\overline{L_t}}\right)^2} \times 100, \quad (\text{A.4.26})$$

$$= \sqrt{\left(\frac{1.6603 \times 10^{-4}}{6.971 \times 10^{-2}}\right)^2 + \left(\frac{11.6334 \times 10^{-3}}{5.45}\right)^2} \times 100 \approx 0.32 \%.$$

The overall uncertainties in tubes' dependent dimensions are listed in Table A.4.1.

Table A.4.1 Uncertainties in Tubes' Dependent Dimensions (Calculated Values)

	Tubes' Dependent Dimensional Parameters	Mean Value, \overline{H}	Absolute Uncertainty, $U_{\overline{H}} \times 10^3$	Relative Uncertainty, $\frac{U_{\overline{H}}}{\overline{H}} \times 100$ (%)
	Total length of all tubes together, L_t [m]	5.450000	11.63000	0.21
Inner-side	Cross-sectional area, $A_{c,i}$ [m ²]	0.000184	0.00196	1.07
	Perimeter / Circumference, P_i [m]	0.064949	0.24382	0.38
	Hydraulic diameter, $D_{h,i}$ [m]	0.011322	0.12803	1.13
	Surface area, $A_{s,i}$ [m ²]	0.353980	1.52900	0.43
Outer-side	Cross-sectional area, $A_{c,o}$ [m ²]	0.000239	0.00189	0.80
	Perimeter / Circumference, P_o [m]	0.069710	0.16603	0.24
	Hydraulic diameter, $D_{h,o}$ [m]	0.013720	0.11374	0.83
	Surface area, $A_{s,o}$ [m ²]	0.379920	1.21500	0.32

A.4.2. Uncertainty in the Airside Dependent Parameters – ($H = V_a$, \dot{m}_a , Re_a , or q_a):

The flow velocity (V_a), mass flow rate (\dot{m}_a), and the heat transfer rate (q_a) are the basic dependent parameters to this experiment for the airside. The uncertainties associated with these parameters are estimated according to their functional relationship with that of the independent parameters as detailed below.

Uncertainty in the Airside Velocity ($H = V_a$):

The airside velocity, as measured by Pitot static tube in terms of pressure difference, is defined as

$$\overline{H} = \overline{V}_a = \sqrt{\frac{2\Delta p_{\text{pitot}}}{\rho_a}} = \sqrt{2} (\overline{\Delta p_{\text{pitot}}})^{1/2} (\overline{\rho_a})^{-1/2} \text{ m/s} \quad (\text{A.4.27})$$

and its partial derivatives are

$$\frac{\partial \overline{V}_a}{\partial \Delta p_{\text{pitot}}} = \frac{1}{\sqrt{2} \sqrt{\Delta p_{\text{pitot}} \rho_a}} \quad \text{and} \quad \frac{\partial \overline{V}_a}{\partial \rho_a} = -\frac{\sqrt{\Delta p_{\text{pitot}}}}{\sqrt{2} (\rho_a)^{3/2}}. \quad (\text{A.4.28})$$

The uncertainty associated with this velocity was estimated to be

$$U_{\overline{H}} = U_{\overline{V}_a} = \sqrt{\frac{\overline{\Delta p_{\text{pitot}}}}{2\rho_a} \left[\left(\frac{U_{\overline{\Delta p_{\text{pitot}}}}}{\overline{\Delta p_{\text{pitot}}}} \right)^2 + \left(\frac{U_{\overline{\rho_a}}}{\overline{\rho_a}} \right)^2 \right]} \text{ m/s}, \quad (\text{A.4.29a})$$

where the partial derivatives are taken from Eq. (A.4.28) and the uncertainty components;

$U_{\overline{\Delta p_{\text{pitot}}}}$ is taken from Table A.2.2 or Eq. (A.2.18) and $U_{\overline{\rho_a}}$ from Eq. (A.3.1). The

relative uncertainty (in percentage) was estimated to be

$$\frac{U_{\overline{H}}}{\overline{H}} (\%) = \frac{U_{\overline{V_a}}}{\overline{V_a}} (\%) = \frac{1}{2} \sqrt{\left(\frac{U_{\overline{\Delta p_{\text{pitot}}}}}{\overline{\Delta p_{\text{pitot}}}}\right)^2 + \left(\frac{U_{\overline{\rho_a}}}{\overline{\rho_a}}\right)^2} \times 100\% . \quad (\text{A.4.29b})$$

SAMPLE CALCULATION – Example Experimental Data Table A.1.1 ($H = V_a$):

From Table A.1.1: $\overline{\Delta p_{\text{pitot}}} = 48.50 \text{ Pa}$, $\overline{V_a} = 8.92 \text{ m/s}$, $\overline{\rho_a} = 1.2326 \text{ kg/m}^3$. The absolute uncertainty in air velocity is estimated using Eq. (A.4.29a) and taking values from Eq. (A.2.18c) or Table A.2.2 and Eq. (A.3.19b) to be

$$\begin{aligned} U_{\overline{H}} = U_{\overline{V_a}} &= \sqrt{\frac{\overline{\Delta p_{\text{pitot}}}}{2\overline{\rho_a}} \left[\left(\frac{U_{\overline{\Delta p_{\text{pitot}}}}}{\overline{\Delta p_{\text{pitot}}}}\right)^2 + \left(\frac{U_{\overline{\rho_a}}}{\overline{\rho_a}}\right)^2 \right]}, \quad (\text{A.4.29c}) \\ &= \sqrt{\frac{48.50}{2 \times 1.2326} \left[(0.0293)^2 + (2.529 \times 10^{-3})^2 \right]} = 0.13 \text{ m/s}, \end{aligned}$$

and the relative uncertainty, From Eq. (A.4.29b), is estimated to be

$$\frac{U_{\overline{H}}}{\overline{H}} = \frac{U_{\overline{V_a}}}{\overline{V_a}} = \frac{1}{2} \sqrt{(0.0293)^2 + (2.529 \times 10^{-3})^2} = 0.0147 = 1.47\% . \quad (\text{A.4.29d})$$

Uncertainty in the Air Mass Flow Rate ($H = \dot{m}_a$):

The mass flow rate of air through the test section duct is defined as

$$\overline{H} = \overline{\dot{m}_a} = \overline{\rho_a} \overline{A_{\text{duct}}} \overline{V_a} \text{ kg/s}, \quad (\text{A.4.30})$$

and its partial derivatives are

$$\frac{\partial \overline{\dot{m}_a}}{\partial \overline{\rho_a}} = \overline{A_{\text{duct}}} \overline{V_a}, \quad \frac{\partial \overline{\dot{m}_a}}{\partial \overline{A_{\text{duct}}}} = \overline{\rho_a} \overline{V_a}, \quad \text{and} \quad \frac{\partial \overline{\dot{m}_a}}{\partial \overline{V_a}} = \overline{\rho_a} \overline{A_{\text{duct}}} . \quad (\text{A.4.31})$$

The effect of the boundary layer around the inside wall of the test section duct was not taken into account. So, a conservative estimate of uncertainty associated with this mass flow rate was made as

$$U_{\overline{H}} = U_{\overline{\dot{m}_a}} = \sqrt{\left(\frac{\partial \overline{\dot{m}_a}}{\partial \overline{\rho_a}} U_{\overline{\rho_a}}\right)^2 + \left(\frac{\partial \overline{\dot{m}_a}}{\partial \overline{A_{\text{duct}}}} U_{\overline{A_{\text{duct}}}}\right)^2 + \left(\frac{\partial \overline{\dot{m}_a}}{\partial \overline{V_a}} U_{\overline{V_a}}\right)^2} \text{ kg/s}, \quad (\text{A.4.32a})$$

where the partial derivatives are taken from Eq. (A.4.31) and the uncertainty components; $U_{\overline{\rho_a}}$ is obtained using Eq. (A.3.1), $U_{\overline{V_a}}$ is taken from Eq. (A.4.29a), and $U_{\overline{A_{\text{duct}}}}$ is taken to be zero because of the fixed cross-sectional area of the duct. The relative uncertainty (in percentage) was estimated to be

$$\frac{U_{\overline{H}}}{\overline{H}} (\%) = \frac{U_{\overline{\dot{m}_a}}}{\overline{\dot{m}_a}} (\%) = \sqrt{\left(\frac{U_{\overline{\rho_a}}}{\overline{\rho_a}}\right)^2 + \left(\frac{U_{\overline{V_a}}}{\overline{V_a}}\right)^2} \times 100\%. \quad (\text{A.4.32b})$$

SAMPLE CALCULATION – Example Experimental Data Table A.1.1 ($\overline{H} = \overline{\dot{m}_a}$):

From Table A.1.1: $\overline{\dot{m}_a} = 1.011 \text{ kg/s}$, $\overline{V_a} = 8.92 \text{ m/s}$, and $\overline{\rho_a} = 1.2326 \text{ kg/m}^3$.

From Eq. (A.3.19a): $U_{\overline{\rho_a}} = 3.1177 \times 10^{-3} \text{ kg/m}^3$, and from Eq. (A.4.29c):

$U_{\overline{V_a}} = 0.13 \text{ m/s}$. The cross-sectional area of the test section duct is: $\overline{A_{\text{duct}}} = 0.09 \text{ m}^2$. The

absolute uncertainty in air mass flow is estimated using Eqs. (A.4.31) and (A.4.32a) as

$$U_{\overline{H}} = U_{\overline{\dot{m}_a}} = \sqrt{\left(0.09 \times 8.92 \times 3.118 \times 10^{-4}\right)^2 + \left(0.09 \times 1.233\right) \times 0.13^2} = 0.0146 \text{ kg/s}, \quad (\text{A.4.32c})$$

and the relative uncertainty, from Eq. (A.4.32b), is estimated to be

$$\frac{U_{\bar{H}}}{\bar{H}} = \frac{U_{\bar{\dot{m}}_a}}{\bar{\dot{m}}_a} = \sqrt{(1.92 \times 10^{-4})^2 + (0.0147)^2} = 0.0147 \approx 1.47 \% . \quad (\text{A.4.32d})$$

Uncertainty in the Airside Reynolds number ($H = \text{Re}_a$):

The airside Reynolds number, based on the streamwise major axis length of the elliptical tube, is defined as

$$\bar{H} = \overline{\text{Re}}_a = \frac{\overline{\rho}_a \overline{V}_a (2\overline{a}_o)}{\overline{\mu}_a} = \frac{\overline{V}_a (2\overline{a}_o)}{\overline{\nu}_a}, \quad (\text{A.4.33})$$

and its partial derivatives are

$$\frac{\partial \overline{\text{Re}}_a}{\partial \overline{V}_a} = \frac{2\overline{a}_o}{\overline{\nu}_a}, \quad \frac{\partial \overline{\text{Re}}_a}{\partial (2\overline{a}_o)} = \frac{\overline{V}_a}{\overline{\nu}_a}, \quad \text{and} \quad \frac{\partial \overline{\text{Re}}_a}{\partial \overline{\nu}_a} = -\frac{\overline{V}_a (2\overline{a}_o)}{(\overline{\nu}_a)^2}. \quad (\text{A.4.34})$$

The uncertainty associated with Reynolds number was estimated to be

$$U_{\bar{H}} = U_{\overline{\text{Re}}_a} = \sqrt{\left(\frac{\partial \overline{\text{Re}}_a}{\partial \overline{V}_a} U_{\overline{V}_a} \right)^2 + \left(\frac{\partial \overline{\text{Re}}_a}{\partial (2\overline{a}_o)} U_{2\overline{a}_o} \right)^2 + \left(\frac{\partial \overline{\text{Re}}_a}{\partial \overline{\nu}_a} U_{\overline{\nu}_a} \right)^2}, \quad (\text{A.4.35a})$$

where the partial derivatives are taken from Eq. (A.4.34) and the uncertainty components;

$U_{\overline{V}_a}$ from Eq. (A.4.29a), $U_{2\overline{a}_o}$ from Table A.2.2, and $U_{\overline{\nu}_a}$ using Eq. (A.3.1). The

relative uncertainty (in percentage) was estimated to be

$$\frac{U_{\bar{H}}}{\bar{H}} (\%) = \frac{U_{\overline{\text{Re}}_a}}{\overline{\text{Re}}_a} (\%) = \sqrt{\left(\frac{U_{\overline{V}_a}}{\overline{V}_a} \right)^2 + \left(\frac{U_{2\overline{a}_o}}{2\overline{a}_o} \right)^2 + \left(\frac{U_{\overline{\nu}_a}}{\overline{\nu}_a} \right)^2} \times 100\% . \quad (\text{A.4.35b})$$

SAMPLE CALCULATION – Example Experimental Data Table A.1.1 ($H = \text{Re}_a$):

From Table A.1.1: $\overline{\text{Re}}_a = 19229$, $\overline{V}_a = 8.92 \text{ m/s}$, and $\overline{v}_a = 1.455 \times 10^{-5} \text{ m}^2/\text{s}$.

From Eq. (A.4.29c): $U_{\overline{V}_a} = 0.13 \text{ m/s}$, from Eq. (A.3.20a): $U_{\overline{v}_a} = 5.0 \times 10^{-9} \text{ m}^2/\text{s}$, and

from Table A.2.2: $\overline{2a}_o = 31.64 \times 10^{-3} \text{ m}$, and $U_{\overline{2a}_o} = 5.57 \times 10^{-5} \text{ m}$. The absolute

uncertainty in airside Reynolds number is estimated using Eqs. (A.4.34) and (A.4.35a) as

$$U_{\overline{H}} = U_{\overline{\text{Re}}_a} = \sqrt{\left(\frac{31.64 \times 10^{-3}}{1.455 \times 10^{-5}} \times 0.13\right)^2 + \left(\frac{8.92}{1.455 \times 10^{-5}} \times (5.57 \times 10^{-5})\right)^2} + \sqrt{\left(\frac{8.92 \times (31.64 \times 10^{-3})}{(1.455 \times 10^{-5})^2} \times (6.5 \times 10^{-8})\right)^2} = 284.83 \quad (\text{A.4.35c})$$

and the relative uncertainty, from Eq. (A.4.35b), is estimated to be

$$\frac{U_{\overline{H}}}{\overline{H}} = \frac{U_{\overline{\text{Re}}_a}}{\overline{\text{Re}}_a} = \sqrt{(0.0149)^2 + (1.8 \times 10^{-3})^2 + (4.468 \times 10^{-3})^2} = 0.0157 \approx 1.57\% \quad (\text{A.4.35d})$$

Uncertainty in the Airside Heat Transfer Rate ($H = q_a$):

The heat transfer rate based on airside analysis is defined by

$$\overline{H} = \overline{q}_a = \overline{\dot{m}}_a \overline{c}_{p,a} \left| \overline{T}_{a,i} - \overline{T}_{a,o} \right| = \overline{\dot{m}}_a \overline{c}_{p,a} \left| \overline{\Delta T}_a \right| \text{ W} \quad (\text{A.4.36})$$

and its partial derivatives are

$$\frac{\partial \overline{q}_a}{\partial \overline{\dot{m}}_a} = \overline{c}_{p,a} \overline{\Delta T}_a, \quad \frac{\partial \overline{q}_a}{\partial \overline{c}_{p,a}} = \overline{\dot{m}}_a \overline{\Delta T}_a, \quad \text{and} \quad \frac{\partial \overline{q}_a}{\partial \overline{\Delta T}_a} = \overline{\dot{m}}_a \overline{c}_{p,a}. \quad (\text{A.4.37})$$

The uncertainty associated with this heat transfer rate was estimated to be

$$U_{\overline{H}} = U_{\overline{q_a}} = \sqrt{\left(\frac{\partial \overline{q_a}}{\partial \overline{m_a}} U_{\overline{m_a}}\right)^2 + \left(\frac{\partial \overline{q_a}}{\partial \overline{c_{p,a}}} U_{\overline{c_{p,a}}}\right)^2 + \left(\frac{\partial \overline{q_a}}{\partial \overline{\Delta T_a}} U_{\overline{\Delta T_a}}\right)^2} \text{ W}, \quad (\text{A.4.38a})$$

where the partial derivatives are taken from Eq. (A.4.37) and the uncertainty components;

$U_{\overline{m_a}}$ is taken from Eq. (A.4.32a), $U_{\overline{c_{p,a}}}$ using Eq. (A.3.1), and $U_{\overline{\Delta T_a}}$ from Eq. (A.2.30)

or from Table A.2.3. The relative uncertainty (in percentage) was estimated to be

$$\frac{U_{\overline{H}}}{\overline{H}} (\%) = \frac{U_{\overline{q_a}}}{\overline{q_a}} (\%) = \sqrt{\left(\frac{U_{\overline{m_a}}}{\overline{m_a}}\right)^2 + \left(\frac{U_{\overline{c_{p,a}}}}{\overline{c_{p,a}}}\right)^2 + \left(\frac{U_{\overline{\Delta T_a}}}{\overline{\Delta T_a}}\right)^2} \times 100\%. \quad (\text{A.4.38b})$$

SAMPLE CALCULATION – Example Experimental Data Table A.1.1 ($H = \overline{q_a}$):

From Table A.1.1: $\overline{q_a} = 559.40 \text{ W}$, $\overline{m_a} = 1.011 \text{ kg/s}$, $\overline{c_{p,a}} = 1006.55 \text{ J/kg}\cdot^\circ\text{C}$, and

$\overline{\Delta T_a} = \overline{T_{a,o}} - \overline{T_{a,i}} = 0.55^\circ\text{C}$. From Eq. (A.4.32c): $U_{\overline{m_a}} = 0.0146 \text{ kg/s}$, from Eq. (A.3.17a):

$U_{\overline{c_{p,a}}} = 0.01074 \text{ J/kg}\cdot^\circ\text{C}$, and from Table A.2.3: $U_{\overline{\Delta T_a}} = 0.10^\circ\text{C}$. The absolute

uncertainty in airside Heat transfer rate is estimated using Eqs. (A.4.37) and (A.4.38a) as

$$U_{\overline{H}} = U_{\overline{q_a}} = \sqrt{(1006.55 \times 0.55 \times 0.0146)^2 + (1.011 \times 0.55 \times (0.01074))^2 + (1.011 \times 1006.55 \times 0.10)^2} = 102.08 \text{ W} \quad (\text{A.4.38c})$$

and the relative uncertainty, from Eq. (A.4.38b), is estimated to be

$$\frac{U_{\overline{H}}}{\overline{H}} = \frac{U_{\overline{q_a}}}{\overline{q_a}} = \sqrt{(0.0149)^2 + (1.07 \times 10^{-5})^2 + \left(\frac{0.10}{0.55}\right)^2} = 0.1824 \approx 18.24\%. \quad (\text{A.4.38d})$$

A.4.3. Uncertainty in the Waterside Dependent Parameters – ($H = \dot{m}_w, V_w, Re_w, q_w$):

The mass flow rate (\dot{m}_w), flow velocity (V_w), and the heat transfer rate (q_w) are the basic dependent parameters to this experiment for the waterside. The uncertainties associated with these parameters are estimated according to their functional relationship with that of the independent parameters as detailed below.

Uncertainty in the Water Mass Flow Rate ($H = \dot{m}_w$):

The mass flow rate of water inside the elliptical tubes is defined by

$$\overline{H} = \overline{\dot{m}_w} = \frac{\overline{m_w}}{t} \text{ kg/s,} \quad (\text{A.4.39})$$

and its partial derivatives are

$$\frac{\partial \overline{\dot{m}_w}}{\partial m_w} = \frac{1}{t}, \text{ and } \frac{\partial \overline{\dot{m}_w}}{\partial t} = -\frac{\overline{m_w}}{(t)^2}. \quad (\text{A.4.40})$$

The uncertainty associated with this mass flow rate was estimated to be

$$U_{\overline{H}} = U_{\overline{\dot{m}_w}} = \sqrt{\left(\frac{\partial \overline{\dot{m}_w}}{\partial m_w} U_{m_w} \right)^2 + \left(\frac{\partial \overline{\dot{m}_w}}{\partial t} U_t \right)^2} \text{ kg/s,} \quad (\text{A.4.41a})$$

where the partial derivatives are taken from Eq. (A.4.40) and the uncertainty components;

U_{m_w} and U_t are obtained from Table A.2.3 or Eqs. (A.2.36) and (A.2.33) respectively.

The relative uncertainty (in percentage) was estimated to be

$$\frac{U_{\overline{H}}}{\overline{H}} (\%) = \frac{U_{\overline{\dot{m}_w}}}{\overline{\dot{m}_w}} (\%) = \sqrt{\left(\frac{U_{m_w}}{m_w} \right)^2 + \left(\frac{U_t}{t} \right)^2} \times 100\%. \quad (\text{A.4.41b})$$

SAMPLE CALCULATION – Example Experimental Data Table A.1.1 ($H = \dot{m}_w$):

From Table A.1.1: $\overline{\dot{m}_w} = 0.0641 \text{ kg/s}$, $\bar{t} = 293.10 \text{ sec}$, and $\overline{m_w} = 18.7674 \text{ kg}$.

From Table A.2.3 or Eq. (A.2.33), $U_t = 1.13 \text{ sec}$. From Eq. (A.2.36), $U_{\overline{m_w}} = 0.1173 \text{ kg}$.

The absolute uncertainty in water mass flow rate is estimated using Eqs. (A.4.40) and (A.4.41a) as

$$U_{\overline{H}} = U_{\overline{\dot{m}_w}} = \sqrt{\left(\frac{0.1173}{293.10}\right)^2 + \left(-\frac{18.7674 \times 1.13}{(293.10)^2}\right)^2} = 4.70 \times 10^{-4} \text{ kg/s}, \quad (\text{A.4.41c})$$

and the relative uncertainty, from Eq. (A.4.41b) as

$$\frac{U_{\overline{H}}}{\overline{H}} = \frac{U_{\overline{\dot{m}_w}}}{\overline{\dot{m}_w}} = \sqrt{\left(\frac{0.1173}{18.7674}\right)^2 + \left(\frac{1.13}{293.10}\right)^2} = 0.00734 \approx 0.73 \%. \quad (\text{A.4.41d})$$

Uncertainty in the Waterside Flow Velocity inside Tube ($H = V_w$):

The waterside flow velocity is obtained from the following relationship

$$\overline{H} = \overline{V_w} = \frac{\overline{\dot{m}_w}}{\rho_w A_{c,i}} \text{ m/s}, \quad (\text{A.4.42})$$

where $A_{c,i}$ being the tube inner side cross-sectional area. The partial derivatives are

$$\frac{\partial \overline{V_w}}{\partial \overline{\dot{m}_w}} = \frac{1}{\rho_w A_{c,i}}, \quad \frac{\partial \overline{V_w}}{\partial \rho_w} = -\frac{\overline{\dot{m}_w}}{(\rho_w)^2 A_{c,i}}, \quad \text{and} \quad \frac{\partial \overline{V_w}}{\partial A_{c,i}} = -\frac{\overline{\dot{m}_w}}{\rho_w (A_{c,i})^2}. \quad (\text{A.4.43})$$

The uncertainty associated with this velocity was estimated to be

$$U_{\overline{H}} = U_{\overline{V_w}} = \sqrt{\left(\frac{\partial \overline{V_w}}{\partial \overline{\dot{m}_w}} U_{\overline{\dot{m}_w}}\right)^2 + \left(\frac{\partial \overline{V_w}}{\partial \rho_w} U_{\rho_w}\right)^2 + \left(\frac{\partial \overline{V_w}}{\partial A_{c,i}} U_{A_{c,i}}\right)^2} \text{ m/s}, \quad (\text{A.4.44a})$$

where the partial derivatives are taken from Eq. (A.4.43) and the uncertainty components; $U_{\dot{m}_w}$ from Eq. (A.4.41a), U_{ρ_w} using Eq. (A.3.2), and $U_{A_{c,i}}$ from Table A.4.1. The relative uncertainty (in %) was estimated to be

$$\frac{U_{\bar{H}}}{\bar{H}} (\%) = \frac{U_{\bar{V}_w}}{\bar{V}_w} (\%) = \sqrt{\left(\frac{U_{\dot{m}_w}}{\dot{m}_w}\right)^2 + \left(\frac{U_{\rho_w}}{\rho_w}\right)^2 + \left(\frac{U_{A_{c,i}}}{A_{c,i}}\right)^2} \times 100\%. \quad (\text{A.4.44b})$$

SAMPLE CALCULATION – Example Experimental Data Table A.1.1 ($H = V_w$):

From Table A.1.1: $\bar{V}_w = 0.338$ m/s, $\bar{\dot{m}}_w = 0.0641$ kg/s, and $\bar{\rho}_w = 997.55$ kg/m³.

From Eq. (A.4.41c): $U_{\dot{m}_w} = 4.70 \times 10^{-4}$ kg/s. From Eq. (A.3.24a): $U_{\rho_w} = \pm 0.012$ kg.

From Table A.4.1: $\bar{A}_{c,i} = 1.839 \times 10^{-4}$ m² and $U_{A_{c,i}} = \pm 1.961 \times 10^{-6}$ m². The absolute uncertainty in waterside velocity is estimated using Eqs. (A.4.43) and (A.4.44a) as

$$U_{\bar{H}} = U_{\bar{V}_w} = \sqrt{\left(\frac{4.70 \times 10^{-4}}{998 \times 1.84 \times 10^{-4}}\right)^2 + \left(\frac{0.0641 \times 0.012}{(998)^2 \times 1.84 \times 10^{-4}}\right)^2 + \left(\frac{0.0641 \times 1.961 \times 10^{-6}}{998 \times (1.84 \times 10^{-4})^2}\right)^2} = 0.00452 \text{ m/s} \quad (\text{A.4.44c})$$

and the relative uncertainty, from Eq. (A.4.44b) as

$$\frac{U_{\bar{H}}}{\bar{H}} = \frac{U_{\bar{V}_w}}{\bar{V}_w} = \sqrt{(0.00734)^2 + (1.203 \times 10^{-5})^2 + \left(\frac{1.961 \times 10^{-6}}{1.839 \times 10^{-4}}\right)^2} = 0.0134 \approx 1.30\%. \quad (\text{A.4.44d})$$

Uncertainty in the Waterside Reynolds number ($H = Re_w$):

The waterside Reynolds number, based on the inner-side hydraulic diameter of the elliptical tube, is defined as

$$\overline{H} = \overline{Re_w} = \frac{\overline{\rho_w} \overline{V_w} \overline{D_{h,i}}}{\overline{\mu_w}} = \frac{\overline{V_w} \overline{D_{h,i}}}{\overline{\nu_w}}, \quad (\text{A.4.45})$$

and its partial derivatives are

$$\frac{\partial \overline{Re_w}}{\partial \overline{V_w}} = \frac{\overline{D_{h,i}}}{\overline{\nu_w}}, \quad \frac{\partial \overline{Re_w}}{\partial \overline{D_{h,i}}} = \frac{\overline{V_w}}{\overline{\nu_w}}, \quad \text{and} \quad \frac{\partial \overline{Re_w}}{\partial \overline{\nu_w}} = -\frac{\overline{V_w} \overline{D_{h,i}}}{(\overline{\nu_w})^2}. \quad (\text{A.4.46})$$

The uncertainty associated with waterside Reynolds number was estimated to be

$$U_{\overline{H}} = U_{\overline{Re_w}} = \sqrt{\left(\frac{\partial \overline{Re_w}}{\partial \overline{V_w}} U_{\overline{V_w}} \right)^2 + \left(\frac{\partial \overline{Re_w}}{\partial \overline{D_{h,i}}} U_{\overline{D_{h,i}}} \right)^2 + \left(\frac{\partial \overline{Re_w}}{\partial \overline{\nu_w}} U_{\overline{\nu_w}} \right)^2}, \quad (\text{A.4.47a})$$

where the partial derivatives are taken from Eq. (A.4.46) and the uncertainty components;

$U_{\overline{V_w}}$ from Eq. (A.4.44a), $U_{\overline{D_{h,i}}}$ from Table A.4.1, and $U_{\overline{\nu_w}}$ using Eq. (A.3.2). The

relative uncertainty (in percentage) was estimated to be

$$\frac{U_{\overline{H}}}{\overline{H}} (\%) = \frac{U_{\overline{Re_w}}}{\overline{Re_w}} (\%) = \sqrt{\left(\frac{U_{\overline{V_w}}}{\overline{V_w}} \right)^2 + \left(\frac{U_{\overline{D_{h,i}}}}{\overline{D_{h,i}}} \right)^2 + \left(\frac{U_{\overline{\nu_w}}}{\overline{\nu_w}} \right)^2} \times 100\%. \quad (\text{A.4.47b})$$

SAMPLE CALCULATION – Example Experimental Data Table A.1.1 ($H = Re_w$):

From Table A.1.1: $\overline{Re_w} = 4235$, $\overline{V_w} = 0.3382$ m/s, and $\overline{\nu_w} = 9.338 \times 10^{-7}$ m²/s.

From Eq. (A.4.44c): $U_{\overline{V_w}} = 0.00452$ m/s. From Eq. (A.3.25a): $U_{\overline{\nu_w}} = 1 \times 10^{-9}$ m²/s.

From Table A.4.1: $\overline{D_{h,i}} = 0.01132$ m and $\overline{U_{D_{h,i}}} = 1.28 \times 10^{-4}$ m. The absolute uncertainty in waterside Reynolds number is estimated using Eqs. (A.4.46) and (A.4.47a) as

$$U_{\overline{H}} = U_{\overline{Re_w}} = \sqrt{\left(\frac{0.01132 \times 0.004522}{9.338 \times 10^{-7}}\right)^2 + \left(\frac{0.338 \times 1.28 \times 10^{-4}}{9.34 \times 10^{-7}}\right)^2 + \left(\frac{0.338 \times 0.01132 \times 1 \times 10^{-9}}{(9.34 \times 10^{-7})^2}\right)^2} = 72.87 \quad (\text{A.4.47c})$$

and the relative uncertainty, from Eq. (A.4.47b) as

$$\frac{U_{\overline{H}}}{\overline{H}} = \frac{U_{\overline{Re_w}}}{\overline{Re_w}} = \sqrt{(0.0134)^2 + (0.0113)^2 + (1.07 \times 10^{-3})^2} = 0.0175 \approx 1.75\% . \quad (\text{A.4.47d})$$

Uncertainty in the Waterside Heat Transfer Rate ($H = q_w$):

The heat transfer rate based on waterside analysis is defined by

$$\overline{H} = \overline{q_w} = \overline{\dot{m}_w} \overline{c_{p,w}} \left| \overline{T_{w,i}} - \overline{T_{w,o}} \right| = \overline{\dot{m}_w} \overline{c_{p,w}} \left| \overline{\Delta T_w} \right| \text{ W}, \quad (\text{A.4.48})$$

and the necessary partial derivatives are

$$\frac{\partial \overline{q_w}}{\partial \overline{\dot{m}_w}} = \overline{c_{p,w}} \overline{\Delta T_w}, \quad \frac{\partial \overline{q_w}}{\partial \overline{c_{p,w}}} = \overline{\dot{m}_w} \overline{\Delta T_w}, \quad \text{and} \quad \frac{\partial \overline{q_w}}{\partial \overline{\Delta T_w}} = \overline{\dot{m}_w} \overline{c_{p,w}} . \quad (\text{A.4.49})$$

The uncertainty associated with this heat transfer rate was estimated to be

$$U_{\overline{H}} = U_{\overline{q_w}} = \sqrt{\left(\frac{\partial \overline{q_w}}{\partial \overline{\dot{m}_w}} U_{\overline{\dot{m}_w}}\right)^2 + \left(\frac{\partial \overline{q_w}}{\partial \overline{c_{p,w}}} U_{\overline{c_{p,w}}}\right)^2 + \left(\frac{\partial \overline{q_w}}{\partial \overline{\Delta T_w}} U_{\overline{\Delta T_w}}\right)^2} \text{ W}, \quad (\text{A.4.50a})$$

where the partial derivatives are taken from Eq. (A.4.49) and the uncertainty components;

$\overline{U_{\dot{m}_w}}$ is taken from Eq. (A.4.41a), $\overline{U_{c_{p,w}}}$ using Eq. (A.3.2), and $\overline{U_{\Delta T_w}}$ from

Eq. (A.2.30) or from Table A.2.3. The relative uncertainty (in %) was estimated to be

$$\frac{\overline{U_H}}{H} (\%) = \frac{\overline{U_{q_w}}}{q_w} (\%) = \sqrt{\left(\frac{\overline{U_{\dot{m}_w}}}{\dot{m}_w}\right)^2 + \left(\frac{\overline{U_{c_{p,w}}}}{c_{p,w}}\right)^2 + \left(\frac{\overline{U_{\Delta T_w}}}{\Delta T_w}\right)^2} \times 100\%. \quad (\text{A.4.50b})$$

SAMPLE CALCULATION – Example Experimental Data Table A.1.1 ($H = q_w$):

From Table A.1.1: $\overline{q_w} = 562.67 \text{ W}$, $\overline{\dot{m}_w} = 0.0641 \text{ kg/s}$, $\overline{c_{p,w}} = 4183.03 \text{ J/kg}\cdot\text{C}$, and

$\overline{\Delta T_w} = \overline{T_{w,i}} - \overline{T_{w,o}} = 2.10\text{C}$. From Eq. (A.4.41c): $\overline{U_{\dot{m}_w}} = 4.70 \times 10^{-4} \text{ kg/s}$. From Eq. (A.3.23a):

$\overline{U_{c_{p,w}}} = 1.35 \times 10^{-3} \text{ J/kg}\cdot\text{C}$. From Table A.2.3: $\overline{U_{\Delta T_w}} = 0.10\text{C}$. The absolute uncertainty in

waterside Heat transfer rate is estimated using Eqs. (A.4.49) and (A.4.50a) as

$$\overline{U_H} = \overline{U_{q_w}} = \sqrt{\left(4183 \times 2.10 \times (4.70 \times 10^{-4})\right)^2 + \left(0.064 \times 2.10 \times (1.35 \times 10^{-3})\right)^2 + (0.064 \times 4183 \times 0.10)^2} = 27.13 \text{ W}, \quad (\text{A.4.50c})$$

and the relative uncertainty, from Eq. (A.4.50b) as

$$\frac{\overline{U_H}}{H} = \frac{\overline{U_{q_w}}}{q_w} = \sqrt{(0.00734)^2 + (3.23 \times 10^{-7})^2 + \left(\frac{0.10}{2.10}\right)^2} = 0.0482 \approx 4.82\%. \quad (\text{A.4.50d})$$

A.5. Propagation of Uncertainties into the Representative Results

In the current study, for both airside and waterside, the experimental results were represented in the form of dimensionless heat transfer coefficient (i.e. the Nusselt number, Nu). The effect of Reynolds number (Re) on Nu and on the airflow pressure drop (in terms of pressure coefficient, C_{press}) across the tube array were presented. The uncertainties from the basic dependent parameters, as estimated in section D, propagate into these presented results depending on the relationship of representative results with that of the basic dependent parameters. In this view, the uncertainty associated with Nu for both airside and waterside and C_{press} for airside are estimated in this section. The heat transfer coefficient, h , and hence the Nu were calculated based on the overall heat transfer rate, q . This q was taken to be the arithmetic average of the heat transfer rate at airside (q_a) and the heat transfer rate at waterside (q_w). To proceed with, we have to first obtain the uncertainty associated with the q and then with h .

Uncertainty in the Overall Heat Transfer Rate ($H = q$):

The overall heat transfer rate was considered to

$$\overline{H} = \overline{q} = \frac{\overline{q_a} + \overline{q_w}}{2} \text{ W,} \quad (\text{A.5.1})$$

and its partial derivatives are

$$\frac{\partial \overline{q}}{\partial q_a} = \frac{1}{2} \text{ and } \frac{\partial \overline{q}}{\partial q_w} = \frac{1}{2}. \quad (\text{A.5.2})$$

The uncertainty associated with overall heat transfer rate, q , is given by

$$U_{\overline{H}} = U_{\overline{q}} = \sqrt{\left(\frac{\partial \overline{q}}{\partial q_a} U_{q_a}\right)^2 + \left(\frac{\partial \overline{q}}{\partial q_w} U_{q_w}\right)^2}, \quad (\text{A.5.3a})$$

where the partial derivatives are taken from Eq. (A.5.2) and the uncertainty components; $U_{q_a}^-$ is taken from Eq. (A.4.38a) and $U_{q_w}^-$ from Eq. (A.4.50a). The relative uncertainty (in percentage) was estimated to be

$$\frac{U_{\bar{H}}}{\bar{H}} (\%) = \frac{U_{\bar{q}}}{\bar{q}} (\%) = \frac{1}{q_a + q_w} \sqrt{(U_{q_a}^-)^2 + (U_{q_w}^-)^2} \times 100\%. \quad (\text{A.5.3b})$$

SAMPLE CALCULATION – Example Experimental Data Table A.1.1 ($H = q$):

From Table A.1.1: $\bar{q}_a = 559.40 \text{ W}$, $\bar{q}_w = 562.67 \text{ W}$, and $\bar{q} = 561.04 \text{ W}$. From Eq. (A.4.38c): $U_{q_a}^- = 102.08 \text{ W}$, and from Eq. (A.4.50c): $U_{q_w}^- = 27.13 \text{ W}$. The absolute uncertainty in overall Heat transfer rate is estimated using Eqs. (A.5.2) and (A.5.3a) as

$$U_{\bar{H}} = U_{\bar{q}} = \sqrt{\left(\frac{1}{2} \times 102.08\right)^2 + \left(\frac{1}{2} \times 27.13\right)^2} = 52.81 \text{ W} \quad (\text{A.5.3c})$$

and the relative uncertainty, from Eq. (A.5.3b) as

$$\frac{U_{\bar{H}}}{\bar{H}} = \frac{U_{\bar{q}}}{\bar{q}} = \frac{1}{559.4 + 562.67} \sqrt{(102.07)^2 + (27.13)^2} = 0.0941 \approx 9.41\% \quad (\text{A.5.3d})$$

Uncertainty in the Heat Transfer Coefficient ($H = h_a$ or h_w):

The heat transfer coefficient, h , is obtained from the overall heat transfer rate, q as follows

$$\bar{H} = \bar{h} = \frac{\bar{q}}{A_s |T - T_s|} = \frac{\bar{q}}{A_s \Delta T}. \quad (\text{A.5.4})$$

and its partial derivatives are

$$\frac{\partial \bar{h}}{\partial \bar{q}} = \frac{1}{A_s \Delta T}, \quad \frac{\partial \bar{h}}{\partial A_s} = -\frac{\bar{q}}{(A_s)^2 \Delta T}, \quad \text{and} \quad \frac{\partial \bar{h}}{\partial \Delta T} = -\frac{\bar{q}}{A_s (\Delta T)^2}. \quad (\text{A.5.5})$$

The uncertainty associated with the heat transfer coefficient was estimated to be

$$U_{\bar{H}} = U_{\bar{h}} = \sqrt{\left(\frac{\partial \bar{h}}{\partial \bar{q}} U_{\bar{q}} \right)^2 + \left(\frac{\partial \bar{h}}{\partial A_s} U_{A_s} \right)^2 + \left(\frac{\partial \bar{h}}{\partial \Delta T} U_{\Delta T} \right)^2}, \quad (\text{A.5.6a})$$

and the relative uncertainty (in percentage) was estimated to be

$$\frac{U_{\bar{H}}}{\bar{H}} (\%) = \frac{U_{\bar{h}}}{\bar{h}} (\%) = \sqrt{\left(\frac{U_{\bar{q}}}{\bar{q}} \right)^2 + \left(\frac{U_{A_s}}{A_s} \right)^2 + \left(\frac{U_{\Delta T}}{\Delta T} \right)^2} \times 100\%, \quad (\text{A.5.6b})$$

where the partial derivatives are taken from Eq. (A.5.5) and the uncertainty components;

$U_{\bar{q}}$ is taken from Eq. (A.5.3a), U_{A_s} (i.e. $\overline{A_{s,o}}$ for airside or $\overline{A_{s,i}}$ for waterside) from

Table A.4.1, and $U_{\Delta T}$ from Eq. (A.2.30) or Table A.2.3.

SAMPLE CALCULATION – Example Experimental Data Table A.1.1 ($H = h_a$):

From Table A.1.1: $\bar{h}_a = 116.30 \frac{\text{W}}{\text{m}^2 \cdot ^\circ\text{C}}$, $\overline{\Delta T_{a,i \leftrightarrow s,o}} = \overline{T_{s,o}} - \overline{T_{a,i}} = 12.55^\circ\text{C}$, and

$\bar{q} = 560 \text{ W}$. From Table A.2.3: $U_{\overline{\Delta T_{a,i \leftrightarrow s,o}}} = 0.10^\circ\text{C}$. From Table A.4.1:

$\overline{A_{s,o}} = 0.3799 \text{ m}^2$, and $U_{\overline{A_{s,o}}} = 1.215 \times 10^{-3} \text{ m}^2$. From Eq. (A.5.3c): $U_{\bar{q}} = 52.81 \text{ W}$. The

absolute uncertainty in airside Heat transfer coefficient is estimated using Eqs. (A.5.5)

and (A.5.6a) as

$$\begin{aligned}
 U_{\overline{H}} = U_{\overline{h_a}} &= \sqrt{\left(\frac{U_{\overline{q}}}{A_{s,o} \Delta T_{a,i \leftrightarrow s,o}}\right)^2 + \left(\frac{\overline{q} U_{\overline{A_{s,o}}}}{(A_{s,o})^2 \Delta T_{a,i \leftrightarrow s,o}}\right)^2 + \left(\frac{\overline{q} U_{\overline{\Delta T_{a,i \leftrightarrow s,o}}}}{A_{s,o} (\Delta T_{a,i \leftrightarrow s,o})^2}\right)^2} \quad (\text{A.5.6c}) \\
 &= \sqrt{\left(\frac{52.81}{0.3799 \times 12.6}\right)^2 + \left(\frac{560 \times 1.21 \times 10^{-3}}{(0.3799)^2 \times 12.6}\right)^2 + \left(\frac{560 \times 0.10}{0.3799 \times (12.6)^2}\right)^2} = 11.12 \frac{\text{W}}{\text{m}^2 \cdot ^\circ\text{C}}
 \end{aligned}$$

and the relative uncertainty, from Eq. (A.5.6b) as

$$\begin{aligned}
 \frac{U_{\overline{H}}}{\overline{H}} = \frac{U_{\overline{h_a}}}{\overline{h_a}} &= \sqrt{\left(\frac{U_{\overline{q}}}{\overline{q}}\right)^2 + \left(\frac{U_{\overline{A_{s,o}}}}{\overline{A_{s,o}}}\right)^2 + \left(\frac{U_{\overline{\Delta T_{a,i \leftrightarrow s,o}}}}{\overline{\Delta T_{a,i \leftrightarrow s,o}}}\right)^2} \quad (\text{A.5.6d}) \\
 &= \sqrt{(0.0941)^2 + (3.198 \times 10^{-3})^2 + \left(\frac{0.10}{12.55}\right)^2} = 0.0945 \approx 9.45 \%
 \end{aligned}$$

SAMPLE CALCULATION – Example Experimental Data Table A.1.1 ($H = h_w$):

From Table A.1.1: $\overline{h_w} = 443 \frac{\text{W}}{\text{m}^2 \cdot ^\circ\text{C}}$, and $\overline{\Delta T_{w,b \leftrightarrow s,i}} = \overline{T_{w,b}} - \overline{T_{s,i}} = 3.52^\circ\text{C}$, and

$\overline{q} = 560 \text{ W}$. From Table A.2.3: $U_{\overline{\Delta T_{w,b \leftrightarrow s,i}}} = 0.10^\circ\text{C}$. From Table A.4.1: $\overline{A_{s,i}} = 0.354 \text{ m}^2$,

and $U_{\overline{A_{s,i}}} = 1.53 \times 10^{-3} \text{ m}^2$. From Eq. (A.5.3c): $U_{\overline{q}} = 52.81 \text{ W}$. The absolute uncertainty

in waterside Heat transfer coefficient is estimated using Eqs. (A.5.5) and (A.5.6a) as

$$U_{\overline{H}} = U_{\overline{h_w}} = \sqrt{\left(\frac{U_{\overline{q}}}{A_{s,i} \Delta T_{w,b \leftrightarrow s,i}}\right)^2 + \left(\frac{\overline{q} U_{\overline{A_{s,i}}}}{(A_{s,i})^2 \Delta T_{w,b \leftrightarrow s,i}}\right)^2 + \left(\frac{\overline{q} U_{\overline{\Delta T_{w,b \leftrightarrow s,i}}}}{A_{s,i} (\Delta T_{w,b \leftrightarrow s,i})^2}\right)^2} \quad (\text{A.5.6e})$$

$$= \sqrt{\left(\frac{52.81}{0.35398 \times 3.52}\right)^2 + \left(\frac{560 \times 1.529 \times 10^{-3}}{(0.35398)^2 \times 3.52}\right)^2 + \left(\frac{560 \times 0.10}{0.35398 \times (3.52)^2}\right)^2} = 44.33 \frac{\text{W}}{\text{m}^2 \cdot ^\circ\text{C}}$$

and the relative uncertainty, from Eq. (A.5.6b) as

$$\begin{aligned} \frac{U_{\overline{H}}}{\overline{H}} = \frac{U_{\overline{h_w}}}{\overline{h_w}} &= \sqrt{\left(\frac{U_{\overline{q}}}{\overline{q}}\right)^2 + \left(\frac{U_{\overline{A_{s,i}}}}{\overline{A_{s,i}}}\right)^2 + \left(\frac{U_{\overline{\Delta T_{w,b \leftrightarrow s,i}}}}{\overline{\Delta T_{w,b \leftrightarrow s,i}}}\right)^2} \quad (\text{A.5.6f}) \\ &= \sqrt{(0.0941)^2 + (4.319 \times 10^{-3})^2 + \left(\frac{0.10}{3.52}\right)^2} = 0.0983 \approx 9.84 \% \end{aligned}$$

A.5.1. Uncertainty in the Airside Nusselt number – ($H = \text{Nu}_a$)

Nusselt number for the airside is defined as

$$\overline{H} = \overline{\text{Nu}_a} = \frac{\overline{h_a} (2a_o)}{\overline{k_a}}. \quad (\text{A.5.7})$$

and its partial derivatives are

$$\frac{\partial \overline{\text{Nu}_a}}{\partial \overline{h_a}} = \frac{2a_o}{\overline{k_a}}, \quad \frac{\partial \overline{\text{Nu}_a}}{\partial (2a_o)} = \frac{\overline{h_a}}{\overline{k_a}}, \quad \text{and} \quad \frac{\partial \overline{\text{Nu}_a}}{\partial \overline{k_a}} = -\frac{\overline{h_a} (2a_o)}{(\overline{k_a})^2}. \quad (\text{A.5.8})$$

The uncertainty associated with the Nusselt number was estimated to be

$$U_{\overline{H}} = U_{\overline{\text{Nu}_a}} = \sqrt{\left(\frac{\partial \overline{\text{Nu}_a}}{\partial \overline{h_a}} U_{\overline{h_a}}\right)^2 + \left(\frac{\partial \overline{\text{Nu}_a}}{\partial (2a_o)} U_{2a_o}\right)^2 + \left(\frac{\partial \overline{\text{Nu}_a}}{\partial \overline{k_a}} U_{\overline{k_a}}\right)^2}, \quad (\text{A.5.9a})$$

and the relative uncertainty (in percentage) was estimated to be

$$\frac{U_{\overline{H}}}{\overline{H}} (\%) = \frac{U_{\overline{Nu}_a}}{\overline{Nu}_a} (\%) = \sqrt{\left(\frac{U_{\overline{h}_a}}{\overline{h}_a}\right)^2 + \left(\frac{U_{\overline{2a_o}}}{\overline{2a_o}}\right)^2 + \left(\frac{U_{\overline{k}_a}}{\overline{k}_a}\right)^2} \times 100\%, \quad (\text{A.5.9b})$$

where the partial derivatives are taken from Eq. (A.5.8) and the uncertainty components;

$U_{\overline{h}_a}$ is taken from Eq. (A.5.6a), $U_{\overline{2a_o}}$ from Table A.2.2, and $U_{\overline{k}_a}$ using Eq. (A.3.1).

SAMPLE CALCULATION – Example Experimental Data Table A.1.1 ($H = Nu_a$):

From Table A.1.1: $\overline{Nu}_a = 150$, $\overline{h}_a = 116.30 \text{ W/m}^2\text{°C}$, and $\overline{k}_a = 0.02463 \text{ W/m}^2\text{°C}$.

From Table A.2.2: $\overline{2a_o} = 0.03164 \text{ m}$, and $U_{\overline{2a_o}} = 5.57 \times 10^{-5} \text{ m}$. From Eq. (A.3.18a):

$U_{\overline{k}_a} = 5.43 \times 10^{-5} \text{ W/m}^2\text{°C}$. From Eq. (A.5.6c): $U_{\overline{h}_a} = 11.12 \text{ W/m}^2\text{°C}$. Now the absolute

uncertainty in airside Nusselt number is estimated using Eqs. (A.5.8) and (A.5.9a) as

$$\begin{aligned} U_{\overline{H}} = U_{\overline{Nu}_a} &= \sqrt{\left(\frac{\overline{2a_o} U_{\overline{h}_a}}{\overline{k}_a}\right)^2 + \left(\frac{\overline{h}_a U_{\overline{2a_o}}}{\overline{k}_a}\right)^2 + \left(\frac{\overline{h}_a \overline{2a_o} U_{\overline{k}_a}}{(\overline{k}_a)^2}\right)^2} \\ &= \sqrt{\left(\frac{0.0316 \times 11.12}{0.02463}\right)^2 + \left(\frac{116.30 \times 5.57 \times 10^{-5}}{0.02463}\right)^2 + \left(\frac{116.30 \times 0.0316 \times 5.43 \times 10^{-5}}{(0.02463)^2}\right)^2} = 14.24 \end{aligned} \quad (\text{A.5.9c})$$

and the relative uncertainty, from Eq. (E.9b) as

$$\frac{U_{\overline{H}}}{\overline{H}} = \frac{U_{\overline{Nu}_a}}{\overline{Nu}_a} = \sqrt{(0.0945)^2 + (1.76 \times 10^{-3})^2 + (0.0221)^2} = 0.0945 \approx 9.45\% \quad (\text{A.5.9d})$$

A.5.2. Uncertainty in the Airside Pressure Drop Coefficient – ($H = C_{\text{press}}$)

The non-dimensional airflow pressure drop across the tube array, i.e. the Pressure Coefficient for a single tube in the array is defined as

$$\overline{H} = \overline{C_{\text{press}}} = \frac{\overline{\Delta p_{\text{array}}}}{\frac{1}{2} \rho_a \overline{(V_a)}^2 N_T} = \frac{2 \overline{\Delta p_{\text{array}}}}{N_T \rho_a \overline{(V_a)}^2}. \quad (\text{A.5.10})$$

and its partial derivatives are

$$\begin{aligned} \frac{\partial \overline{C_{\text{press}}}}{\partial \overline{\Delta p_{\text{array}}}} &= \frac{2}{N_T \rho_a \overline{(V_a)}^2}; & \frac{\partial \overline{C_{\text{press}}}}{\partial \rho_a} &= -\frac{2 \overline{\Delta p_{\text{array}}}}{N_T (\rho_a)^2 \overline{(V_a)}^2}; \\ \frac{\partial \overline{C_{\text{press}}}}{\partial \overline{V_a}} &= -\frac{4 \overline{\Delta p_{\text{array}}}}{N_T \rho_a \overline{(V_a)}^3}; & \text{and } \frac{\partial \overline{C_{\text{press}}}}{\partial N_T} &= -\frac{2 \overline{\Delta p_{\text{array}}}}{N_T^2 \rho_a \overline{(V_a)}^2}. \end{aligned} \quad (\text{A.5.11})$$

The uncertainty associated with the Nusselt number was estimated to be

$$U_{\overline{H}} = U_{\overline{C_{\text{press}}}} = \sqrt{\left(\frac{\partial \overline{C_{\text{press}}}}{\partial \overline{\Delta p_{\text{array}}}} U_{\overline{\Delta p_{\text{array}}}} \right)^2 + \left(\frac{\partial \overline{C_{\text{press}}}}{\partial \rho_a} U_{\overline{\rho_a}} \right)^2 + \left(\frac{\partial \overline{C_{\text{press}}}}{\partial \overline{V_a}} U_{\overline{V_a}} \right)^2 + \left(\frac{\partial \overline{C_{\text{press}}}}{\partial N_T} U_{\overline{N_T}} \right)^2}, \quad (\text{A.5.12a})$$

where, the partial derivatives are taken from Eq. (A.5.11) and the uncertainty components; $U_{\overline{\Delta p_{\text{array}}}}$ from Eq. (A.2.22a) or Table A.2.3, $U_{\overline{\rho_a}}$ using Eq. (A.3.1), and $U_{\overline{V_a}}$ from Eq. (A.4.29a). The other component, $U_{\overline{N_T}}$, is taken to be zero because the number of tubes (N_T) in the array is fixed to 18. The relative uncertainty (in percentage) was estimated to be

$$\frac{U_{\overline{H}}}{\overline{H}} (\%) = \frac{U_{\overline{C_{press}}}}{\overline{C_{press}}} (\%) = \sqrt{\left(\frac{U_{\overline{\Delta p_{array}}}}{\overline{\Delta p_{array}}}\right)^2 + \left(\frac{U_{\overline{\rho_a}}}{\overline{\rho_a}}\right)^2 + \left(\frac{2U_{\overline{V_a}}}{\overline{V_a}}\right)^2} \times 100\% , \quad (\text{A.5.12b})$$

SAMPLE CALCULATION – Example Experimental Data Table A.1.1 ($H = C_{press}$):

From Table A.1.1: $\overline{C_{press}} = 0.207$, $\overline{V_a} = 8.92$ m/s, $\overline{\rho_a} = 1.233$ kg/m³ and $\overline{\Delta p_{array}} = 181$ Pa. From Eq. (A.2.22b): $U_{\overline{\Delta p_{array}}} = 6.05$ Pa. From Eq. (A.3.19a): $U_{\overline{\rho_a}} = 3.1173 \times 10^{-3}$ kg/m³. From Eq. (A.4.29c): $U_{\overline{V_a}} = 0.13$ m/s. The absolute uncertainty in airside pressure coefficient for a single tube in the array was estimated using Eqs. (A.5.11) and (A.5.12a) as

$$U_{\overline{H}} = U_{\overline{C_{press}}} = \sqrt{\left(\frac{2 U_{\overline{\Delta p_{array}}}}{N_T \overline{\rho_a} (\overline{V_a})^2}\right)^2 + \left(\frac{2 \overline{\Delta p_{array}} U_{\overline{\rho_a}}}{N_T (\overline{\rho_a})^2 (\overline{V_a})^2}\right)^2 + \left(\frac{4 \overline{\Delta p_{array}} U_{\overline{V_a}}}{N_T \overline{\rho_a} (\overline{V_a})^3}\right)^2} \quad (\text{A.5.12c})$$

$$= \sqrt{\left(\frac{2 \times 6.05}{18 \times 1.233 \times (8.92)^2}\right)^2 + \left(\frac{2 \times 181 \times 3.1177 \times 10^{-3}}{18 \times (1.233)^2 \times (8.92)^2}\right)^2 + \left(\frac{4 \times 181 \times 0.13}{18 \times 1.233 \times (8.92)^3}\right)^2} = 0.0092$$

and the relative uncertainty, from Eq. (A.5.12b) as

$$\frac{U_{\overline{H}}}{\overline{H}} = \frac{U_{\overline{C_{press}}}}{\overline{C_{press}}} = \sqrt{(0.0334)^2 + (2.53 \times 10^{-3})^2 + (2 \times 0.0147)^2} = 0.0446 \approx 4.46\% \quad (\text{A.5.12d})$$

Similarly, for this typical experimental run for $V_a = 8.92$ m/s, the uncertainty in the pressure coefficient for the whole array was also estimated. The mean air velocity at the narrowest gap between two adjacent tube surfaces was calculated from Eq. (4.3.3) to

be $\overline{V_{a,\max}} = 22.48$ m/s, where the mean value of the void fraction was $\overline{\psi} = 2.52$. The mean pressure coefficient for the whole array was calculated to be $\overline{C_{\text{press,array}}} = 0.58$. The uncertainty in calculation of the void fraction was determined from Eq. (A.5.13a) to be $U_{\overline{\psi}} = 0.0172$.

$$U_{\overline{H}} = U_{\overline{\psi}} = \sqrt{\left(\frac{\partial \overline{\psi}}{\partial (2b_o)} U_{2b_o}\right)^2 + \left(\frac{\partial \overline{\psi}}{\partial S_T} U_{S_T}\right)^2} = \sqrt{\left(\frac{U_{2b_o}}{S_T}\right)^2 + \left(\frac{2b_o U_{S_T}}{S_T}\right)^2}. \quad (\text{A.5.13a})$$

The uncertainty in $V_{a,\max}$ was calculated from Eq. (A.5.13b) to be $U_{\overline{V_{a,\max}}} = 0.3616$ m/s.

$$U_{\overline{H}} = U_{\overline{V_{a,\max}}} = \sqrt{\left(\frac{\partial \overline{V_{a,\max}}}{\partial \overline{\psi}} U_{\overline{\psi}}\right)^2 + \left(\frac{\partial \overline{V_{a,\max}}}{\partial \overline{V_a}} U_{\overline{V_a}}\right)^2} = \sqrt{(\overline{V_a} U_{\overline{\psi}})^2 + (\overline{\psi} U_{\overline{V_a}})^2}. \quad (\text{A.5.13b})$$

Now the relative uncertainty (in percentage) was estimated as follows,

$$U_{\overline{H}} = \frac{U_{\overline{C_{\text{press,array}}}}}{\overline{C_{\text{press,array}}}} = \sqrt{\left(\frac{U_{\overline{\Delta p_{\text{array}}}}}{\overline{\Delta p_{\text{array}}}}\right)^2 + \left(\frac{U_{\overline{\rho_a}}}{\overline{\rho_a}}\right)^2 + \left(\frac{2U_{\overline{V_{a,\max}}}}{\overline{V_{a,\max}}}\right)^2} \quad (\text{A.5.13c})$$

$$= \sqrt{\left(\frac{6.05}{181}\right)^2 + (2.529 \times 10^{-3})^2 + \left(\frac{2 \times 0.3616}{22.48}\right)^2} = 0.4663 \approx 4.66\%$$

A.5.3. Uncertainty in the Waterside Nusselt number – ($H = Nu_w$):

Nusselt number for the waterside is defined as

$$\overline{H} = \overline{Nu_w} = \frac{\overline{h_w} \overline{D_{h,i}}}{\overline{k_w}}. \quad (\text{A.5.14})$$

and its partial derivatives are

$$\frac{\partial \overline{Nu_w}}{\partial \overline{h_w}} = \frac{\overline{D_{h,i}}}{\overline{k_w}}, \quad \frac{\partial \overline{Nu_w}}{\partial \overline{D_{h,i}}} = \frac{\overline{h_w}}{\overline{k_w}}, \quad \text{and} \quad \frac{\partial \overline{Nu_w}}{\partial \overline{k_w}} = -\frac{\overline{h_w} \overline{D_{h,i}}}{(\overline{k_w})^2}. \quad (\text{A.5.15})$$

The uncertainty associated with the Nusselt number was estimated to be

$$U_{\overline{H}} = U_{\overline{Nu_w}} = \sqrt{\left(\frac{\partial \overline{Nu_w}}{\partial \overline{h_w}} U_{\overline{h_w}}\right)^2 + \left(\frac{\partial \overline{Nu_w}}{\partial \overline{D_{h,i}}} U_{\overline{D_{h,i}}}\right)^2 + \left(\frac{\partial \overline{Nu_w}}{\partial \overline{k_w}} U_{\overline{k_w}}\right)^2}, \quad (\text{A.5.16a})$$

and the relative uncertainty (in percentage) was estimated to be

$$\frac{U_{\overline{H}}}{\overline{H}} (\%) = \frac{U_{\overline{Nu_w}}}{\overline{Nu_w}} (\%) = \pm \sqrt{\left(\frac{U_{\overline{h_w}}}{\overline{h_w}}\right)^2 + \left(\frac{U_{\overline{D_{h,i}}}}{\overline{D_{h,i}}}\right)^2 + \left(\frac{U_{\overline{k_w}}}{\overline{k_w}}\right)^2} \times 100\%, \quad (\text{A.5.16b})$$

where the partial derivatives are taken from Eq. (A.5.15) and the uncertainty components;

$U_{\overline{h_w}}$ is taken from Eq. (A.5.6a), $U_{\overline{D_{h,i}}}$ from Table A.4.1, and $U_{\overline{k_w}}$ using Eq. (A.3.2).

SAMPLE CALCULATION – Example Experimental Data Table A.1.1 ($H = Nu_w$):

From Table A.1.1: $\overline{Nu_w} = 8.31$, $\overline{h_w} = 443 \text{ W/m}^2\cdot\text{°C}$, and $\overline{k_w} = 0.604 \text{ W/m}\cdot\text{°C}$.

From Table A.4.1: $\overline{D_{h,i}} = 0.01132 \text{ m}$, and $U_{\overline{D_{h,i}}} = 1.28 \times 10^{-4} \text{ m}$. From Eq. (A.3.23a):

$U_{\overline{k_w}} = 8.68 \times 10^{-5} \text{ W/m}\cdot\text{°C}$. From Eq. (A.5.6e): $U_{\overline{h_w}} = 44.33 \text{ W/m}^2\cdot\text{°C}$. The absolute

uncertainty in Nu_w number was estimated using Eqs. (A.5.15) and (A.5.16a) as

$$U_{\overline{H}} = U_{\overline{Nu_w}} = \sqrt{\left(\frac{\overline{D_{h,i}} U_{\overline{h_w}}}{\overline{k_w}}\right)^2 + \left(\frac{\overline{h_w} U_{\overline{D_{h,i}}}}{\overline{k_w}}\right)^2 + \left(\frac{\overline{h_w} \overline{D_{h,i}} U_{\overline{k_w}}}{(\overline{k_w})^2}\right)^2} \quad (\text{A.5.16c})$$

$$= \sqrt{\left(\frac{0.01132 \times 44.33}{0.604}\right)^2 + \left(\frac{443 \times 1.28 \times 10^{-4}}{0.604}\right)^2 + \left(\frac{443 \times 0.01132 \times 1.7 \times 10^{-4}}{(0.604)^2}\right)^2} = 0.80$$

and the relative uncertainty, from Eq. (A.5.16b) as

$$\frac{U_{\overline{H}}}{\overline{H}} = \frac{U_{\overline{Nu_w}}}{\overline{Nu_w}} = \sqrt{(0.0983)^2 + (0.01131)^2 + (0.0001438)^2} = 0.099 \approx 9.90 \% \quad (\text{A.5.16d})$$

A.6. Tabulation of Overall Uncertainty Data for all the Experiments

The uncertainties for all the experimental operating conditions and for all the runs were estimated according to the procedures and calculations described above. Table A.6.1 lists the data for the key parameters.

Table A.6.1 Overall Uncertainty Data for all the Experiments

AIRSIDE		WATERSIDE	
Parameters	Uncertainty	Parameters	Uncertainty
Re_a	1 – 4 %	Re_w	2 – 4 %
h_a [W/m ² .°C]	4 – 13 %	h_w [W/m ² .°C]	4 – 14 %
Nu_a	4 – 13 %	Nu_w	5 – 14 %
C_{press}	3 – 12 %		
$C_{press, array}$	3 – 12 %		
Overall for both Airside and Waterside			
Parameter		Uncertainty	
q [Watt]		3 – 12 %	

APPENDIX - B

TABULATION OF EXPERIMENTAL RESULTS

Table B.1 Heat Transfer Data corresponding to different Re_a (for a given Re_w)

Experimental phases and test conditions	Waterside data				Airside data		
	Re_w	h_w [W/m ² .°C]	Nu_w	q [Watt]	Re_a	h_a [W/m ² .°C]	Nu_a
Phase-I: Air Cooling ($T_{a,i}$ and $T_{w,i}$ maintained constant)	1079	341	6.65	823	9944	91.61	112
	1135	340	6.54	961	19860	138.01	168
	1105	346	6.65	1228	27293	179.42	217
	1054	336	6.47	1244	33099	186.88	226
	1826	388	7.64	869	10085	84.18	104
	1905	402	7.84	1126	19942	130.99	160
	1888	410	7.99	1428	27385	169.29	206
	1883	416	8.13	1515	33390	177.69	217
	2527	406	8.03	882	10111	81.34	100
	2616	453	8.89	1269	19944	135.96	167
	2912	461	9.02	1517	27454	163.91	200
	2686	456	8.97	1654	33525	179.89	220
	3450	427	8.47	898	10212	80.47	100
	3451	446	8.79	1268	19931	129.28	159
	4033	536	10.52	1665	27727	185.74	227
	3484	497	9.81	1720	33613	184.34	226
	1744	422	7.68	547	10935	101.66	127
	1554	390	7.10	723	20849	144.38	180
	1460	390	7.12	855	30694	187.29	234
	1407	382	6.98	825	34079	204.64	256
Phase-II: Air Heating ($T_{a,i}$ and $T_{w,i}$ maintained constant)	3246	525	9.51	581	10553	94.66	118
	3353	536	9.72	841	20646	147.84	184
	3347	522	9.48	944	30838	189.28	235
	3455	548	9.95	847	33247	211.34	263
	5469	513	9.26	560	10506	86.6	107
	5305	566	10.22	790	20445	144.84	179
	5133	628	11.35	943	29701	178.11	220
	5371	568	10.25	948	33607	204.97	254
	7348	632	11.42	591	10316	90.08	111
	7386	633	11.44	777	20399	137.76	170
	7100	578	10.44	1016	29679	179.16	222
	7269	549	9.91	1012	33038	187.17	231
	3297	531	10.22	420	10308	92.02	115
3175	534	10.28	527	18429	129.46	162	
3331	535	10.29	623	26638	165.76	207	
3229	536	10.30	679	33518	194.3	242	
Phase-III: Air Cooling (ΔT_{a-w} maintained constant)	5571	509	9.83	442	10302	85.63	107
	5658	504	9.69	574	18300	118.25	147
	6642	510	9.62	680	25709	147.34	179
	6260	562	10.62	742	32479	184.43	226
	4110	483	9.08	434	10857	84.51	109
	*4232	443	8.31	560	19292	116.3	150
Phase-IV: Air Heating (ΔT_{a-w} maintained constant)	3870	427	8.02	630	27895	148.6	191
	4117	494	9.28	712	35756	181.91	234
	7012	500	9.38	437	10834	81.75	105
	7206	528	9.88	614	19244	122.05	156
	7235	486	9.10	651	27701	139.12	178
	7075	568	10.64	812	35823	193.23	248

* Data set in the shaded row is presented in the uncertainty analysis

Table B.2 Heat Transfer Data corresponding to different Re_w (for a given Re_a)

Experimental phases and test conditions	Waterside data			q [Watt]	Airside data		
	Re_w	h_w [W/m ² .°C]	Nu_w		Re_a	h_a [W/m ² .°C]	Nu_a
Phase-I: Air Cooling ($T_{a,i}$ and $T_{w,i}$ maintained constant)	1079	341	6.65	823	9944	91.61	112
	1826	388	7.64	869	10085	84.18	104
	2527	406	8.03	882	10111	81.34	100
	3450	427	8.47	898	10212	80.47	100
	1135	340	6.54	961	19860	138.01	168
	1905	402	7.84	1126	19942	130.99	160
	2616	453	8.89	1269	19944	135.96	167
	3451	446	8.79	1268	19931	129.28	159
	1105	346	6.65	1228	27293	179.42	217
	1888	410	7.99	1428	27385	169.29	206
	2912	461	9.02	1517	27454	163.91	200
	4033	536	10.52	1665	27727	185.74	227
	1054	336	6.47	1244	33099	186.88	226
	1883	416	8.13	1515	33390	177.69	217
	2686	456	8.97	1654	33525	179.89	220
	3484	497	9.81	1720	33613	184.34	226
Phase-II: Air Heating ($T_{a,i}$ and $T_{w,i}$ maintained constant)	1744	422	7.68	547	10935	101.66	127
	3246	525	9.51	581	10553	94.66	118
	5469	513	9.26	560	10506	86.60	107
	7348	632	11.42	591	10316	90.08	111
	1554	390	7.10	723	20849	144.38	180
	3353	536	9.72	841	20646	147.84	184
	5305	566	10.22	790	20445	144.84	179
	7386	633	11.44	777	20399	137.76	170
	1460	390	7.12	855	30694	187.29	234
	3347	522	9.48	944	30838	189.28	235
	5133	628	11.35	943	29701	178.11	220
	7100	578	10.44	1016	29679	179.16	222
	1407	382	6.98	825	34079	204.64	256
	3455	548	9.95	847	33247	211.34	263
	5371	568	10.25	948	33607	204.97	254
	7269	549	9.91	1012	33038	187.17	231
Phase-III: Air Cooling (ΔT_{a-w} maintained constant)	3297	531	10.22	420	10308	92.02	115
	5571	509	9.83	442	10302	85.63	107
	3175	534	10.28	527	18429	129.46	162
	5658	504	9.69	574	18300	118.25	147
	3331	535	10.29	623	26638	165.76	207
	6642	510	9.62	680	25709	147.34	179
	3229	536	10.30	679	33518	194.30	242
	6260	562	10.62	742	32479	184.43	226
Phase-IV: Air Heating (ΔT_{a-w} maintained constant)	4110	483	9.08	434	10857	84.51	109
	7012	500	9.38	437	10834	81.75	105
	*4232	443	8.31	560	19292	116.30	150
	7206	528	9.88	614	19244	122.05	156
	3870	427	8.02	630	27895	148.60	191
	7235	486	9.10	651	27701	139.12	178
	4117	494	9.28	712	35756	181.91	234
7075	568	10.64	812	35823	193.23	248	

* Data set in the shaded row is presented in the uncertainty analysis

VITA AUCTORIS

VITA AUCTORIS

NAME	Mesbah-ul Ghani Khan
PLACE OF BIRTH	Dhawakola, Bogra, Bangladesh
YEAR OF BIRTH	1963
EDUCATION	<p>1973. Completed elementary school (Grade-V) from Dhawakola Govt. Primary School, Bogra, Bangladesh and promoted to Grade VI at high school level</p> <p>1978. Completed 10-year schooling at Gokul T. U. High School, Bogra, Bangladesh and passed the first compulsory public exam SSC (Secondary School Certificate) in Science</p> <p>1980. Completed 2-year college schooling at Govt. A. H. College, Bogra, Bangladesh and passed the second compulsory public exam HSC (Higher Secondary Certificate) in Science</p> <p>1986. Received the Degree of Bachelor of Science in Mechanical Engineering from Engineering College, Rajshahi, Bangladesh (renamed as Bangladesh Institute of Technology – BIT and again as Rajshahi University of Engineering and Technology – RUET)</p> <p>2000. Received the Degree of Master of Science (M.Sc.) in Renewable Energy from the University of Oldenburg, Germany</p>
EXPERIENCE	1986-1998. Served as Mechanical Engineer in an Energy Utility
CURRENT	2003-2004. A candidate for the degree of Master of Applied Science (M.A.Sc.) in Mechanical Engineering at the University of Windsor, Windsor, Ontario, Canada and expecting to graduate in Summer 2004